Characterization of the small scale ice sheet topography of Antarctica and Greenland

Benjamin E. Smith

A dissertation submitted in partial fulfillment
of the requirements for the degree of

Doctor of Philosophy

University of Washington

2005

Program Authorized to Offer Degree: Department of Earth and Space Sciences - Geophysics

University of Washington
Graduate School

This is to certify that I have examined this copy of a doctoral dissertation by

Benjamin E. Smith

and have found that it is complete and satisfactory in all respects,
and that any and all revisions required by the final
examining committee have been made.

Chair of Supervisory Committee:

_____
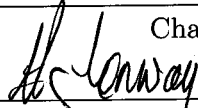
Charles F. Raymond
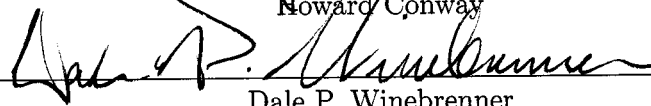
Reading Committee:

_____

Charles F. Raymond

_____
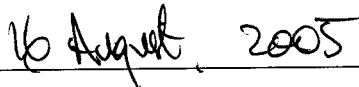
Howard Conway

_____

Dale P. Winebrenner

Date: _____16 August, 2005_____
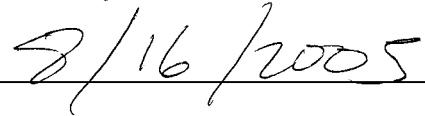
In presenting this dissertation in partial fulfillment of the requirements for the doctoral degree at the University of Washington, I agree that the Library shall make its copies freely available for inspection. I further agree that extensive copying of this dissertation is allowable only for scholarly purposes, consistent with "fair use" as prescribed in the U.S. Copyright Law. Requests for copying or reproduction of this dissertation may be referred to Proquest Information and Learning, 300 North Zeeb Road, Ann Arbor, MI 48106-1346, to whom the author has granted "the right to reproduce and sell (a) copies of the manuscript in microform and/or (b) printed copies of the manuscript made from microform."
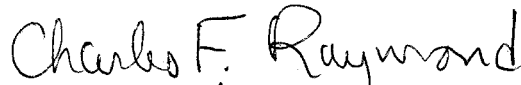
Signature _____

Date __2/16/2005__

University of Washington

Abstract

Characterization of the small scale ice sheet topography of Antarctica and Greenland

Benjamin E. Smith

Chair of Supervisory Committee:
Professor Charles F. Raymond
Department of Earth and Space Sciences

In this dissertation I analyze and model the characteristics of small-scale, dynamically supported topography. I develop a method for mapping spatial variations in the Fourier spectra of ice-sheet surfaces from elevation data measured along linear tracks. I find that there are characteristic patterns in these spectra, and that the shape of the spectra is largely determined by the local ice thickness, while the overall spectral amplitude is determined by the local surface slope and by bed roughness. I explain the broad features of the spectra and their variation with a model that describes the ice-sheet bed as isotropic red noise, and describes the ice flow dynamics with a perturbation analysis of flow of a viscous, Newtonian fluid. I further develop this model to take into account variations in the viscosity of the ice due to the nonlinear viscosity of flowing ice, and find that the patterns of surface topography are broadly consistent with expected variations in viscosity. Next, I analyze map-view variations in ice-sheet surface slopes, and find that there is a characteristic anisotropic pattern in surface slope variations that is common to Antarctica and Greenland. These variations are also consistent with a perturbation model of ice flow, which I use to show that the pattern of surface slopes may be useful in identifying areas where the ice is sliding rapidly at the bed. Finally, I analyze a two-year time-series of elevation measurements from the Ross Embayment in West Antarctica, detecting small but significant rates of elevation change throughout the region, with unexpectedly large rates of change in a few areas.

TABLE OF CONTENTS

LIST OF FIGURES

LIST OF TABLES

ACKNOWLEDGMENTS

This dissertation did not come about without drama, false starts, and sudden changes in direction. It would not have reached a successful conclusion if a very large number of people had not lent me their confidence and support. I will thank as many as I can, but if I leave any names out, be assured that it is only because the acknowledgments should be shorter than the dissertation they precede.

I have been very lucky to have Charlie Raymond as my advisor. He has been unfailingly patient through all of the bizarre permutations this project has taken over the last five years. Throughout, he has offered sharp insights and wise advice, and set an inspiring example of how to go about being a scientist. Charlie Bentley lured me into glaciology some years ago, and has encouraged and supported my work ever since. He has been a strong collaborator and a terrifying editor, and his suggestions for further research directions have been consistently excellent. Howard Conway persuaded me that the University of Washington was the place to continue my graduate career, and has offered me his encyclopedic knowledge of glaciology and glaciologists, and has kept a project conducted mostly from orbit grounded in field glaciology. Dale Winebrenner has kept me abreast of the broad world of remote sensing, and has pushed me to find practical applications for my work. John Stone and David Cobden were kind enough to agree to serve on my committee, and each has kept me honest along the way.

Ed Waddington has kept his door open, and has answered more questions and filled more gaps in my logic than I could possibly remember. The glaciology group graduate students have given me advice, moral support, and have shown by example that it is possible to survive grad school. In particular, my office mates, Ginny Catania and Erin Pettit, showed how to cross the finish line with panache, and kept my spirits up in the mean time.

I have been very fortunate to have a continuing relationship with the ICESat/GLAS

science team. I have learned a tremendous amount about how big collaborative science projects are conducted by participating in their meetings. I particularly recall a comment by Jeanie Sauber, in the dark days before the ICESat launch, that the best dissertations are about theory rather than data- I can only hope that I have enough of each.

Melanie Raymond and Hilmar Gudmundsson gave me considerable assistance at the very last minute, salvaging a chapter and bringing clarity to much of the rest of the dissertation. Ted Scambos and Terry Haran gave me a data set that made chapter 4 possible, and kept me busy before ICESat data became available.

I thank my parents and my sister for the love and encouragement they have given me before and during this process. They have given me both intellectual drive and humane perspective that have served me well in and out of school.

Finally, this work would not have been feasible without the support of my frequent collaborator, Dr. Jennifer Loertscher. Dr. Loertscher advised me on a number of important subjects, and has somehow kept me sane and on track.

Chapter 1

INTRODUCTION

A man who keeps company with glaciers comes to feel tolerably insignificant by and by. The Alps and the glaciers together are able to take every bit of conceit out of a man and reduce his self-importance to zero if he will only remain within the influence of their sublime presence long enough to give it a fair and reasonable chance to do its work.

-Mark Twain, from "A Tramp Abroad" 1880

1.1 Background

For the last thirty years, the great ice sheets in Greenland and Antarctica have been intensively mapped using data from satellite altimeters. The most important reason for mapping, then mapping again, the ice sheet surfaces has been to detect elevation changes that might imply, or forewarn of, the motion of grounded ice into the ocean. Enhanced melting, decreased snowfall, accelerated ice motion, and retreat of grounding lines all can lead to sea level rise, and all should produce changes in the ice sheet surface elevation visible from space. Yet until recently, these changes have proven difficult to measure and to interpret, because instrumental biases and the variability of snowfall from one year to the next have made small elevation changes difficult to detect, and have made even large elevation changes difficult to interpret.

A secondary set of benefits have come from the elevation maps themselves. In some recently published studies, ice-sheet elevation maps have been used to infer the drainage patterns of the ice sheets (Bamber and others (2000)), and to help infer the local stress balance in models (Joughin and others (2004)). The present surface elevation is also used

to initialize models to analyze the time-evolution of glaciers (Parizek and others (2002), Wild and others (2003)).

Most applications of ice-topography data implicitly or explicitly use the SIA (Shallow-Ice Approximation), in which longitudinal stress gradients are ignored. Only topography at scales larger than about ten ice-thicknesses is relevant to glacier dynamics in this approximation (Kamb and Echelmeyer (1986)), and shorter-wavelength features are usually filtered out during analysis. However, the features ignored in the SIA are ubiquitous over the Greenland and Antarctic ice sheets. Analysis by Whillans (1983), Thorsteinsson and others (2003) and Gudmundsson (2003), shows that many of these features arise from bedrock roughness and from variations in sliding at the ice-sheet bed. This suggests that analysis of surface undulations may reveal characteristics relating to geology and the thermal conditions of the bed, each of which may play a part in determining the stability of the ice sheet (Bell and others (1998)).

To a limited extent, it is already possible to infer information about the bed of an ice sheet based on an intuitive understanding of what normal ice sheet topography looks like, and what features are exceptional, and therefore informative. Analysis of elevation models and shaded-relief imagery of ice sheet surfaces can in some cases reveal the location of active and relict ice-streams (Hodge and Doppelhammer (1996), Scambos and others (1998), Ekholm and others (1998)), and until recently, the extent of subglacial Lake Vostok was best known by the extremely flat surface topography above it, measured using satellite radar altimetry (Ridley and others (1993)). Thorsteinsson and others (2003) demonstrated a technique for the inversion of surface topography and ice velocity data for bed topography and sliding rates, but their technique requires high-resolution topography and velocity data that are not available for most of Antarctica.

Small-scale ice-sheet topography itself can drive some small-scale ice-sheet processes. Bindschadler and others (2004) showed that local surface-slope reversals associated with O(10 km)-scale topography can trap water at the bed in ice-streams, and Gray and others (2005) measured ice-surface motions on comparable scales, which they believe to reflect motion of water pockets at the bed. Storage and transport of water beneath ice streams in this way could provide a mechanism for short-period changes in ice stream velocity. Surface

processes also have important controls from small-scale topography: Spikes and others (2004) showed that short-scale variations in snow accumulation are strongly correlated with kilometer-scale surface topography.

There have been few systematic studies aimed at characterizing the nature of ice-sheet topography on fine scales. The most comprehensive characterization of medium-to-large-scale surface topography is by Remy and Minster (1997), who described Antarctic ice-sheet undulations on scales of 50-100 km, and showed that in a steady state, the ice-sheet shape at this scale is largely determined by the geometry of outlet glaciers. Other authors have made local studies of 1-10 km -scale surface topography: Budd and Carter (1971) measured ice-sheet undulations on scales of a few kilometers, and presented a spectral analysis showing that the peak of the power-spectrum for these undulations came at about three times the ice thickness. McIntyre (1986) found undulations at similar scales in Antarctica, but demonstrated that the spectrum did not have a maximum at three ice thicknesses, and instead increased in power monotonically with wavelength. Malamud and Turcotte (2001) showed that a profile measured in West Antarctica measured with radar altimetry had a bi-fractal topography, with a power-law relationship between wavelength and amplitude. Jóhannesson (1992) showed that the ice-topography on Höfsjokul, Iceland, could be explained well by the dynamics of ice flow over a rough bed.

These measurement-based studies show that kilometer-scale surface topography of 1-100 m of amplitude is found throughout Antarctica and Greenland, that ice-sheet surfaces are very smooth at scales smaller than one ice thickness (but larger than crevasses or sastrugi), and that there are indications that the magnitude of surface undulations varies smoothly from one part of the ice sheet to another. However, there is no clear way to say with any precision whether the topography in any one part of Antarctica is typical of Antarctic topography in general, nor is there any simple way to distill from these studies a picture of what properties ice sheet surfaces have in common with one another that makes them different from all other earth surfaces. In part, this is because ice-topography data that could resolve small-scale features were not available for much of the ice sheet.

Very recently, a set of data that accurately measures ice topography from very long to very short scales has become available. Since its 2003 launch, ICESat (Ice Cloud and

land Elevation Satellite) has measured around 3 million kilometers of topographic profiles in Antarctica. ICESat was designed with very high precision so that it could measure elevation changes accurately, but ICESat data have proven useful in mappin and characterizing ice topography. I have been fortunate to have early access to these data, which have largely resolved the instrumental effects that obscure fine-scale surface topography in older radar-altimetry data sets, and have sufficiently broad coverage to allow me to draw generalizations about the nature of surface topography of Antarctica.

1.2 Motivation and Goals

The goal of this dissertation is to characterize small-scale ice sheet topography. By presenting statistics of ice-sheet topography derived from ICESat data and from older radar-altimetry data, I will show how ice-sheet elevations vary in space, with scale, and, for a limited area in West Antarctica, in time. I will investigate the dynamics of ice that give ice surfaces their unusual characteristics different from other land surfaces, and will show which glaciological variables lead to spatial variations in these characteristics. No previous study has synthesized continental-scale data with ice-dynamic theory to find typical ice surface characteristics at fine scales. This analysis will allow future researchers to identify unusual areas in ice-sheet surfaces needing further study, to accurately model small-scale topography in models of ice-atmosphere and ice-bed interactions, and to design surveys that efficiently measure the most significant features of ice-sheet topography.

1.3 Organization of the dissertation

Each chapter in this dissertation was written as an independent manuscript. Chapter 5 has been submitted to Geophysical Research Letters, and chapters 2, 3, and 4 are in preparation to be submitted to various journals. Some discussion of techniques and theory is therefor repeated between chapters.

Chapters 2, 3, and 4 explore the characterization of fine-scale ice-sheet topography revealed by satellite altimetry. Chapter 2 shows the spectral characteristics of ice-sheet elevation profiles, demonstrating that ice sheet surface spectra have broadly uniform spectral

properties measured on a non-dimensional wavelength scale. These properties are entirely different from those of typical land surfaces, and we explain the difference using transfer theory to show that the ice sheet surface characteristics result from glacier flow over a bed that has characteristics typical of land surfaces. I also generate a digital elevation model that accurately resolves ice surface slopes in the southern part of Antarctica not previously covered by satellite altimetry.

In chapter 3 I expand on this model, using a more complex version of the transfer theory that takes into account ice-viscosity variations due to temperature variations and the nonlinear viscosity of flowing ice. I show that spectra calculated from surface elevation measurements are statistically consistent with those expected when the effects of longitudinal stretching on ice viscosity are taken into account, but inconsistent with those expected when only viscosity variations due to thermal variations and shearing flow are taken into account. This shows that taking into account softening of the ice near the surface due to longitudinal stretching is important in understanding ice surface texture.

In chapter 4, I expand my view from undulations measured on single profiles of ice elevation, and examine the anisotropic patterns of short-scale surface undulations found in Antarctica and Greenland. I demonstrate that short-scale undulations are of significant magnitude compared to the large-scale surface slope of the ice sheets, and find characteristic anisotropic patterns in the spatial organization of undulations that are seen on both ice sheets. This pattern is readily explained with the same kind of ice-flow model used in chapters 2 and 3, and I show that fast-streaming ice can be distinguished from ice that is frozen at the bed on the basis of patterns in the surface texture.

In chapter 5, I quantify surface elevation changes measured with ICESat during its first 24 months of operation over the Ross Embayment. I show that most of the measured surface elevation changes are not significantly different from those predicted based on previous glaciological studies. In a few regions, rates of elevation change indicated by ICESat data are unexpected: Conway Ridge appears to be thinning rapidly, while the trunk of Kamb Ice Stream is thinning slowly, rather than thickening.

Chapter 2

CHARACTERISTIC SPECTRUM OF DYNAMICALLY SUPPORTED TOPOGRAPHY REVEALED BY ICESAT ELEVATION PROFILES

2.1 Summary

Spatial variations in local Fourier spectra of ice-elevation profiles are estimated in Antarctica. Although each component of the spectra varies strongly in space, the shapes of the spectra become uniform throughout Antarctica when plotted on logarithmic axes as a function of a non-dimensional wavelength equal to the spatial wavelength divided by the ice thickness. The overall amplitudes of the spectra correlate well with the surface slope, and weakly with the ice thickness. These properties are explained with a model of ice-sheet topography resulting from a descriptive red-noise model of the ice-sheet bed combined with a process-oriented model of ice flow.

2.2 Introduction

In this paper we present a statistical description Antarctic ice sheet topography on scales of 1-50 km. This topography is at smaller scales than that usually treated in ice-sheet modeling, and indeed, in the commonly used "Shallow Ice Approximation" its effects on ice-sheet dynamics are explicitly filtered out. Yet short-wavelength surface undulations are present everywhere on the ice-sheet and, when ground measurements are made, dominate the local environment. For example, in studies of ice-stream dynamics, the local surface slope across a ten-kilometer-wide strain grid may be much different than the mean surface slope of the ice stream (e.g. Liu and others (1999)), and the difference between the two must be taken into account in calculating the local force balance. Likewise, kilometer-scale variations in surface slope appear to control accumulation variability in many places on the ice-sheet (Spikes and others (2004)).

A straightforward way to describe the undulations of earth surfaces is to calculate their Fourier spectra. Studies of this type on land surfaces often show spectra whose amplitudes increase monotonically with wavelength. Such surfaces, whether called "self-similar" or "self-affine" or "fractal," have no natural scale; they have the same characteristics when viewed at high or at low magnification. Their spectra, plotted on log-log axes, have slopes, $d\,log(A)/d\,log\lambda$ that are positive and approximately independent of λ. Typical measured values of $d\,log(A)/d\,log\lambda$ are on the order of 5-10 dBa (decibels of amplitude, defined as $10\,log_{10}$ of the spectral amplitude) per decade (Turcotte (1992)).

Investigations of ice sheet dynamics have led to a series of mathematical treatments of how ice sheet topography relates to bed topography. One of the earliest was a discussion by Nye (1959a), who showed how ice-sheet surface topography relates to bedrock undulations based on a perturbation analysis of ice-flow. Budd (1968) and Budd (1969) expanded on Nye's theory, and introduced a convenient way to describe the relationship between ice sheet beds and surfaces with a transfer function ($T(\lambda)$) that relates bed spectra ($B(\lambda)$) to surface spectra ($S(\lambda)$):

$$S(\lambda) = T(\lambda)B(\lambda). \tag{2.1}$$

Budd and Carter (1971) calculated transfer functions with a peak at about $\lambda = 3h$, declining with wavelength at longer wavelengths. Hutter and others (1981) showed that a fuller treatment of the force-balance eliminates this spectral peak, and results in a monotonic increase in T with λ. The most recent studies (Reeh (1982), Jóhannesson (1992), and Gudmundsson (2003)), which include the most sophisticated treatments of the force balance, show very weak transfer for wavelengths less than the ice thickness, with transfer increasing rapidly for wavelengths on the order a few times the ice thickness, then gradually approaching an asymptotic value of 1 in the long-wavelength limit. This work suggests that, unlike land surfaces, ice sheet surfaces should have a natural length scale: Surface topography should be very weak for wavelengths less than the ice thickness, and should gain amplitude rapidly with wavelength for wavelengths a few times the ice thickness.

Until recently, the most comprehensive data sets of Antarctic Ice Sheet elevation came from satellite radar altimetry. Satellite radar altimeters can accurately resolve surface fea-

tures larger than the 5-10 km pulse-limited width of the radar beam, but features smaller than this are smoothed and shifted in position, and cannot be measured accurately. This means that while these measurements often match the predictions of transfer theory, with topographic amplitudes falling to zero at wavelengths of a few ice thicknesses, it cannot be determined whether this is a property of the ice topography or an artefact of the measurements.

Since 2002, ICESat (Ice, Cloud, and land Elevation Satellite) has been making very accurate measurements of ice-sheet elevation at high resolution on profiles separated by less than 20 km for most of Antarctica. These profiles are the first continental scale data-set that can resolve undulations with wavelengths as small as 350 m. With these data, we have estimated ice-sheet surface spectra over a wide range of wavelengths. We find that, while spectra are quite variable from one part of the ice sheet to another, there is a characteristic shape to the surface spectra when they are plotted against λ/h, and this characteristic shape matches the predictions of transfer theory under the assumption that the glacier bed is a typical red-noise land surface. Further, in analyzing the spatial distribution of the overall amplitude of the ice-sheet surface, we find that there is a correlation between large surface amplitudes and strong surface slopes. Ice streams are an exception to this relationship, because strong sliding at the bed leads to enhanced transfer of bed topography to the surface.

2.3 Measurements

All of the surface elevation measurements in this paper come from ICESat. ICESat measures ice-sheet elevations with a pulsed infrared laser, giving elevation measurements accurate to 5-10 cm in profiles along its ground tracks (Zwally and others (2002)). ICESat measurements represent the mean elevation of the laser footprint, which is about 70 m wide; this gives ICESat measurements much higher resolution than previous radar-altimetry missions, which had pulse-limited footprints 5-10 km wide. ICESat ground tracks converge at 86°S, and are separated by about 20 km at the northern edge of Antarctica.

To minimize errors due to forward scattering by clouds and highly saturated returns, we

filter the data based on a set of parameters describing the return pulse, provided in GLA12. Returns unaffected by saturation or forward scattering resemble narrow Gaussian pulses, similar to the transmitted pulse. We expect saturation and forward scattering to change the shape of these pulses, increasing the apparent surface roughness (estimated from the width of the return-pulse), the misfit between the return pulse a Gaussian, and expect clouds to decrease the apparent surface reflectivity. We also expect forward scattering to increase the apparent shot-to-shot surface roughness because of inhomogenaeties in cloud layers. After some experimentation, we find that if we reject all returns for which the apparent surface reflectivity is less than 40 % or the apparent surface roughness is more than 2 m or the RMS difference between the digitized waveform and the best-fitting single Gaussian is more than 0.06 mV, we can reduce the RMS shot-to-shot surface roughness for the flat parts of WAIS from 0.30 m to 0.025 m. These criteria reject about 45% of all shots.

2.4 Spectral Analysis

In this section we quantify spatial variations in the topography revealed by ICESat data. We use a windowed Fourier transform to derive measures of the spectral content of ICESat profiles for short segments of data, then map variations in each spectral component at a resolution of 20 km. These maps allow us to synthesize a spectral estimate for the ice-sheet topography at any point on the ice-sheet.

In describing topography we use three measures: spectral amplitude, spectral roughness, and spectral exponent. Spectral amplitude is estimated from a windowed Fourier transform:

$$A(k) = \frac{\sum_{j=1}^{N} W_j z_j e^{(-i2\pi(k\delta-1)(j-1)/N)}}{\sqrt{\sum_{j=1}^{N} W_j^2}} \qquad (2.2)$$

where z_j are the N sampled surface elevation values, k is the wavenumber, δ is the measurement interval, and W_j is a spatial weighting function (here a raised cosine function) that reduces spectral leakage. The denominator in equation 2.2 normalizes the spectrum so that a sine wave of unit amplitude has a spectral amplitude of 1, regardless of the length of the profile. The amplitude values have units of meters, although we will sometimes speak of decibels of amplitude (dBa), expressed as $10 \, log_{10}(A/1 \text{ meter})$. Amplitude spectra as a

function of k may be expressed as a function of wavelength, λ, under the transformation: $\lambda = 2\pi/k$.

Spectral roughness is the RMS (Root Mean Square) surface slope associated with a spectral component, and is found:

$$R(\lambda) = A(\lambda)/\lambda. \tag{2.3}$$

Spectral roughness values are unitless.

Spectral exponents describe the local slope of a log-log plot of amplitude against wavelength. We adopt this term because if $A \propto \lambda^\gamma$, then $d(logA)/d(log\lambda) = \gamma$. We express spectral exponents in units of dBa/decade. A spectral slope of 20 dBa/decade means that the spectral amplitude at 10 λ_o is 100 times that at λ_o.

2.4.1 Estimating surface spectra

The scale at which we map spectral variations determines the smallest features that our analysis will measure. Outlet glaciers, ice streams, and ice rises all have widths on the order of 40-80 km, so to ensure that our measurements can resolve such features, we choose to map the spectral variations in topography at a grid resolution of 20 km. Spectral components with wavelengths much larger than 20 km vary only on scales larger than the grid resolution and will appear to be smooth in these maps, but variations in short-wavelength spectral components will be resolved.

To achieve the best resolution for each spectral component, we derive spectral estimates from segments of ICESat data that are as short as possible for each wavelength. We have adapted the standard Welch's method to the very red spectra of ice-surface profiles in a way that avoids spectral-leakage problems that can otherwise overshadow real variations in the data. Spectral leakage comes about because for Fourier-transform-based spectral estimates, the spectral estimate recovered at each wavenumber is a weighted sum of all amplitudes at all wavenumbers present in the surface profile. The weighting function is peaked at the wavenumber being estimated, but if it has secondary maxima (side-lobes), it can be sensitive to high-amplitude parts of the spectrum far from the peak. This becomes a severe problem in short profiles, because the width of the sidelobes is large compared to the

wavenumber-range of the spectrum measured (Austin and others (1994)). If steps are not taken to avoid this problem, local spectral exponents estimated for red-noise surfaces will be too small, and the measured spectrum will be less red than the true spectrum, particularly at short wavelengths.

We minimize leakage in two ways: First, by choosing a windowing function with very weak side-lobes, we avoid long-range leakage at the expense of some spectral blurring. The customary choice of a windowing function in Welch's method is the Hanning function, the magnitude of whose side-lobes falls off with distance from the main peak by about 15 dBa per decade of wavenumber. We use instead the square of the Hanning function, whose side-lobes fall off at about 30 dBa per decade.

Second, by filtering our data before estimating the spectrum, we avoid leakage from the DC (k=0) band into other parts of the spectrum. We filter the data using a sixth- order Butterworth bandpass filter with cutoff wavelengths λ_l and λ_h that depend on the length of the segment of data to be filtered. We use this filter mostly as a high-pass filter, but using a band-pass avoids instability in filter behavior at the start and end of each profile. From experiments on synthetic ice-surface-topography data, we find that for a profile of length L, with sampling interval δx, we can recover accurate spectral estimates for $L/9 < \lambda < L/3$, using cutoff wavelengths $\lambda_l = 2L/3$ and $\lambda_h = 2L/(L/\delta x - 9)$. Thus, to recover each spectral amplitude estimate $A(\lambda)$, we require a profile at least 3λ long.

To recover amplitudes for wavelengths shorter than $L/9$, we subdivide our profiles into two shorter segments; thus, we filter and analyze an 80 km profile to give estimates for wavelengths between $\lambda = 8.8$ km and $\lambda = 26.6$ km, then split the profile into two 40 km segments, each of which gives estimates for wavelengths between $\lambda = 4.4$ km and $\lambda = 26.6$ km. This process can be repeated to give spectral estimates for wavelengths as small as 0.5 km. The shortest wavelengths are estimated from 5.4 km-long profiles containing 32 samples.

Figure 2.1 shows the spectrum recovered from an 85 km long profile of synthetic ice-surface topography. The spectrum we seek to recover (the "true" spectrum, used to generate the synthetic data) from this profile has a local spectral exponent of 25 dBa/decade at the short-wavelength end, and a spectral exponent of about 10 dBa/decade at the long-

wavelength end. Because the profile has been subdivided, there are multiple estimates of the amplitude for each wavelength less than 26 km. These are scattered around the true value, but the median of the estimates at any wavelength gives a good estimate of the true amplitude.
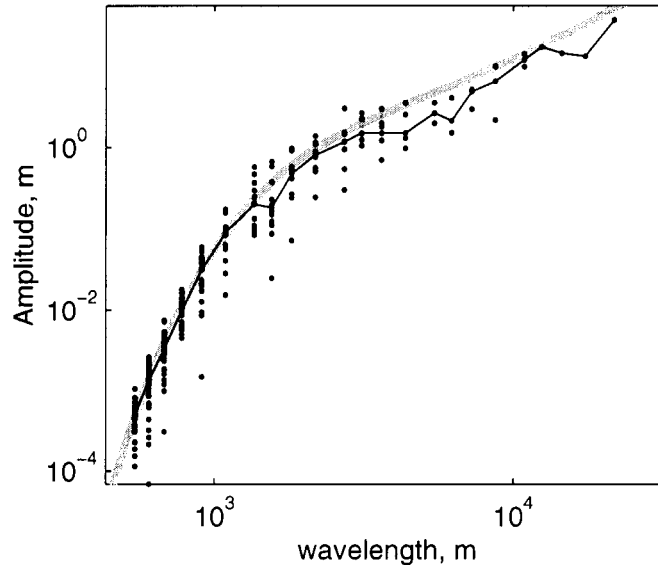
Figure 2.1: Recovery of a spectrum from synthetic ice-surface spectrum data, generated for slow sliding and h=2 km using techniques described in section 2.6. The heavy line shows the spectrum used to generate the synthetic data, while points give recovered amplitude estimates. The median of these (thin line) gives an *a posteriori* estimate of the true spectrum.

Figure 2.2 shows recovered spectral components for a profile running from the Transantarctic mountains (grid south) to Dronning Maud land (grid north). A spectral estimate recovered using Welch's method for a 2048-sample segment of track in Dronning Maud land shows typical characteristics of a surface-amplitude spectrum. The short wavelength region (I) of the spectrum shows only shot-to-shot noise, which in this area is on the order of 0.05 m. In the moderate wavelength region (II), the surface spectrum dominates the noise, and increases rapidly with wavelength. For long wavelength components (III), the spectrum increases more slowly. We can quantify the spectral exponents by fitting the following

equation to the spectrum in a log-least-squares sense:

$$A(\lambda) = A_o \begin{cases} (\frac{\lambda - \lambda_c}{\lambda_c})^{\beta_S}, & \lambda_S \leq \lambda \leq \lambda_c; \\ (\frac{\lambda - \lambda_c}{\lambda_c})^{\beta_L}, & \lambda_c < \lambda \leq \lambda_L. \end{cases} \qquad (2.4)$$

β_S gives the short-wavelength (region II) spectral exponent, β_L gives the long-wavelength (region III) spectral exponent, and A_o gives a measure of the overall spectral amplitude. We find that for figure 2.2 panel B, $\beta_S \approx 22$ dBa/decade and $\beta_L \approx 5$ dBa/decade, for $\lambda_S = 3$ km, $\lambda_c = 18$ km , and $\lambda_L = 60$ km.

In the bottom panel of figure 2.2 we show the 0.5 km, 1 km, 4 km, 17 km and 69 km spectral components recovered using the windowed Fourier transform technique. The 0.5 km and 1 km wavelength curves mainly show variations in the noise level in the ICESat measurements, which are largest on the flanks of the ice sheet. Variations in the 4 km, 17 km and 69 km components are generally correlated over the ice sheet, with larger values in mountainous regions and near the edges of the ice sheet. The shape of the spectral curve shown in figure 2.2 panel B is typical throughout the profile; because the band of wavelengths between 4 km and 17 km is usually in region II, while the band of wavelengths between 17 km and 69 km is usually in region III, the difference in amplitude between the 17 km curve and the 4 km curve is much larger than that between the 69 km curve and the 17 km curve.

2.4.2   Mapping spectral amplitude data

To display our amplitude estimates, we construct maps of the logarithm of the spectral amplitude recovered from GLAS data, for wavelengths between 1 km and 85 km. These maps are divided into 20 km by 20 km square bins; where multiple estimates are found within a bin, the median is recorded, and where no estimates are available for a bin we interpolate between the available data using a cubic spline under tension (Smith and Wessel (1990)). The data have a large dynamic range, and the scatter in the spectral components can cause adjacent spectral estimates to vary by a factor of 2-10. If we were to map the raw spectral estimates, this would produce a very rough map for each spectral component, with large variations in the interpolated values due to the spline algorithm. We avoid spurious

14
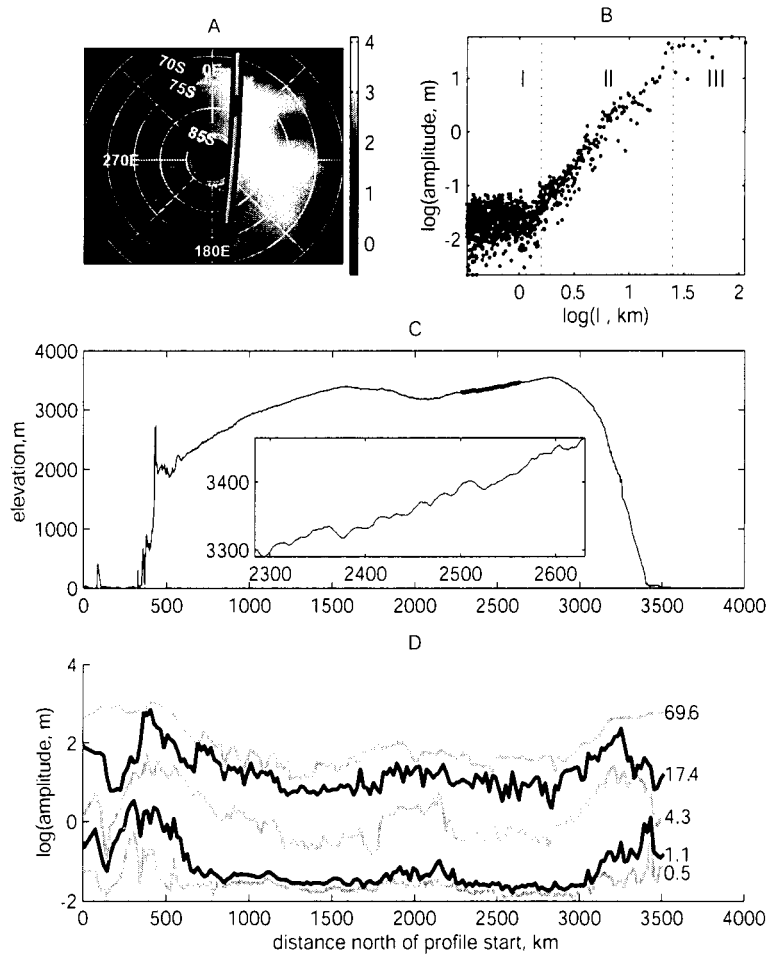
Figure 2.2: Topographic profile and recovered spectrum for an ICESat track across Antarctica. (A) shows the track, plotted over Antarctic topography, running from grid south to grid north. (C) shows the elevation profile, with an inset showing in detail a segment of topography from Dronning Maud Land, which is highlighted in (A) and (C). (B) shows the spectral estimate recovered using Welch's method for the segment of topography highlighted in (C). (D) shows the variation in the 5 spectral components across the profile. Each component is labeled at right with its wavelength in km.

variations in the interpolated values by mapping the logarithm of the amplitude estimates rather than the estimates themselves, because the log values have much smoother spatial gradients. Since the ice surface is not necessarily isotropic, we construct maps for this paper using the ascending ICESat tracks. The descending-track results are largely identical to those shown here; the anisotropic properties of ice-sheet surface are described by Smith

(2005), chapter 4.

Locations discussed

We will show results for the Antarctic continent at large scale to show the general properties of and controls on spectra, and will show fine resolution results for the Ross Embayment, West Antarctica, whose ice streams and inter-stream ridges are difficult to resolve in the continent-scale maps. Figure 2.3 shows the location of the Ross Embayment and the ice streams.
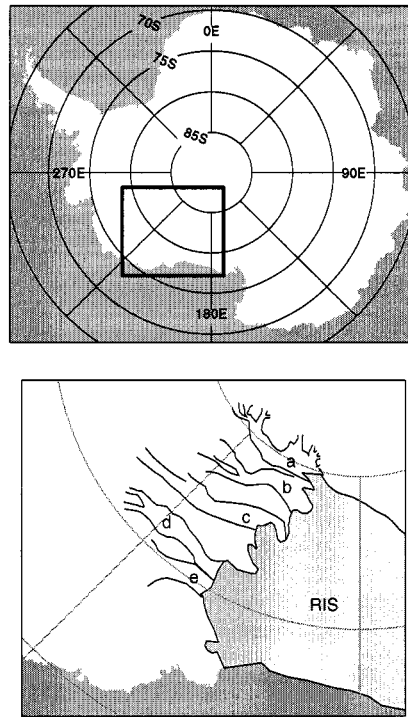
Figure 2.3: Location map, showing the Antarctic continent with latitude and longitude lines labeled (labels will be omitted in later maps), with box showing location of Ross Embayment inset. Bottom: Ross Embayment location map. The Ross ice shelf is shown in gray, with an approximate estimate of the grounding line. The shear margins of the ice streams are shown in black; ice streams are labeled 'a': Mercer; 'b': Whillans/Van der Veen; 'c', Kamb; 'd', Bindschadler; 'e', Macayeal.

2.5 Results

In this section we show that the spectral exponents derived from the short- and long-wavelength parts of the spectrum in figure 2.2 are typical of ice-sheet surfaces, but that the wavelength at which the spectral exponent changes depends strongly on the ice thickness. We show that the surface roughness due to small-scale topography depends on the large-scale slope of the ice sheet and the rate of sliding, but these factors do not entirely explain the surface amplitude everywhere.

2.5.1 Surface amplitudes

Figure 2.4 shows the recovered ice-sheet amplitude for $\lambda = 680$ m, $\lambda = 6.2$ km, and $\lambda = 69$ km. These maps show that everywhere on the ice sheet, long-wavelength components dominate the surface spectrum. The 6 km and the 68 km maps appear to share many of the same features, although the 69 km map has consistently larger amplitudes. However, the 69 km amplitude increases smoothly from the center of the ice-sheet to the coast, while the 6.2 km amplitude falls off sharply in the center of the ice sheet, near the flow-divides,

In the Ross Embayment, all of the ice streams except Kamb ice stream show strongly enhanced surface spectra for $\lambda = 680$ m because of surface crevassing. Crevasses are also apparent in the main shear zones on the Ross Ice Shelf. Kamb ice stream, which stagnated in about 1850 AD (Smith and others (2002)), has no surface crevasses, and appears smooth. For $\lambda = 6.2$ km, the undulating surfaces of the active ice streams have a much larger amplitude than the inter-stream ridges, which are smooth, as is the Ross Ice Shelf. For $\lambda = 69$ km, the region including the ice streams is apparently quite rough because of the elevation differences between the ice streams and the inter-stream ridges.

2.5.2 Characteristics of recovered spectra

Spectral exponents of ice elevation data

The general shape of the profile in 2.2 panel B is typical of ice-sheet spectra; most have a distinct region II, where amplitude increases rapidly with wavelength and a region III, where the amplitude increases slowly with wavelength. The spectral exponent in region

Log amplitude for λ=0.68 km

Log amplitude for λ=6.22 km

Log amplitude for λ=69.6 km
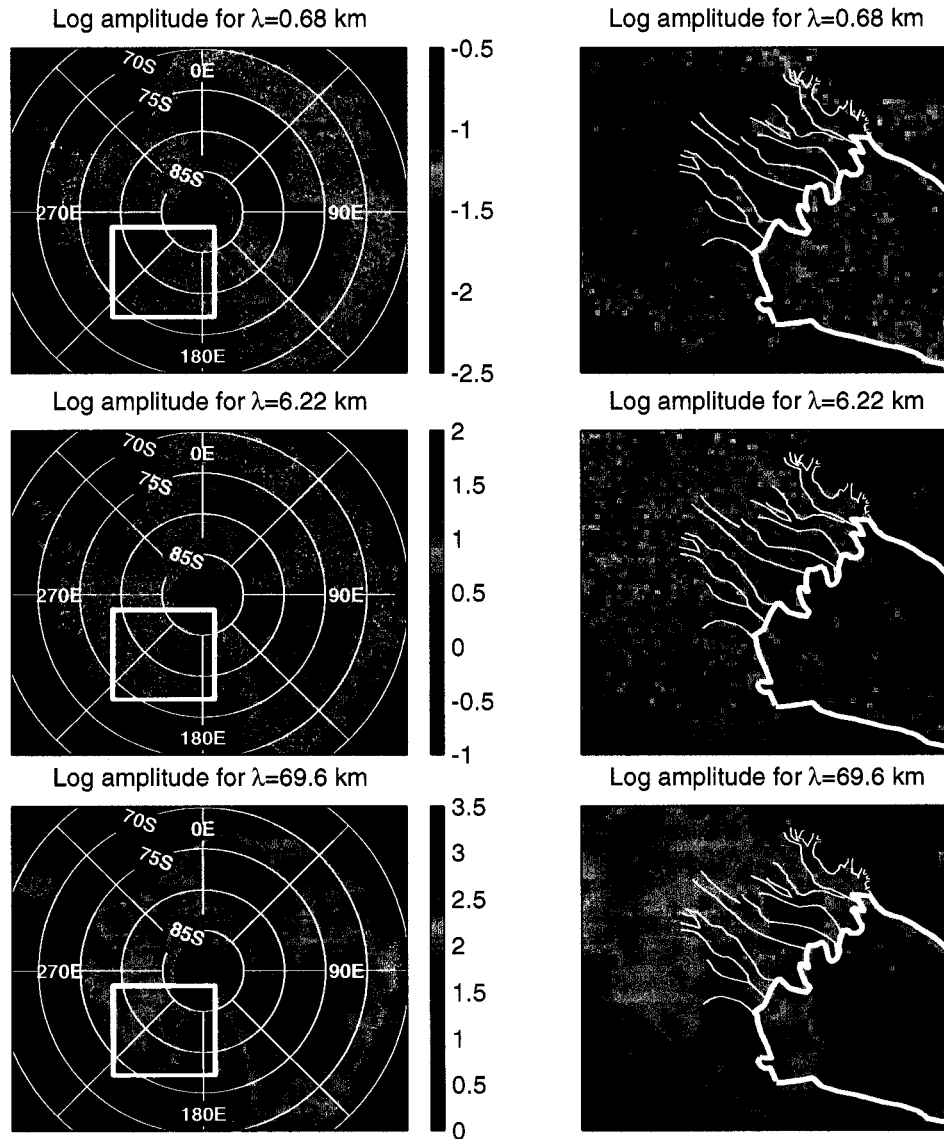
Figure 2.4: Maps of recovered log spectral amplitude, color-scales in center. At left, we show the entire Antarctic continent; at right, we show the Ross Embayment region, with ice stream outlines shown by dotted white lines.

II is much larger than the spectral exponents typical of land surfaces, which are typically between 5 and 10 dBa/decade. The discussion of transfer theory section 2.2 suggests that in the range of wavelengths up to several times the ice thickness, the transfer increases strongly with wavelength, which would produce the increase in amplitude in region II if bed

spectra were typical of land surfaces, while the slow increase in transfer at long wavelengths might lead to the shallower slopes in region III. This means that the shape of the spectrum, defining the boundary between region II and region III should be determined by the ice thickness. Indeed, if the the surface spectrum is determined by transfer, then the shape of the spectrum should be consistent from place to place as a function of non-dimensional wavelength, λ/h. In this section we show individual examples of profiles that have the same shape as a function of λ/h, and present a survey of spectral exponents across the ice sheet for region II and region III for fixed intervals of λ and for fixed intervals of λ/h to demonstrate that the natural wavelength-component for describing ice-sheet spectra is λ/h. We derive the ice thicknesses from a compilation by the BEDMAP project (Lythe and others (2001), shown in figure 2.5, top panel).

We show spectra that are similar as a function of λ/h in figure 2.5: Five spectra, for ice thicknesses between 1.7 and 4 km are shown, on a rough line between Lambert Glacier, and Dome C, in East Antarctica. The profiles have the same shape when plotted on log-log axes, as shown in the middle panel, although the thick-ice plots are shifted to longer wavelengths. When the spectra are plotted against non-dimensional wavelength, λ/h, the changes in slope occur at roughly the same non-dimensional wavelength for each, and the most significant difference between the profiles is an offset in amplitude due to larger overall amplitudes in the thin-ice profiles.

Another illustration of the non-dimensional behavior of spectral shapes is to compare spectral exponents measured over intervals fixed in λ to spectral exponents measured over intervals fixed in λ/h. If the shapes of the spectra are uniform, we should measure consistent spectral exponents over intervals fixed in λ, for region II bounded by 2 km $< \lambda <$ 12 km and region III bounded by 12 km $< \lambda <$ 40 km. If the shapes of the spectra are determined by transfer, we should measure consistent spectral exponents over intervals fixed in λ/h, for region II bounded by $h < \lambda < 6h$ and region III bounded by $6h < \lambda < 20h$.

In figure 2.6 we show the spectral exponents for region II and region III at fixed wavelengths (top), and for region II and region III defined relative to the ice thickness (bottom). The fixed-wavelength maps show strong spatial correlation between thick ice and steep short-wavelength slopes: In the interior of East Antarctica, where the ice is on the order of
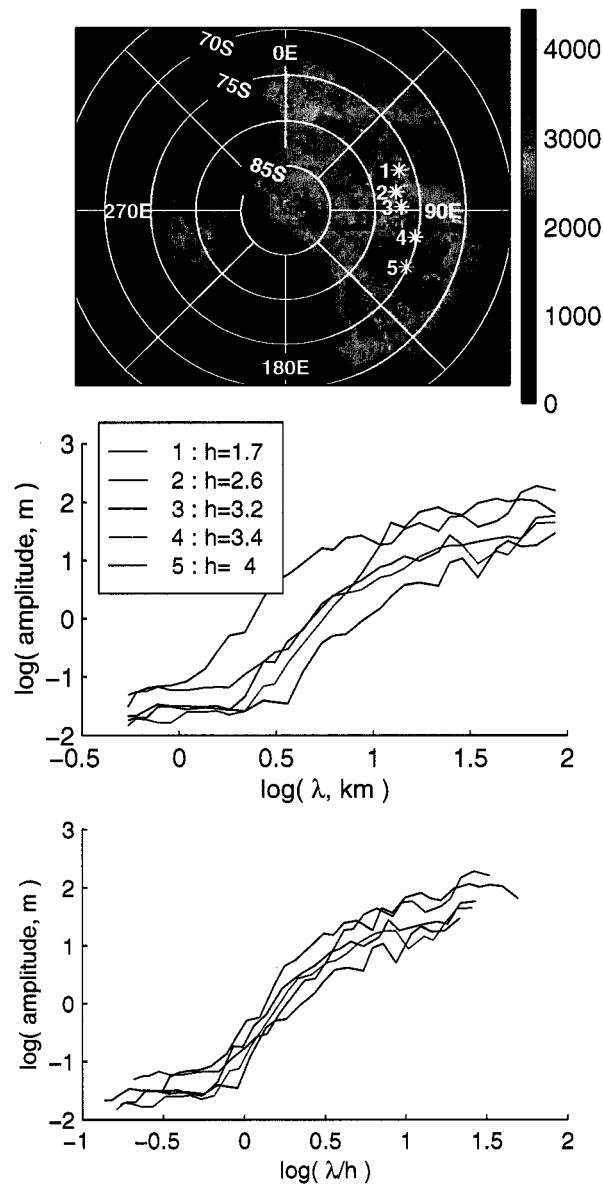
Figure 2.5: Spectra for thin and for thick ice. Top: locations for spectra, on a background showing the BEDMAP ice thickness (Lythe and others (2001)). Middle: Spectra plotted as a function of λ, in km. Ice thicknesses (in km) given in legend. Bottom: Surface spectra as a function of λ/h.

3-4 km thick, the region II slope is on the order of 25-35 dBa/decade, falling to 10-20 in the thin-ice regions of the Siple Coast. By contrast, for region II and III defined relative to λ/h,

we find that region II slopes vary irregularly between 15 dBa/decade and 25 dBa/decade, and are not strongly correlated with the ice thickness.

The long-wavelength spectral exponent is less sensitive to the choice of coordinates, because the spectra are relatively flat near $\lambda = 6h$; however, the long-wavelength slope is slightly smaller and more homogeneous for region III when defined relative to λ/h.
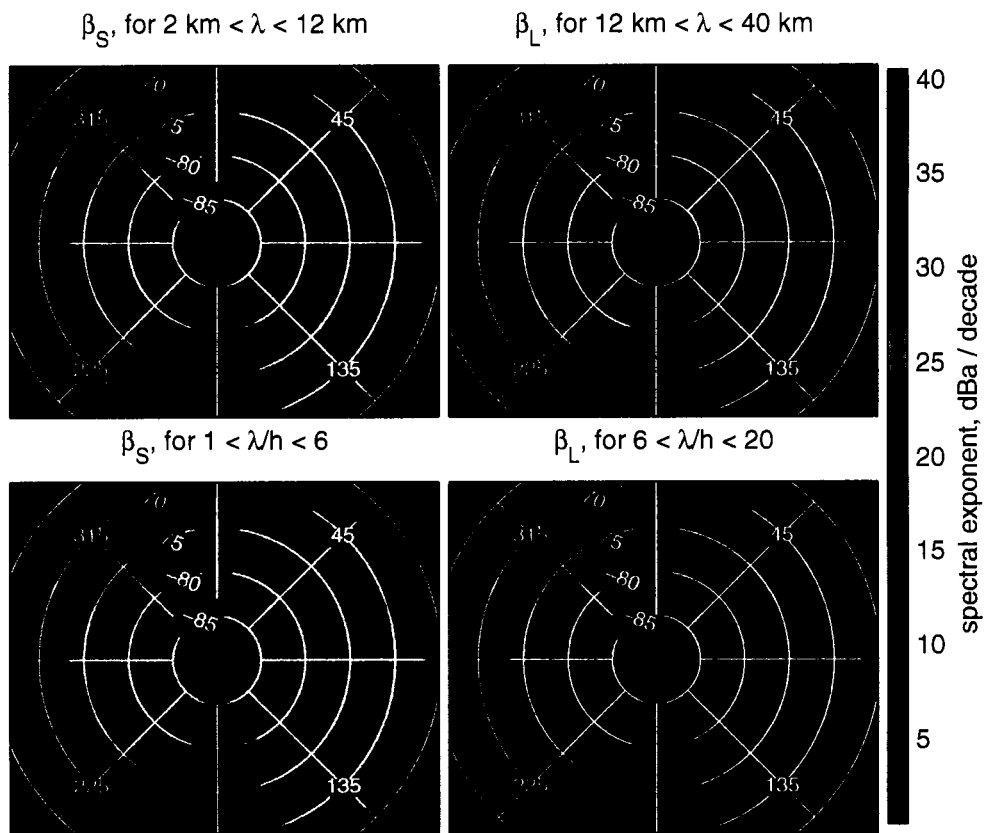
Figure 2.6: Maps of the spectral exponent for short wavelength (at left) and long wavelength(at right). The top row shows spectral slopes for intervals of constant wavelength, the bottom row shows spectral slopes calculated for intervals of constant λ/h.

Roughness of ice elevation spectra

To measure amplitude in a way that consistently samples the same part of the amplitude-versus-λ/h curve, we calculate the spectral roughness at $\lambda = 6h$:

$$\Sigma = \frac{A(\lambda = 6h)}{6h} \qquad (2.5)$$

This factor measures the magnitude of the surface slope variations due to topography at the boundary between region II and region III (figure 2.7). In general, Σ is very small in the interior of the ice sheet, increasing towards the edges of the ice sheet. Σ has a strong ($R^2 =60\%$) correlation with the surface slope of a DEM (digital elevation map) of Antarctica, smoothed to emphasize the large-scale slope of the ice sheet, and is negatively ($R^2=27\%$) correlated with the ice thickness.

In the Ross Embayment, there is a gradual transition from smooth ice surfaces in the interior, to rough surfaces in an intermediate region, to very smooth surfaces on Kamb ice stream, the inter-stream ridges and the Ross Ice Shelf. The ice stream trunks stand out sharply, with large Σ values comparable to the intermediate region. The correlation between surface slope and spectral roughness is opposite the general trend on the ice streams: The ice stream trunks have very low surface slopes on the order of 5×10^{-3}, yet have large spectral roughness, while the inter-stream ridges have surface slopes on the order of 10^{-2} yet have very small spectral roughness.

2.6 A model of ice-sheet surface topography

In the previous section, we showed that the properties of ice sheet surface spectra are spatially uniform when the spectra are represented as a function of λ/h. This suggests that the transfer of basal topography is a dominant factor in determining the shape of the surface spectrum.

In this section we derive a model to describe the statistics we expect for ice-sheet surfaces based on simple assumptions about the statistics of the ice-sheet bed and one of the most complete models of transfer, developed by Reeh (1982) and Gudmundsson (2003). We will refer to this model as a Red Bed Transfer (RBT) model, because it describes the statistics

log₁₀(surface slope)

log₁₀(surface slope)
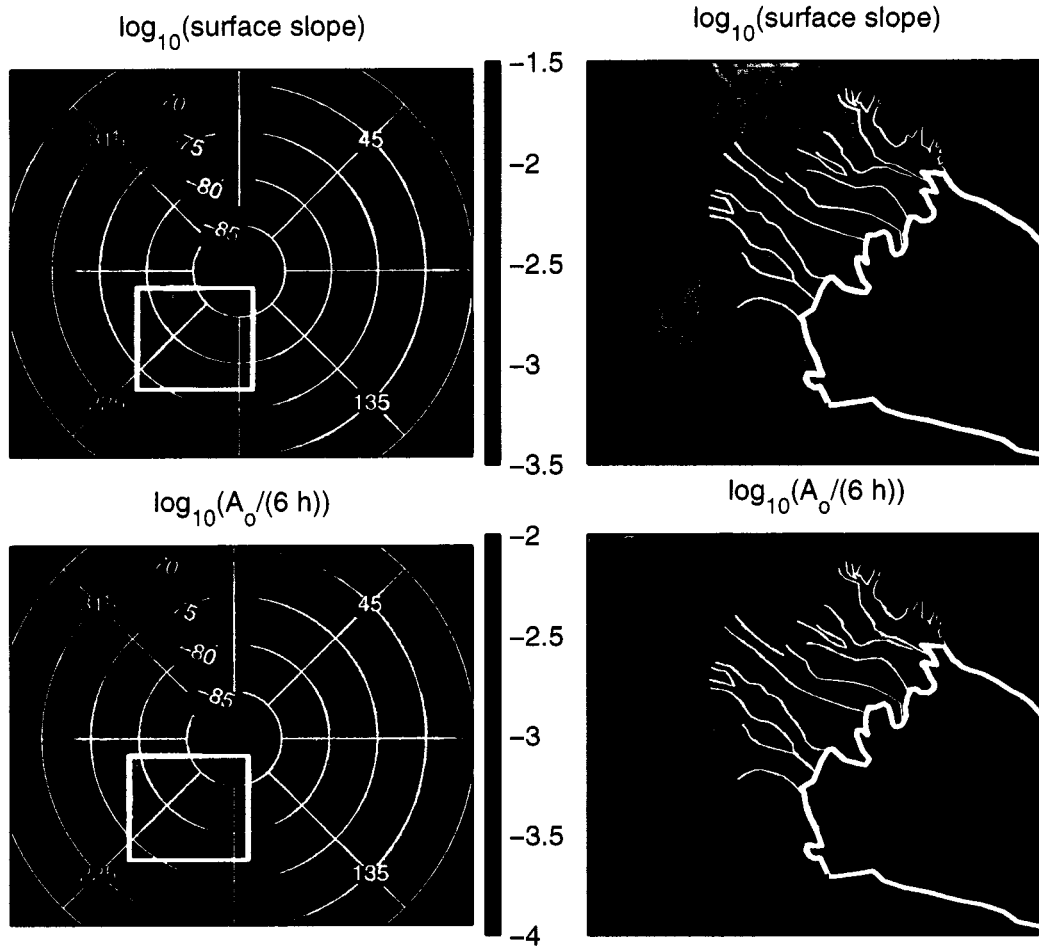
Figure 2.7: Top: magnitude of ice sheet surface slope, calculated on a 40 km baseline, on a log scale. Bottom: the spectral roughness at $\lambda = 6h$, on a log scale. Left hand plots show the entire continent, the right hand plots show the Ross Embayment. In all maps, undefined values are shown in black, and left and right column plots have a common color scale in the center.

of a red-noise bed, transferred to the the surface. The model is made up of two parts: A spectral description of the ice sheet bed that states that the bed has statistical properties like those observed in a variety of land surfaces, and a glacier model that describes the spectrum of the ice sheet surface for a given bed topography. We address each in turn below.

2.6.1 Model bed statistics

In our model, the bed is described by an isotropic spectral power-law model, where the spectral amplitude, $B(\mathbf{k})$ is found:

$$B(\mathbf{k}) = \frac{B_o}{N} \|\mathbf{k}\|^{-\gamma}. \tag{2.6}$$

$\mathbf{k}$ is the wavenumber vector for components on the bed; each component has wavelength $\lambda = 2\pi/\|\mathbf{k}\|$ and strike azimuth $\tan^{-1}(k_y/k_x)$. γ is the bed spectral exponent which measures the slope of a log-log plot of bed spectral amplitude versus wavelength. For spectra measured on a variety of earth-surface topography, γ has values between 10 and 15 dBa/decade (Turcotte (1992), Gagnon and others (2003)), although Austin and others (1994) suggest that published γ values may often be underestimates, because of spectral leakage problems. N is a normalization factor that lets us specify that profiles extracted from the bed at unit wavenumber will have a variance of B_o^2: The Fourier Slice theorem (see appendix A) gives the variance for a profile at wavelength λ_o (corresponding to wavenumber magnitude $\|k_o\|$):

$$B(k_o)^2 = \int_{-\infty}^{\infty} \frac{B_o^2}{N(k_o)^2} (|k_o|^2 + k_1^2)^\gamma dk_1 \tag{2.7}$$

Setting $B_o^2(k_o) = 1$ and integrating we find

$$A(k_o) = \frac{B_o}{N} |k_o|^{-\gamma+1/2} \sqrt{\frac{\sqrt{\pi}\Gamma(\gamma - 1/2)}{\Gamma[\gamma]}}. \tag{2.8}$$

This shows that one-dimensional profiles extracted from the two-dimensional bed have spectral exponents of $-\gamma+1/2$, or between 5 and 10 dB/decade for typical land surfaces. Solving equation 2.8 for N with $|k_o| = 1$ gives

$$N = \sqrt{\frac{\sqrt{\pi}\Gamma(\gamma - 1/2)}{\Gamma[\gamma]}}. \tag{2.9}$$

Evaluating 2.9 for $|k_o| = 1$ gives a bed with a variance of B_o^2 at unit wavenumber (i.e. for $\lambda = 2\pi$). Numerical values of N vary between 1.4, for $\gamma = 1.5$ and 1.7, for $\gamma = 1$.

2.6.2 Transfer of bed statistics to surface statistics

We predict the statistics of the surface of a glacier flowing over the bed described above using the transfer theory developed by Reeh (1982) and expanded by Gudmundsson (2003)

to include the effects of sliding. This transfer theory is based on a perturbation analysis of a Newtonian viscous fluid flowing over a rough bed. The analysis takes into account the full force-balance for viscous flow, allowing it to accurately represent short-wavelength features that are not treated by models using the shallow ice approximation. Raymond and Gudmundsson (2005) showed that, even though this model approximates variable ice viscosity with a constant value, it gives very similar results to a fully nonlinear model of ice flow for bed amplitudes up to 10%, for a broad range of wavelengths.

The relationship between bed topography, sliding variations at the bed, and surface topography is described by transfer coefficients relating the Fourier spectrum of the surface $S(\mathbf{k})$ and spectrum of the bed $B(\mathbf{k})$ and the spectrum of the basal sliding rate $C(\mathbf{k})$:

$$S(\mathbf{k}) = T_{sb}(\mathbf{k}, \alpha, C_o)B(\mathbf{k}) + T_{sc}(\mathbf{k}, \alpha, C_o)C(\mathbf{k}). \qquad (2.10)$$

The transfer coefficients T_{sb} and T_{sc} are complex functions of the non-dimensional wavenumber, $\mathbf{k}$, (defined as the 2D wavenumber times the ice thickness) and two datum parameters α and C_o that describe the local state of the glacier. Both datum parameters are non-dimensional: α gives the regional surface slope and C_o gives the mean rate of sliding at the bed divided by the rate of deformation of the ice between the bed and the surface. Surface topography comes about as a result of both topography and drag variations at the bed, expressed by $C(k)$, which gives spatial variations in the sliding rate, in units of the deformation speed. However, the equations given by Gudmundsson (2003) for T_{sc} show that the short-wavelength topography of the surface is much more strongly influenced by the bed topography for C_o less than about 100, allowing us to neglect the T_{sc} term in equation 2.10 in describing topography for $\lambda < 100h$ and slow sliding.

One dimensional profiles extracted from surfaces with spectra given by equation 2.10 have expected amplitudes given by the Fourier Slice Theorem:

$$S(\lambda, \hat{\mathbf{x}}) = \left(\int_{-\infty}^{\infty} (T_{sb}(2\pi/\lambda + t\hat{\mathbf{t}}, \alpha, C)B(2\pi/\lambda + t\hat{\mathbf{t}}))^2 dt \right)^{1/2}, \qquad (2.11)$$

where $\hat{\mathbf{x}}$ is the unit vector parallel to the profile direction, and $\hat{\mathbf{t}}$ is the unit vector perpendicular to $\hat{\mathbf{x}}$. This integral is calculated numerically.

2.6.3 Model surface statistics

Figure 2.8 shows the predicted ice-sheet surface if there is no sliding at the bed (C_o=0). The transfer coefficients have very small amplitudes at short wavelength, increasing rapidly with wavelength over the range $H < \lambda < 10H$. This implies that if the bed is red noise, the ice-sheet surface is very red noise over this range of wavelengths. Figure 2.9 shows two elevation profiles extracted from the surface in figure 2.8 and the expected Fourier spectrum for each. The amplitude increases strongly with wavelength for short wavelengths, then levels out at long wavelength to a slope more comparable to the spectral exponent of the bed. The model spectral exponent appears to change between the short-wavelength limit and the long-wavelength limit at about $\lambda = 3h$, rather than the $\lambda \approx 6h$ commonly observed for field profiles. Because the transfer coefficients are anisotropic, the amplitude of the profile varies by about a factor of two, depending on the azimuth of the profile relative to the ice-flow direction. However, the shape of the spectrum of the profile is not strongly sensitive to the azimuth.

Model spectral exponents

Following section 2.5.2, we calculate the spectral exponents for region II and region III of the predicted surface spectra, for non-dimensional wavelength intervals $h < \lambda < 6h$ for region II and $6h <= \lambda < 20h$ for region III. The choice of the boundary between region II and region III at $\lambda = 6h$ fits field profiles better than it does model profiles, but because the transition between region II and region III is not very distinct for either, the spectral exponents derived in this way should be comparable between the two.

Figure 2.10 shows the dependance of the short-wavelength spectral exponent, the long-wavelength spectral exponent, and the overall amplitude on the sliding rate C_o. Values of C_o greater than zero tend to enhance transfer amplitudes between $\lambda = 2h$ and $\lambda = 10h$. This makes the long-wavelength slope shallower and the short-wavelength slope steeper, and increases A_o. For sufficiently large sliding, this leads to a local maximum in transfer for λ in region III between 8 h and 12 h, so the transfer decreases slightly with wavelength over region II, leading to mildly negative values of the region III spectral exponents between
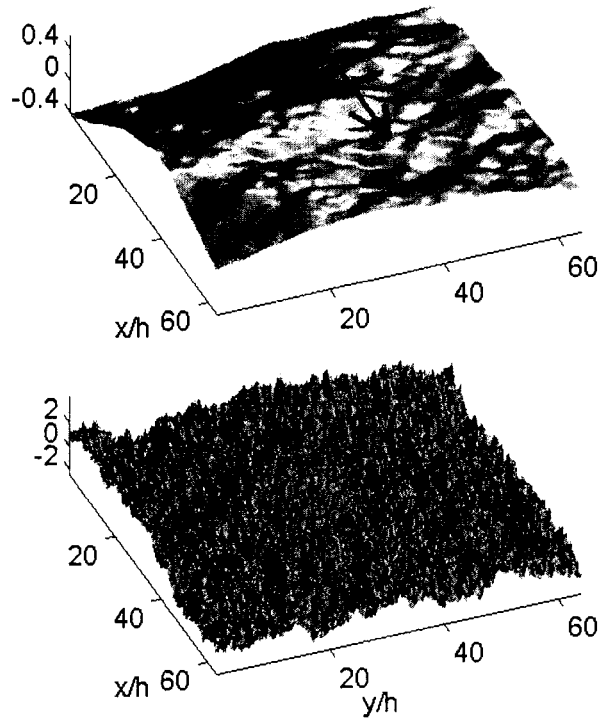
Figure 2.8: Synthetic bed and surface elevation topography from an RBT model. Bottom: Bed elevation for $\gamma = -1.25$ and $B_o = 1$. Top: Surface elevation for $C_o = 0$ and $\alpha = 1°$. Ice flow is from upper left to lower right, as shown by the arrow. x and y scales are in units of h, the z-scale is arbitrary.

$C_o = 60$ and $C_o = 200$.

For surface slopes less than about $1.5°$, the spectral exponents are largely independent of α. In this range, the overall amplitude is proportional to α, because the transfer functions are linearly dependant on α. As α increases beyond $1.5°$, the long-wavelength transfer approaches 1.0, leading to smaller long-wavelength slopes, and A_o approaching a limiting value of 1.0.
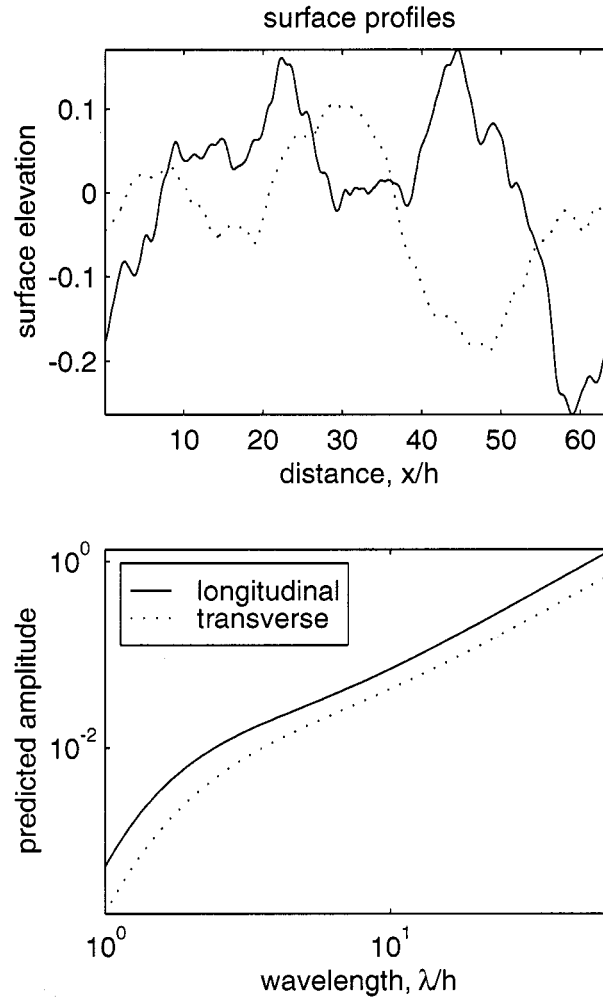
surface profiles

Figure 2.9: RBT profiles and expected RBT spectra. Top: Profiles extracted from the surface in figure 2.8. The solid line shows the profile taken transverse to flow for x=50 h, the dotted line shows the profile parallel to flow for y=50 h. Bottom: Expected spectra for the profiles in the top panel.

Bed amplitudes required for surface amplitudes

In the RBT model, three main variables determine the amplitude at any given point in surface amplitude map for wavelength λ_o: The bed-amplitude scale, B_o, the surface slope, α, and the ice thickness, h. B_o and α set the amplitude of the bed and the transfer, respectively, while the ice thickness determines the non-dimensional wavelength in the transfer function.
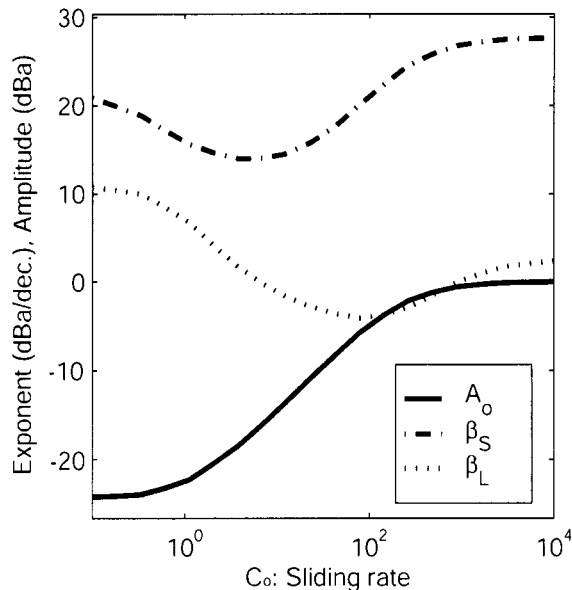
Figure 2.10: Model characteristics from equation 2.4 calculated for synthetic ice-sheet topography for $\alpha = 0.01^{o}$ for profiles running at 45° to the flow-direction.

At any given wavelength, for constant B_o and α, an ice surface for thick ice will have a smaller amplitude than an ice surface for thin ice because the transfer amplitude is weaker for increasing λ/h. This dependance on non-dimensional wavelength implies that on a log-log scale, surface spectra as a function of λ/h will run parallel to one another.

Comparing the values of A_o for a bed with unit roughness with the recovered values of $\hat{A}_o$, we can infer bed amplitude $\hat{B}_o$ required to produce the surface amplitudes seen here:

$$\hat{B}_o = \frac{\hat{A}_o}{A_o(\alpha, C)} \frac{N(\lambda_o = 2\pi h, \gamma)}{N(\lambda_o = 6km, \gamma)} \qquad (2.12)$$

Here A_o is the theoretical value, normalized to give unit amplitude at $\lambda = 6km$, and the ratio of N values corrects for the fact that $\hat{A}_o$ measures surface amplitude that refer to different parts of the (dimensional) **k** plane. We estimate α from a map of Antarctic surface elevation derived from ICESat data, smoothed by convolution with a 40 km wide Gaussian kernel and differentiated on 40 km baselines. If we assume that C_o is uniformly equal to zero, (Figure 2.11) we find that the required bed amplitude is large everywhere, with values of a few hundred to a few thousand meters. Because the scale of bed relief comes from the

summation of multiple roughness components, the implied relief is on the order of 4-5 times larger than this, if the exponential bed-spectrum holds at long scales. Siegert and others (2005) showed that kilometer-high basal relief is not uncommon; Their results also suggest a smooth bed for the aurora subglacial basin (70-80°S, 100°E), where our roughness estimate is also quite small. However, the large values of our bed-amplitude estimates suggests that our modeling may underestimate the transfer in some parts of the ice sheet, leading us to overestimate the bed amplitude. It is also likely that curvature in the ice surface and changes in datum conditions (i.e. α, C_o, and the direction of the surface slope) may in some areas appear as long-wavelength topography. These do not necessarily result from bed topography, but our analysis does not necessarily separate them from long-wavelength topography, and their appearance at long wavelength may be reflected in our estimates of bed roughness.

In the inland part of the Ross Embayment, the implied bed amplitude for $C_o = 0$ is typical of other parts of Antarctica, with amplitudes of several hundred meters. Nearer to the coast, the inter-stream ridges have some of the lowest implied amplitude values (on the order of 10 m). By contrast, the ice streams have implied amplitude values on the order of several thousand meters, which is clearly unrealistic, because the ice is less than 1.5 km thick throughout this region. Further, Siegert and others (2004) showed that the beds of the ice streams are generally slightly smoother than the beds of the inter-stream ridges. The large implied bed roughness is probably a result of fast sliding at the bed: The ice streams are sliding with C_o values on the order of $10^2 - 10^4$ (Raymond and Gudmundsson (2005)). If the RBT model holds, the difference in transfer between the ridges and the ice streams, normalized for the surface slope, should be on the order of $10^{2.2}$, which is comparable to the observed amplitude difference. It is notable that Conway ridge has approximately 10 times the amplitude of the other ridges; this is probably due in part to a rougher bed (Siegert and others (2004)), and to sliding at the bed in this area, indicated by moderately enhanced surface velocities (Joughin and others (2002)).

log$_{10}$ implied bed amplitude at λ=6 km

log$_{10}$ implied bed amplitude at λ=6 km
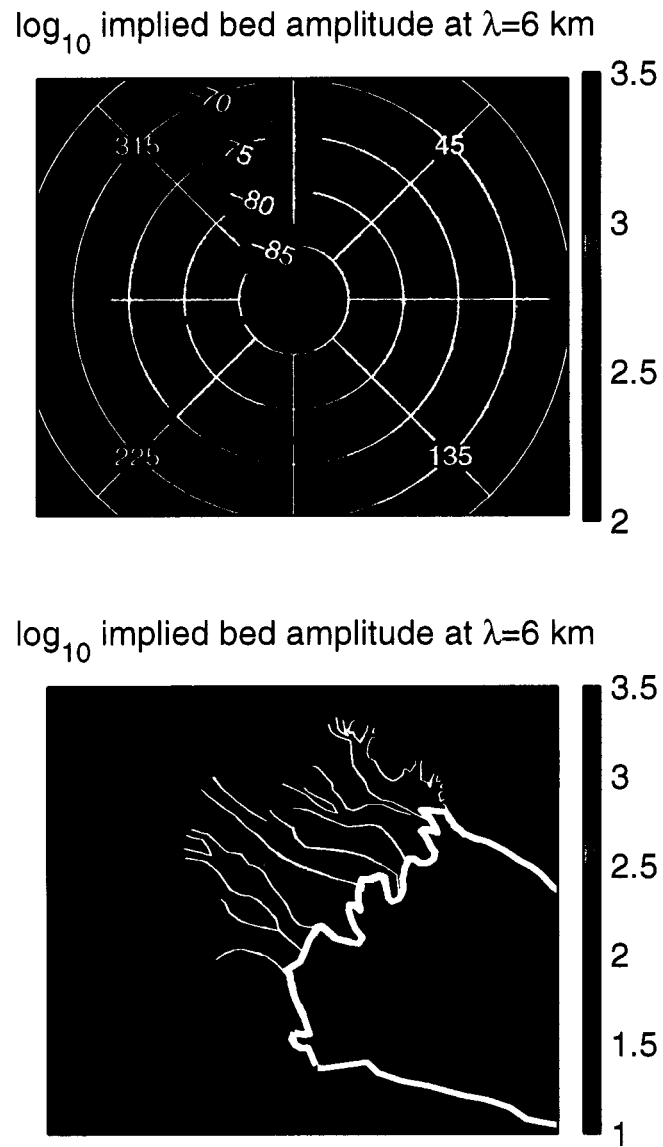
Figure 2.11: Bed amplitude at λ = 6 km required for measured surface amplitude, in $log_{10}(meters)$. Top: entire continent. Bottom: Ross Embayment.

2.7 Discussion

The spectral exponents calculated in section 2.5.2 for amplitude as a function of λ/h are in good agreement with those predicted by the RBT model for slow-sliding ice. Although

there are substantial local variations in calculated β_S and β_L, the values from the slow-sliding model, β_S=22 dBa/decade and β_L=10 dBa/decade are representative of measured spectra throughout the ice sheet. Some of the largest variations in the map of β_S in figure 2.6 coincide with the Megadune regions of East Antarctica (Fahnestock and others (2000)) which have increased surface amplitude at short wavelength. This is an example of a process that is not described by the RBT model that can nonetheless have a substantial impact on surface spectral properties.

The shape of the spectra derived in section 2.6.3 gives a clue as to why the spectral exponents for fixed λ intervals are strongly correlated with the ice thickness: The transition between region II and region III in the model curves is gradual, and the local spectral exponent becomes large at short wavelengths. If, for example, the spectral exponent is calculated for region II between 2 and 12 km when the ice thickness is 4 km, the spectral slope recovered will reflect non-dimensional wavelengths between 0.5 and 3, giving a steeper spectral exponent than would be recovered for the nondimensional region II, h $< \lambda/h <$ 6h.

There is a difference between the shapes of the model spectra and the measured spectra between $\lambda = 3h$ and $\lambda = 6h$. Measured spectral exponents change between the long-wavelength range (region III) and the short-wavelength range (region II) close to $\lambda = 6h$, while model spectral slopes change at approximately $\lambda = 3h$. This difference is difficult to quantify accurately because of scatter in the measured spectra and because the transition is gradual in either case. Raymond and Gudmundsson (2005) showed that transfer functions calculated for nonlinear ice viscosity have stronger amplitudes around $\lambda = 6h$ than do transfer functions for constant ice viscosity, which suggests that the difference between the model and the data comes about because the calculation of transfer functions with a constant viscosity model is an oversimplification.

The pattern of variation in the spectral roughness measured across the ice sheet also generally agrees with the RBT model: The roughness is large where the surface slope is large, and where the ice sheet is known to be sliding at its bed. The bed amplitude values required to produce the observed surface roughness are large, and in some cases imply bed relief exceeding the ice thickness. This may come about because in some areas the large-scale shape of the ice sheet appears as long-wavelength topography, although it does not reflect

transfer of bed topography of the surface. Alternately, it may suggest that sliding at the bed is more prevalent than we have estimated, or that our transfer model underestimates transfer in some areas.

Because increased bed roughness and faster sliding at the bed have similar effects on the surface roughness, our analysis cannot conclusively identify sliding regions of the bed from surface statistics alone. However, given measurements of bed roughness, it should be possible to use figure 2.10 to estimate whether the sliding rate is large for a given field survey site. However, precise recovery of C_o probably requires detailed knowledge of bed topography. Additionally, because the RBT theory used here does not include the effects of nonlinear ice viscosity or of thermal ice stratification, and because bed topography perturbations may be large compared to the ice thickness, the transfer theory may not give an accurate estimate of the roughness as a function of C_o.

2.8 Conclusions

Our work in this paper shows that ice elevation spectra have a characteristic shape as a function of the non-dimensional wavelength, λ/h: The spectra have steep spectral exponents for $\lambda < 6$ h and shallow spectral exponents for $\lambda > 6$ h. Typical surface roughness values for the center of the spectrum at $\lambda = 6h$ are on the order of 0.005 near the coast, and 0.0005-0.001 near the center of the ice sheet and on the inter-stream ridges of the Ross Embayment.

We approximately replicate these properties using an RBT model that predicts surface spectra with properties similar to as the measured surfaces. There are small but noticeable differences between measured and predicted spectra in the $\lambda = 4 - 6h$, but the predicted and measured spectra are broadly similar. The free parameters of RBT models are the bed amplitude, the sliding rate at the bed, and the ice thickness. This should allow researchers who need to model ice sheet surfaces to generate realistic synthetic ice-sheet surface data for a variety of glacial environments given these three parameters.

For the slow-sliding parts of the ice sheet, the major control on the shape of the model spectra is the ice thickness, and the major controls on the overall amplitude are the long-

wavelength surface slope, the bed amplitude, and the sliding rate at the bed. The effects of ice thickness and surface slope are borne out by correlations between spectral shape and ice thickness, and between amplitude and surface slope. The effects of sliding are borne out by data from the Ross Embayment ice streams, where we believe the bed to be of similar roughness between the ridges and the ice streams, but the surface roughness is a few hundred times larger on the ice streams. This helps to explain the distinctive appearance of the ice streams and ridges in sunlit optical imagery, in which the ridges appear very much smoother than the ice streams.

2.9 Appendix to chapter 2: A DEM from ICESat elevations

The Antarctic continent extends from about 65° S to the South Pole. While the 78% of the continent lying north of 81o has been mapped using satellite radar altimetry data, until very recently the best topography data for the area south of 81°, came from widely-scattered observations from a variety of local surveys. In some parts of the continent, the best data came from a balloon-based altimetry survey from the late 1970s.

An important benefit of the ICESat mission is that ICESat extends the area mapped by satellite altimetry from 81° S to 86° S. While ICESat elevations generally agree with older radar altimetry based DEMs north of 81° S, South of 81°, the difference between the two is on the order of 10-100 m (Bamber and Dans (2005)).

In this section I develop a new DEM (Digital Elevation Model] of Antarctica using ICESat data. This model gives novel results for the area between 81° S and 86° S, where older DEMs were constrained by few data. This DEM is designed to give accurate long-wavelength surface slopes for the continent, which are used in sections 2.5.2 and 2.6.

To match the available Bamber and Bindschadler (1997) and Lythe and others (2001) DEMs, I construct the DEM on a 5 km grid, centered on the South Pole, in a polar stereographic projection with a standard latitude of 71° S. To avoid aliasing short-wavelength components of topography, I select a subset of the data that includes only the median ICESat elevation for each grid-cell. I fit these median elevations with a cubic spline under tension (Smith and Wessel (1990)) that matches the data exactly, and interpolates the
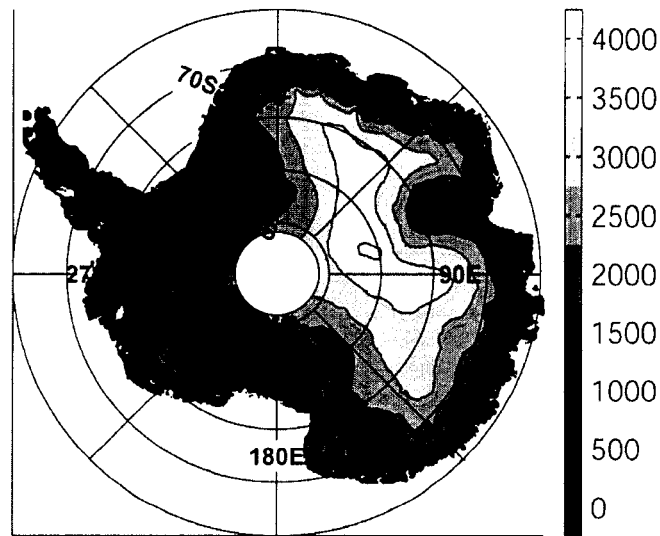
Figure 2.12: Contour map of the ICESat DEM, with elevations in meters. The gap in the center of the map reflects the 86° S limit of ICESat coverage.

elevations for unconstrained cells smoothly. Grid-cells falling more than 20 km from the nearest data point are marked as unconstrained.

Figure 2.12 shows a contour map derived from the ICESat DEM. At the scale at which this map is displayed, the elevations are indistinguishable from those given by Lythe and others (2001). The difference between the two DEMs is more easily seen in the surface slopes (figure 2.13). The ICESat DEM shows small-scale surface texture throughout the continent north of 86°, while the BEDMAP DEM is smooth south of 81° S. The BEDMAP DEM includes a few long-wavelength undulations in this area, but these do not accurately render the shape of the ice sheet, which is less complicated at long wavelengths than the BEDMAP data suggest. The ICESat DEM shows that the WAIS (West Antarctic Ice Sheet) divide is continuous between 81° S and 85° S, while the BEDMAP DEM shows the divide breaking up at about 83° S. Likewise, the ICESat DEM shows Dome Valkyrie (45° E) as sloping smoothly into a flat-ice area at the top of the Pensacola mountains (0° E), while the BEDMAP DEM shows several breaks in slope in this area.
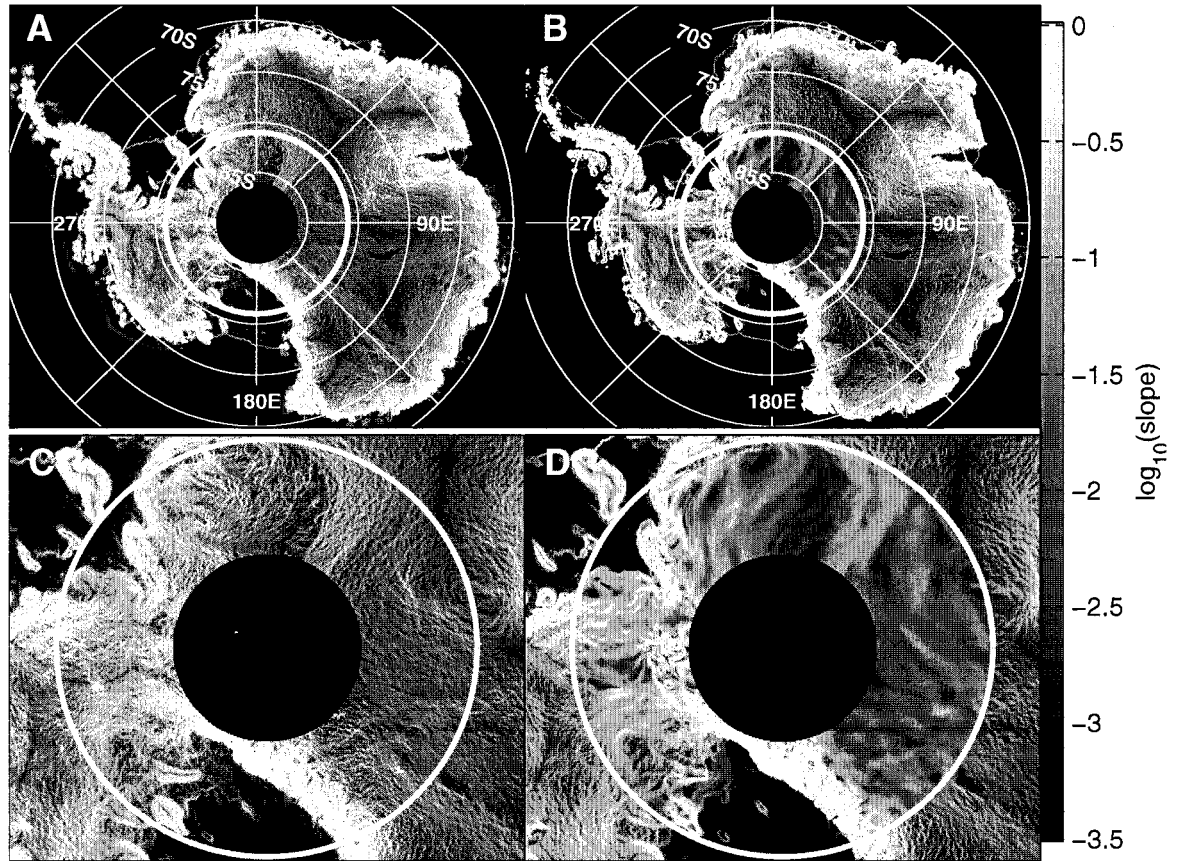
Figure 2.13: Surface slopes of the ICESat DEM (left column) and the BEDMAP DEM (right column). Gray-scales give the logarithm of the magnitude of the surface slope for elevations relative to the OSU91a geoid model. The heavy line shows the southern limit of radar altimetry coverage at 81° S, and both maps are masked south of 86° S to highlight the differences due to ICESat data. (A) and (B) show the ICESat DEM, while (B) and (D) show the BEDMAP DEM. (A) and (C) show the entire continent, (C) and (D) show the area immediately around 81° S, where the most significant differences between the DEMs are found.
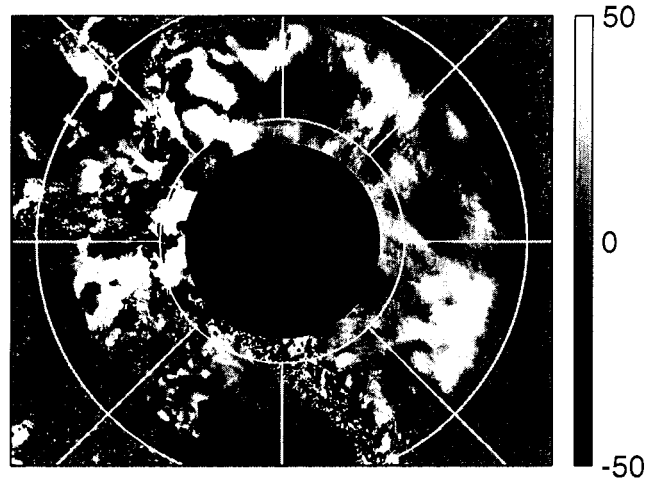
Figure 2.14: The difference between the ICESat DEM and the BEDMAP DEM south of 81° S. The gray-scale gives the ICESat DEM minus the BEDMAP DEM, in meters.

Figure 2.14 shows the difference between the BEDMAP DEM and the ICESat DEM. As Bamber and Dans (2005) suggested, the BEDMAP DEM contains errors on the order of 50 m over most of the area south of 81° S.

Chapter 3

VISCOSITY STRUCTURE OF THE ANTARCTIC ICE SHEET INFERRED FROM SURFACE UNDULATION SPECTRA

This paper is to be published as *Viscosity structure of the Antarctic ice sheet inferred from surface undulation spectra*, by Benjamin Smith and Melanie Raymond. Melanie Raymond was generous with her time in calculating the stratified-viscosity transfer coefficients used in this paper.

3.1 Summary

The Fourier spectra of ice-sheet elevation profiles from ICESat are compared to a model of ice topography. In this model, the bed is represented by a red-noise power-spectrum model and the ice is described as a Newtonian fluid whose viscosity varies exponentially with depth. The shape of the Fourier spectrum of the surface in this model is controlled by the degree to which near-surface viscosity exceeds near-bed viscosity. We compare predicted spectra with measured spectra across Antarctica, and find that a good statistical match obtains for a moderate range of stratification parameters. Comparable stratification parameters are expected based on analysis of non-linear, temperature-dependant ice viscosity taking into account horizontal and vertical strain rate induced by accumulation and other factors.

3.2 Introduction

The effective viscosity of ice varies with depth for two main reasons: First, ice viscosity is smaller for large applied stresses, so the large shear stresses near the bed result in an effective weakening of the ice. Second, warm ice flows more easily than cold ice, so in polar glaciers the ice at the bed is less viscous than that at the surface. These viscosity variations influence the distribution of stress within the glacier as it flows over bed topography, and hence the

relationship between bed topography and surface topography. At a large scale, the effective viscosity of the ice determines the relationship between surface slope, ice thickness, and ice flux (Nye (1952), Remy and Minster (1997)), and thus determines the overall shape of the glacier, and long-wavelength bedrock features may perturb the surface topography through this mechanism alone (Jóhannesson (1992)). However, perturbation analysis of transfer for features smaller than a few tens of ice thicknesses shows that transfer at short scales is independent of the mean viscosity of the glacier (Hutter and others (1981) Gudmundsson (2003)). The apparent difference between these results comes about because the large-scale flow processes that depend on ice viscosity are taken as part of the datum condition of the glacier around which the small-scale theories calculate perturbations.

While small scale transfer theory is independent of the mean ice viscosity, viscosity variations through the ice column can change the characteristics of transfer. Hutter and others (1981) showed the effects of nonlinear ice viscosity variations on transfer, and Jóhannesson (1992) separated the effects of shear across horizontal planes and longitudinal stretching in determining the vertical viscosity profile, and showed the effects of each on transfer. Gudmundsson and others (1998) showed how viscosity variations might be expressed in a three-dimensional transfer theory by approximating the variation of ice viscosity with depth with an exponential function, and Thorsteinsson and others (2003) showed transfer functions calculated with this theory for fast-sliding ice. These studies agree that the increased stiffness of the ice at the surface suppresses transfer at short wavelength, and can enhance transfer at wavelengths of about ten ice thicknesses.

Smith (2005) (chapter 2) showed that short-scale Fourier spectra of Antarctic ice sheet topography measured by ICESat (Ice Cloud and land Surface Satellite) are roughly consistent with a model in which red-noise bed topography is transferred to the surface by ice flow. However, the shape of these spectra vary over the ice sheet, and the significance of these variations was not fully explored. In this paper we compare the spectra of the ICESat elevation paper to spectra calculated for transfer from a red-noise bed to the surface by ice with viscosity variations due to thermal stratification and nonlinear ice flow. We adopt the approach of Gudmundsson and others (1998) and Schoof (2002) in approximating viscosity variations with an exponential model, which lets us express the ice viscosity variations in a

single parameter. We show that the observed spectral variations are statistically compatible with model spectral variations for stratification less than or equal to the stratification we expect for Antarctic conditions. The surface spectra are not statistically different from the unstratified model, but are statistically different from models with unrealistically large viscosity stratification.

Gudmundsson and others (1998) and Schoof (2002) both propose that linear-viscosity transfer theory can approximate transfer in ice with vertical temperature variations and power-law viscosity if the ice viscosity is allowed to vary exponentially with depth. Although Gudmundsson (2003) described the derivation of a transfer theory for ice with larger viscosity near the surface than near the bed, a description of the transfer functions has not been published, in part because the numeric calculations for this theory lead to numeric singularities when carried out in standard 32 bit floating-point arithmetic. In this paper, to avoid this problem we approximate the results of the full stratified-viscosity calculation by calculating the transfer coefficients for undulations running across the flow direction using the finite-element approach of Raymond and Gudmundsson (2005), then extrapolating these transfer coefficients to the entire $\mathbf{k}$ plane under the assumption that the anisotropy of the transfer coefficients follows the same pattern for stratified viscosity that it does for unstratified viscosity.

3.3 Data

All of the surface elevation measurements in this paper come from ICESat. ICESat measures ice-sheet elevations with a pulsed infrared laser, giving elevation measurements accurate to 5-10 cm in profiles along its ground tracks (Zwally and others (2002)). ICESat measurements represent the mean elevation of the laser footprint, which is about 70 m wide; this gives ICESat measurements much higher resolution than previous radar-altimetry missions, which had pulse-limited footprints 5-10 km wide. ICESat ground tracks converge at 86°S, and are separated by about 20 km at the northern edge of Antarctica.

Our data are ICESat level 2a ice-sheet elevations (GLA12), from the 2a, 3a, and 3b campaigns (October, 2003, October, 2004, and March, 2005). The laser 2 data are from re-

lease 21, the laser 3 data are from release 19. To remove apparent short-wavelength features caused by cloud-scattered surface returns, we reject returns for which the parameters in the GLA12 do not imply a clean return from a smooth ice-sheet surface: We do not use returns if the apparent surface reflectivity is less than 40 % or the apparent surface roughness is more than 2 m or the RMS difference between the digitized waveform and the best-fitting model waveform is more than 0.06 mV. These criteria reject about 45% of all returns.

3.4 Spectral Analysis

In this section we quantify spatial variations in the topography revealed by ICESat data. We use a windowed Fourier transform to derive measures of the spectral content of ICESat profiles for short segments of data, then map variations in each spectral component at a resolution of 20 km. These maps allow us to synthesize a spectral estimate for the ice-sheet topography at any point on the ice-sheet.

We estimate spectral amplitudes using a windowed Fourier transform:

$$A(k) = \frac{\sum_{j=1}^{N} W_j z_j e^{(-i2\pi(k\delta-1)(j-1)/N)}}{\sqrt{\sum_{j=1}^{N} W_j^2}} \tag{3.1}$$

where z_j are the N sampled surface elevation values, k is the wavenumber, δ is the measurement interval, and W_j is a spatial weighting function that reduces spectral leakage. The denominator in equation 3.1 normalizes the spectrum so that a sine wave of unit amplitude has a spectral amplitude of 1, regardless of the length of the profile. The amplitude values have units of meters. Amplitude spectra as a function of k may be expressed as a function of wavelength, λ, under the transformation: $\lambda = 2\pi h/k$.

Our procedures for mapping small-scale variations in spectral components of the ice elevation are described in Smith (2005), Chapter 2. We estimate spectra for short segments of GLAS profiles using equation 3.1 after filtering the data to avoid spectral aliasing. We interpolate between these amplitude estimates to map the spatial variations in each component at a resolution of 20 km, making separate maps for ICESat's ascending and de-

scending passes. The amplitude for each component of wavelength λ is estimated based on a profile with a length between 3λ and 6λ, so spatial variations in the shortest-wavelength components are resolved with resolution better than 20 km. At short wavelength, the profile spectra are dominated by shot-to-shot measurement noise. The noise magnitude varies depending on the surface characteristics of the ice sheet. In general, ice sheet spectra are dominated by noise for wavelengths shorter than 500 m, so we estimate the noise level for each spectrum from the mean spectral amplitude for 350 m$< \lambda <$500 m.

3.5 Model development

Our spectral analysis produces 31 maps of spectral amplitude, for wavelengths between 500 m and 87 km, with a noise estimate for each. Smith (2005) (Chapter 2) showed that there are strong similarities between the measured spectra and those predicted for red noise bed topography transferred to the surface by slow-flowing, constant-viscosity ice. In this section we extend this model to include the effects of stratified ice viscosity on the transfer.

3.5.1 Red-noise bed model

In our model, the bed is described by an isotropic spectral power-law model, where the spectral amplitude, $B(\mathbf{k})$ is found:

$$B(\mathbf{k}) = \frac{B_o}{N} \|\mathbf{k}\|^{-\gamma}. \tag{3.2}$$

$\mathbf{k}$ is the non-dimensional wavenumber vector for components on the bed; each component has wavelength $\lambda = 2\pi/\|\mathbf{k}\|$ and azimuth perpendicular to wave-crests of $\tan^{-1}(k_y/k_x)$. γ is the bed spectral exponent which measures the slope of a log-log plot of bed spectral amplitude versus wavelength. For measured statistics on a variety of earth-surface topography, γ has values between 10 and 15 dBa/decade (Turcotte (1992)). N is a normalization factor that lets us specify that profiles extracted from the bed at unit wavenumber will have a variance of B_o^2.

3.5.2 Transfer theory

The work in this section follows from the work of Gudmundsson (2003) and Raymond and Gudmundsson (2005). In Gudmundsson's theory, undulations on glacier surfaces reflect local variations in the bed topography and the drag it exerts on the glacier sole. Gudmundsson's model describes the ice-sheet as a parallel-sided slab of thickness h, with surface slope α, flowing in the x-direction, with the z coordinate measured above the unperturbed surface, so that $z < 0$ within the glacier. The effective viscosity of the ice varies with depth as:

$$\eta(z) = \eta_s e^{\Xi \frac{z}{h}}, \tag{3.3}$$

where Ξ is an adjustable parameter (the "stratification parameter") that determines the ice-viscosity variation with depth. Bed topography and basal drag variations give rise to perturbations in the ice-sheet surface, the relationship between the two being described by transfer coefficients relating the Fourier spectrum of the surface $S(\mathbf{k})$ and spectrum of the bed $B(\mathbf{k})$:

$$S(\mathbf{k}) = T_{sb}(\mathbf{k}, \alpha, C_o, \Xi)B(\mathbf{k}) + T_{sc}(\mathbf{k}, \alpha, C_o, \Xi)C(\mathbf{k}). \tag{3.4}$$

The transfer coefficients T_{sb} and T_{sc} are complex functions of the non-dimensional wavenumber vector, $\mathbf{k}$, (defined as the wavenumber times the ice thickness) and a set of datum parameters α, C_o and Ξ that describe the local state of the glacier. α is the regional surface slope, C_o is the rate of sliding at the bed in units of the deformation velocity, and Ξ is the logarithm of the ratio of the ice viscosity at the surface to the ice viscosity at the bed (see equation 3.3). Although surface topography comes about as a result of both topography and drag variations at the bed, the short-wavelength topography of the surface is much more strongly influenced by the bed topography when the datum sliding parameter C_o is less than $O(10^3)$. This allows us to neglect the T_{sc} term in equation 3.4 in describing topography for slow sliding and $\lambda < 100h$.

Figure 3.1 shows the transfer coefficients for $k_y=0$, for five values of Ξ. These curves follow the general pattern that as the stratification increases, transfer gets weaker for very short wavelengths ($\lambda < h$) and increases for wavelengths greater than 3-4 h. This behavior is very similar to the effects of increasing C beyond zero (Gudmundsson (2003)), except that
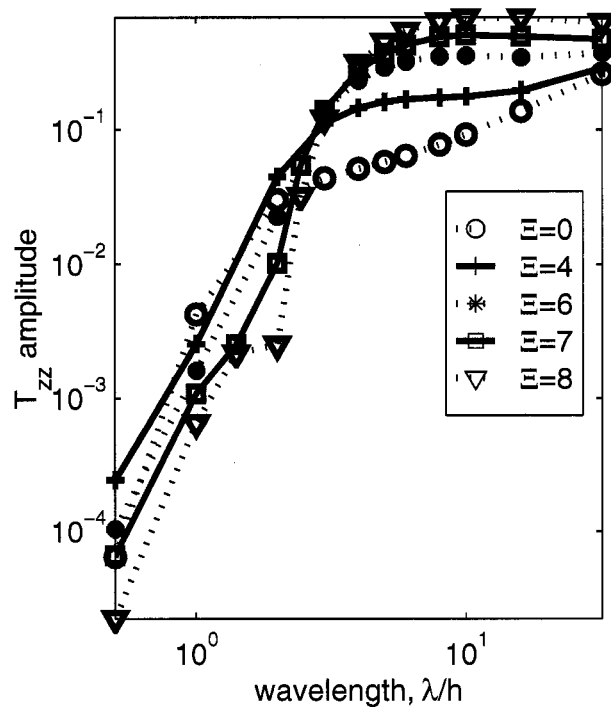
Figure 3.1: Transfer functions calculated for five values of Ξ.

for $C > 0$, the transfer at short wavelengths is mildly enhanced rather than suppressed. The similarity comes about because increasing Ξ effectively softens the ice near the bed, allowing the near-surface ice to move more freely, as if it were sliding over the weak basal ice. The suppression of short-wavelength transfer reflects the tendency for soft ice near the bed to take up strain at short wavelength without disturbing the near-surface ice. There are two areas where more complex behavior is apparent: The transfer at $\lambda = 0.5h$ for $\Xi = 0$ is smaller than that for other values of Ξ, and the curve for $\Xi = 8$ has a nearly constant value between $\lambda = 1.5h$ and $\lambda = 2h$. We do not have a good explanation for these features.

Because the finite-element calculation can give T_{zz} values only for $k_y = 0$, we extrapolate these transfer coefficients to the entire **k**-plane assuming that the relationship between $|T_{zz}(\theta, \lambda, \Xi)|$ and $|T_{zz}(0, \lambda, \Xi)|$ does not depend strongly on Ξ:

$$|T_{zz}(\theta, \lambda, \Xi)| = |T_{zz}(0, \lambda, \Xi)| \frac{|T_{zz}(\theta, \lambda, 0)|}{|T_{zz}(0, \lambda, 0)|}. \tag{3.5}$$

Here θ is the angle between the normal to the wave crests of the Fourier components and the ice-flow direction. The $\Xi = 0$ transfer function can be calculated from expressions given by Gudmundsson (2003).

3.5.3 Predicted surface statistics

Combining the statistical terrain models described in section 3.5.1 with the transfer model in section 3.5.2 gives a prediction of ice-sheet surface spectra. Under these assumptions, ice-sheet surface amplitude spectrum will be:

$$S(\mathbf{k}) = T_{sb}(\mathbf{k}, C, \alpha, \Xi) \frac{B_o}{N} |\mathbf{k}|^{\gamma}. \tag{3.6}$$

We can describe surface spectra over a given band of wavelengths with six numbers: the ice thickness, the sliding ratio, the surface slope, the stratification parameter, the bed amplitude, and the bed spectral exponent.

In figure 3.2 we predict the shape of the ice-sheet surface for a red-noise bed, for datum conditions with no sliding($C_0 = 0$). For a RMS bed amplitude of 1, the surface has an RMS amplitude of 0.2, and has a smoother appearance than the bed because long-wavelength features are transferred much more strongly than short-wavelength features.

Statistics of surface profiles

We predict the RMS amplitude of a surface profile by applying the Fourier Slice Theorem (equation A.6) to equation 3.6:

$$A(\lambda/h, \hat{\mathbf{x}}) = \left(\int_{-\infty}^{\infty} \left(\frac{B_o}{N} | \frac{2\pi h}{\lambda} \hat{\mathbf{x}} + t\hat{\mathbf{t}} |^{\gamma} S(\frac{2\pi h}{\lambda} \hat{\mathbf{x}} + t\hat{\mathbf{t}}) \right)^2 dt \right)^{1/2} \tag{3.7}$$

Here $\hat{\mathbf{x}}$ is the unit vector giving the profile direction relative to the ice-flow direction, and $\hat{\mathbf{t}}$ is a unit vector perpendicular to $\hat{\mathbf{x}}$. The term $2\pi h/\lambda$ is the wavenumber magnitude corresponding to the non-dimensional profile wavelength λ/h. We evaluate this equation numerically, calculating the transfer coefficients using equation 3.5.

Figure 3.3 shows the predicted spectra for slow-sliding ice for different values of Ξ and for different values of γ, for λ between 0.5 h and 30 h. The shapes of the spectra are
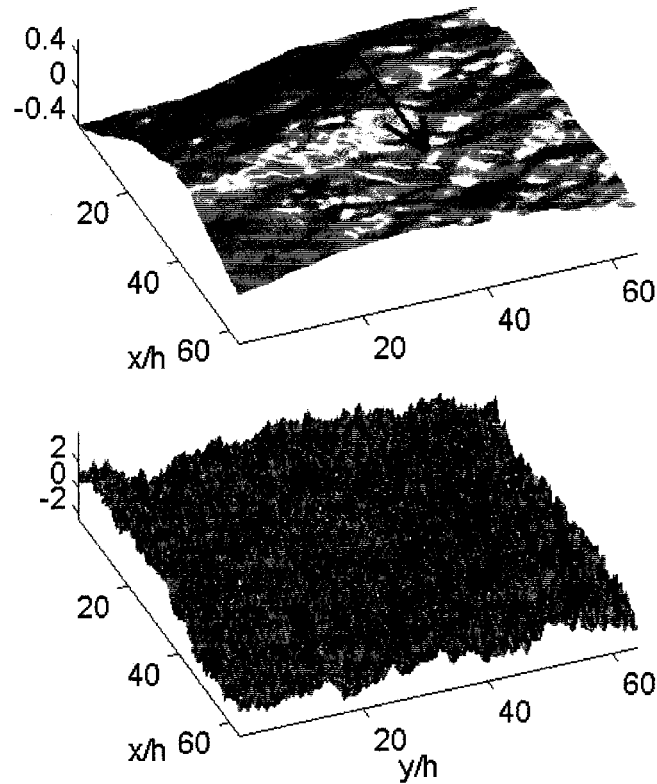
Figure 3.2: A red-noise bed (bottom) with $\gamma = -1.5$, with the predicted surface for $C_0 = 0$, with $\Xi = 0$, $\alpha = 1°$. The x and y axes are in units of ice thicknesses, the z scale is in arbitrary units, but note that the elevation scale in the surface plot runs from -0.4 to 0.4, while the bed scale runs from -2 to 2.

different mainly in that the $\Xi = 0$ and the $\Xi = 8$ spectrum fall off mode rapidly than the others as $\lambda \to 0$, and in that as Ξ increases, spectra have increasingly large amplitudes near $\lambda = 6h - 10h$. The $\Xi = 8$ curve has a feature near $\lambda = h$ that corresponds to the irregularity in the transfer curve seen in figure 3.1. Although the spectra are similar to one another for $\Xi < 6$, there are notable differences between the $\Xi = 0$ and the $\Xi = 8$ curves. These differences are of much larger magnitude than the possible variations in each curve due to the choice of γ.
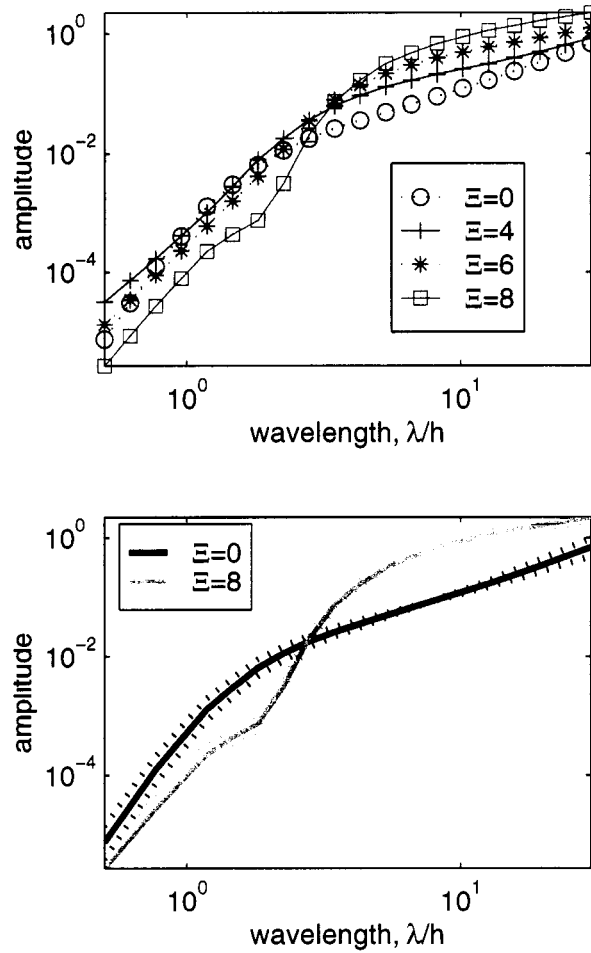
Figure 3.3: Top: Amplitude spectra for four values of Ξ. Profiles have datum conditions $C_0=0$, $\alpha = 1^o$ and run at 45° to the flow direction. Bottom: Spectra for $\Xi = 0$ and $\Xi = 8$. Solid lines are calculated for $\gamma = 1.25$, dotted lines show $\gamma = 1.0$ and $\gamma = 1.5$.

The RMS amplitude-versus-λ/h curves are smooth in λ. However, because the components of the bed spectrum have a random normal distribution around the red-noise $B(\lambda/h)$ curve, the amplitudes of the spectral components in a measured profile will be distributed around $A(\lambda, \hat{x})$ in a $\sqrt{\chi^2}$ distribution with two degrees of freedom. That is, that for amplitude measurements A_i, we expect $A_i^2/A^2(\lambda, \hat{x})$ to be distributed as χ_2^2. Since we will usually look at the logarithm of the surface amplitude, we plot in figure 3.4 the distribution of $log_{10}(A_i/A(\lambda, \hat{x}))$. 68% of the values in this distribution are within a factor of 0.55 of
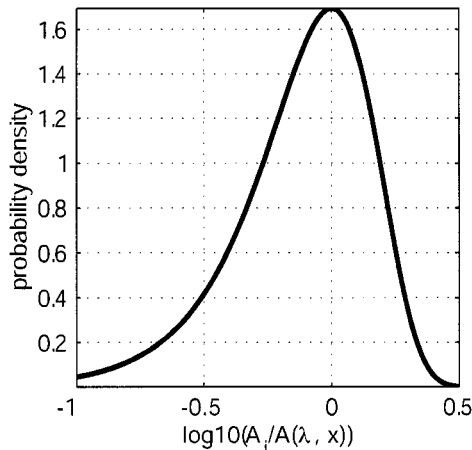
Figure 3.4: The probability distribution function for $log_{10}((A_i/A(\lambda, \hat{x})))$.

the median of the distribution, so the components of the measured spectrum are expected to be scattered within a factor $10^{0.55/2} \approx 1.9$ of the true spectrum. This large variability masks variations in $A(\lambda, \hat{x})$ smaller than a factor of two, and limits the precision with which spectral parameters can be recovered from measured profiles.

3.5.4 Spectral model matching

In this section we determine the range of Ξ for which RBT models are statistically compatible with measured surface spectra. For each cell in our spectrum maps, we determine α and θ from a digital elevation model of Antarctica (Smith (2005) chapter 2). We assume that for most parts of Antarctica, the best estimate of sliding is $C_o = 0$. We then search for combinations of the unknown parameters, $[B_o, \Xi, \gamma]$, that allow us to best match the measured surface amplitude spectra, $A(\lambda)$.

For seven different values of Ξ between 0 and 8, and for three values of γ between 1 and 1.5, we find the best value of B_o for each grid cell of our spectral maps. Based on the surface DEM, we select values of $\hat{x}$ and α, and generate a spectrum $A_u(\lambda, \Xi, \gamma)$, using equation 3.7, equal to the surface amplitude for a bed of unit roughness. The surface amplitude a bed with unit roughness is $B_o A_u(\lambda, \Xi, \gamma)$. We form an estimate of the bed amplitude, $\hat{B}_o$ by

minimizing:

$$R(\Xi, \gamma) = \left(\frac{1}{n_\lambda} \sum_{j=0}^{n_\lambda} \left(log(\hat{B}_o A_u(\lambda_j, \Xi, \gamma)) - log(A(\lambda_j)) \right) \right)^{1/2} . \qquad (3.8)$$

The summation is carried out for the n_λ components whose amplitude is at least twice the noise level and is less than 30 h. For our 31 amplitude maps, this means that n_λ may be between 1 and 28, although we ignore all results for $n_\lambda < 15$. We will refer to the minimum value of R for a given profile as $R_{min}(\Xi, \gamma)$. $R_{min}(\Xi, \gamma)$ measures the misfit between the best-fitting theoretical spectral model and the data for each value of Ξ and γ.

For a red-noise bed, the amplitudes of the components of the surface spectrum for a single profile should be distributed as described in section 3.5.3. The measured spectrum should be scattered around the predicted spectrum; even if the parameters for the predicted spectrum are correct, R_{min} will not be zero. We determine the expected distribution of R_{min} for different n_λ by Monte-Carlo simulation: We generate 8000 sets random of n_λ numbers with a $\sqrt{\chi_2^2}$ distribution and find R_{min} for each. We find that for typical values of n_λ between 16 and 28, 95% of any sample of R_{min} values should be less than R_{crit}, where R_{crit} is approximated by

$$R_{crit} = 0.37 - 0.0015(n_\lambda - 13) \qquad (3.9)$$

We take this as our misfit criterion: Any value of R_{min} greater than R_{crit} is interpreted as indicative of a significant difference between the model spectrum and the measured spectrum.

Figure 3.5 shows three spectra for different ice thicknesses from East Antarctica. (1), from lower Lambert Glacier, is best fit by a model with $\Xi = 6$, (2) from near the crest of Ridge D, is best fit by a model with $\Xi = 1$, and (3) from Dome Argus, is best fit by a model with $\Xi = 0$. The best residuals for the three models are 0.22 and 0.18, and 0.26 respectively, and all are fit best by curves for $\gamma = -1$. The thin-ice curve (1) has noise levels between 0.02 and 0.11 m, while the other two have noise levels on the order of 0.02 m. This allows $n_\lambda = 20$ for (1) and $n_\lambda = 21$ for (2) and (3). The best misfits for (1) and (2) are close to 0.2, while the best misfit for (3) is 0.26. The larger misfit for (3) appears to reflect enhanced surface amplitude for $\lambda \approx 3 - 6h$, which is not fit well by the model. This may come about
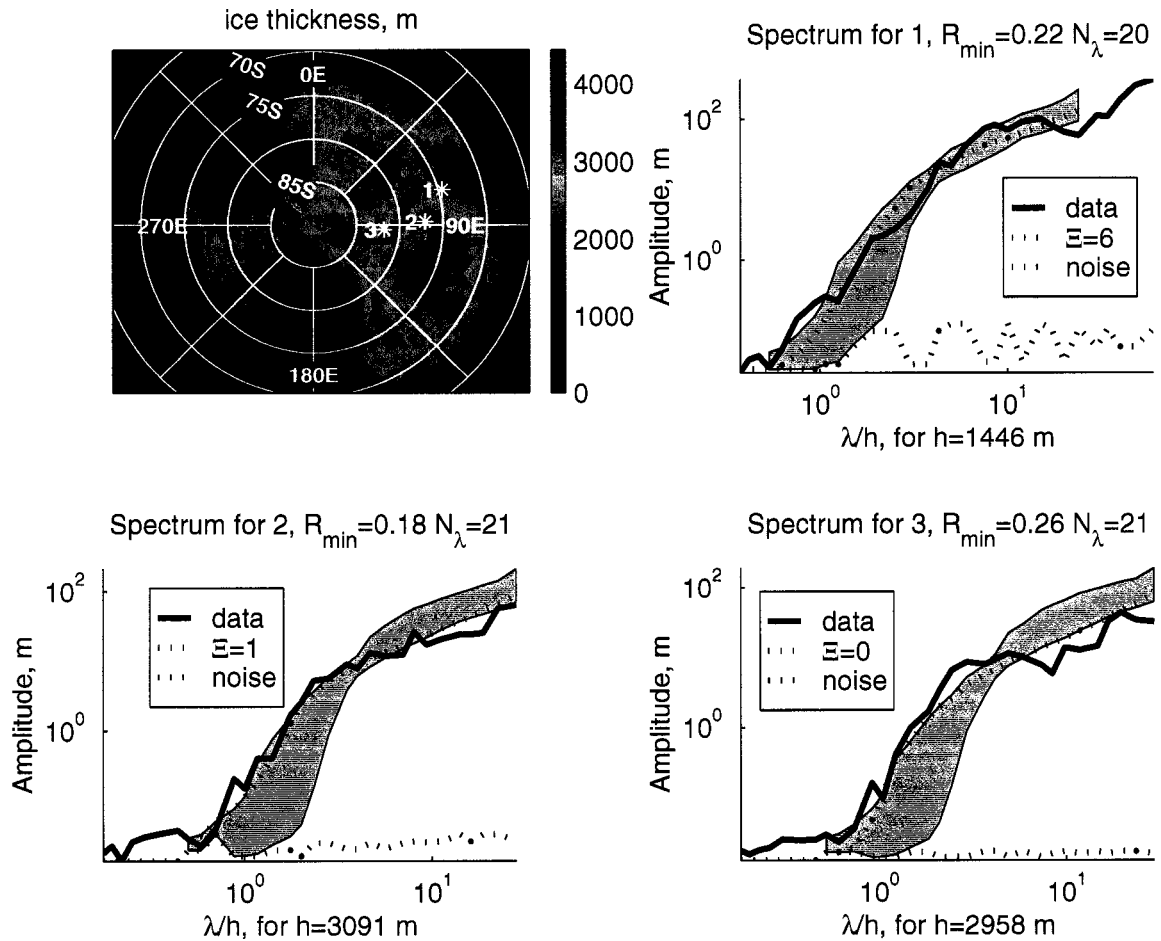
Figure 3.5: Ice thickness (Lythe and others (2001)), with two ascending-track spectra from East Antarctica. Spectrum locations are shown on the ice-thickness map. (1) is from near the Lambert Glacier grounding line, (2) is near the crest of Ridge D, and (3) is near the top of Dome Argus.. In the spectrum plots, the measured spectrum is shown in blue, the best-fitting model is shown in red, and the range of best-fitting models for different values of Ξ and γ is shown as a gray polygon. The noise level for the different spectral components is shown with a dotted black line.

because (3) is close to where megadunes, large aeolean surface features, are known to be common (Fahnestock and others (2000)).

Figure 3.6 shows maps of R_{min} for the best-fitting and worst-fitting models for ascending tracks. The best-fitting models have residuals on the order of 0.2, while the worst-fitting models have residuals up to 0.8. Most of the best-fitting values of R_{min} are smaller than
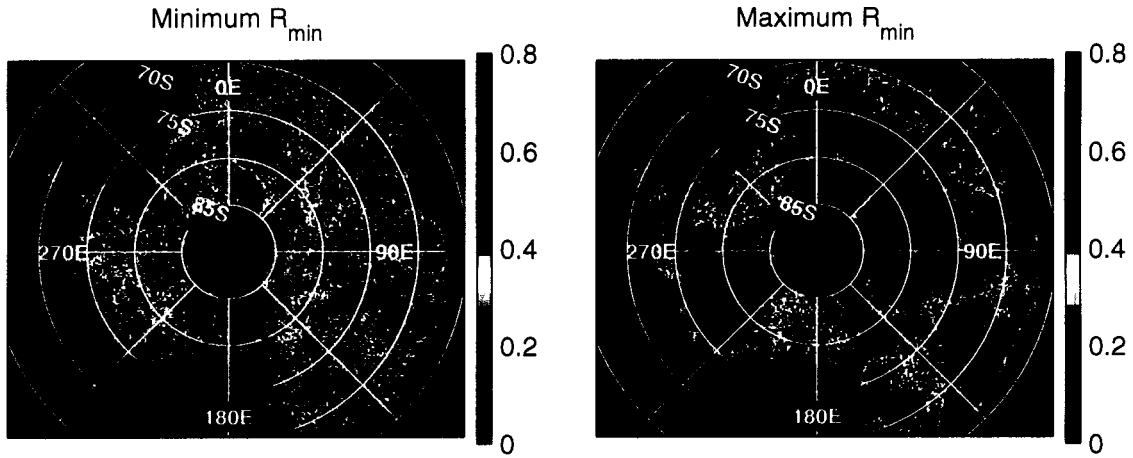
Figure 3.6: Values of R_{min} for the best-fitting (left) and worst-fitting (right) stratified-viscosity spectral models. No model fit was possible in areas shown in black, usually because of very thin ice.

our misfit criterion, so the differences between the best-fitting models and the data are not significant. The descending tracks show essentially the same patterns, and are not shown.

The choice of γ in the minimization does not strongly influence the results. 90% of the data are best fit by a model with $\gamma=-1$, although the difference in R_{min} between models with $\gamma = -1$ and models with $\gamma = -1.25$ is typically less than 0.02, so the difference between models due to different γ values is not usually significant.

Figure 3.7 shows the range of Ξ values for which $R_{min} < R_{crit}$. For 98% of the continent, models with Ξ as small as 0 are not significantly different from the measured spectra. The maximum values of Ξ range between 0 and 9, but about 80% of all models have maximum acceptable values of Ξ less than 7, and fewer than 4% of the measured spectra are compatible with $\Xi = 8$.

3.6 Analysis

The model fitting was performed in terms of the model parameter Ξ. In this section we show how glaciological parameters determine the effective viscosity of ice, and the values of Ξ that correspond to different sets of glaciological parameters. We show that for reasonable
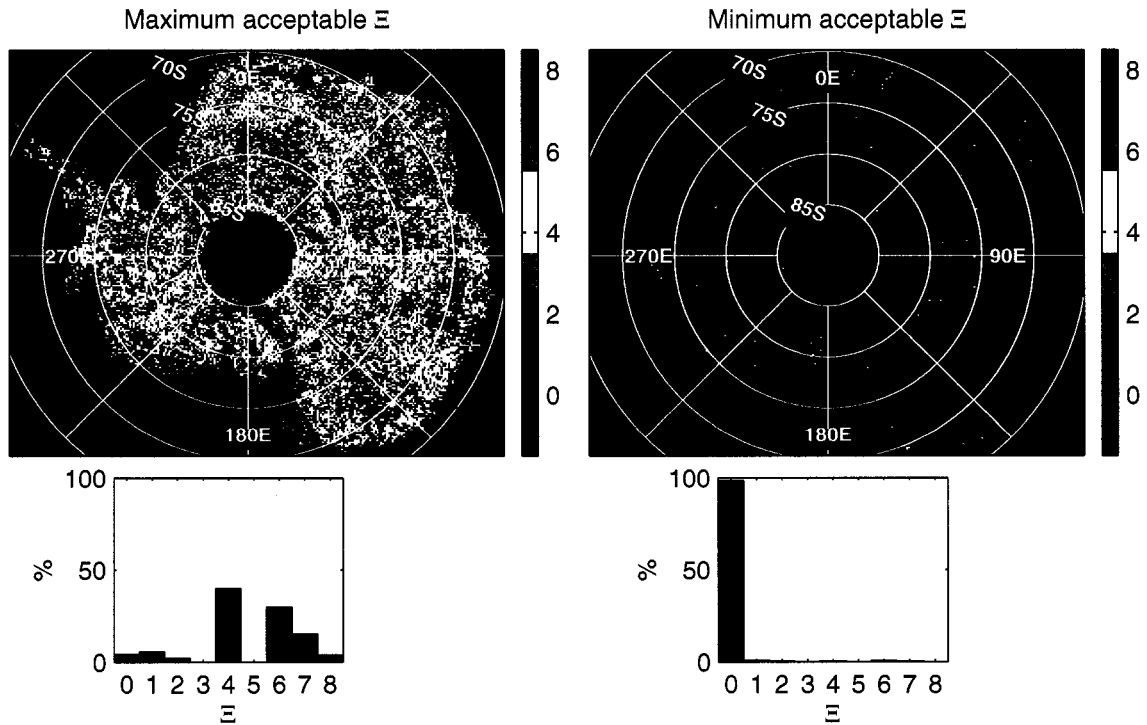
Figure 3.7: Maximum (left) and minimum (right) values of Ξ for which the best-fitting residual is less than 0.29. Where n_λ <15, no R is calculated and the maps are colored black.

estimates of glaciological parameters across Antarctica, most Ξ-values are expected to be between 4 and 7.

3.6.1 Approximating nonlinear ice viscosity variations with an exponential model

The transfer-model depends strongly on the viscosity-stratification parameter Ξ. This parameter gives variation in the viscosity between the bed and the surface, which in the model has an exponential variation (equation 3.3). Conventional models of ice-sheet dynamics calculate ice-viscosity using Glen's law (Paterson (1994)), which gives a more complicated variation of viscosity with depth; Gudmundsson's model lets us choose a value of Ξ that lets the dynamics of the model best match the full dynamics due to Glen's law. In this section we describe the calculation of viscosity using Glen's law. We consider the viscosity and the

best fitting Ξ for simple shearing flow, then consider the changes in the viscosity factor and in Ξ when the effects of stretching of the ice column due to horizontal ice flux divergence and of temperature variations are considered.

We analyze ice viscosity based on Glen's law with a temperature-varying rate factor A. In this analysis, we expect the viscosity of ice to vary between the bed and the surface principally because of temperature variations and nonlinear strain dependence. These effects are given by Paterson (1994):

$$\eta_{Glen} = 1/2(A(T)\tau_{eff}^{n-1})^{-1}, \tag{3.10}$$

where $A(T)$ is the temperature-dependent rate factor and τ_{eff} is the effective stress, given by the quadratic sum of the deviatoric stress components. We take the creep stress exponent, n, to be equal to 3.

The effective stress depends on the flow-parallel shear stress, τ_{xz}, and the deviatoric stress due to horizontal extension, s_{xx} and s_{yy}, and vertical extension, s_{zz}. We assume that other stress components are negligable.

$$\tau_{eff}^2 = \tau_{xz}^2 + s_{xx}^2 + s_{yy}^2 + s_{zz}^2. \tag{3.11}$$

The flow-parallel shear-stress has an approximately linear variation with depth:

$$
\begin{aligned}
\tau_{xz} &= -\rho g \alpha z \\
&= \tau_d \frac{z}{h}
\end{aligned}
\tag{3.12}
$$

where ρ is the density of ice, g is the acceleration due to gravity, α is the surface slope, and z is the vertical coordinate relative to the unperturbed ice surface. Within the glacier, $z < 0$, and at the bed, $z = -h$. τ_d is the driving stress, equal to the shear stress at the bed.

We select values of Ξ by matching $\eta_{exp}(z, \Xi, \eta_o)$ to $\eta_{glen}(z)$ in a log least-squares sense, minimizing

$$\int_o^h (log(\eta_{glen}(z)) - log(\eta_{\exp}(\Xi, \eta_o, z)))^2 dz \tag{3.13}$$

Minimizing the squared difference in log viscosity is roughly equivalent to minimizing the fractional difference between the two viscosity models.

Viscosity variations due to temperature

In a polar glacier, ice near the bed is warmer than the the near-surface ice because geothermal heat warms the bed. As a first approximation, we will assume that the temperature is a linear function of depth.

$$T(z) = T_s + \frac{z}{h}(T_s - T_b), \tag{3.14}$$

were T_s and T_b are the surface and bed temperatures. We ignore the effects of the vertical advection of cold ice, which tends to cool the ice column near the surface, with decreasing effects towards the bed.

Since warm ice has a smaller effective viscosity than cold ice, basal ice is much softer than near-surface ice. We approximate the ice-stiffness-versus-temperature relationship with an Arrhenius-type relationship:

$$A(T) = A_o e^{-Q/RT} \tag{3.15}$$

where Q is the creep activation energy of $Q = 6$ kJ mol^{-1} and $A_o = 4.1 \times 10^{-7}$ Pa a^{-1} (Paterson (1994)). For a polar glacier with T_s=238 K and T_b=273 K, $A(T)$ varies by about a factor of 14 between the bed and the surface.

Viscosity variations for simple shearing flow

Taking into account only viscosity variations due to a nonlinear ice-flow law, the variation of viscosity with depth is

$$\eta_{Glen} = \frac{1}{2} \left(A(T)\tau_d^{n-1}(-z/h)^{n-1} \right)^{-1}, \tag{3.16}$$

For n=3, η_{Glen} varies as z^{-2}, and is singular near the surface, where $\eta_{Glen} \to \infty$. Since we cannot evaluate equation 3.13 at the surface, we minimize the misfit (equation 3.13) for $0.01h \leq z \leq 0.99h$. This range of depths captures the range of viscosity variations, but avoids the singular value at the surface. If we do not take temperature variations into account, the best-fitting value of Ξ is 5.9. Temperature variations introduce a nearly-exponential variation of $A(T)$ with depth to equation 3.16. The best-fitting value of Ξ is then the sum of the Ξ for nonlinear viscosity alone and $log(A(T_{bed})) - log(A(T_{surf}))$. For $T_s - T_b$=-25 k, this increases Ξ to 8.5.
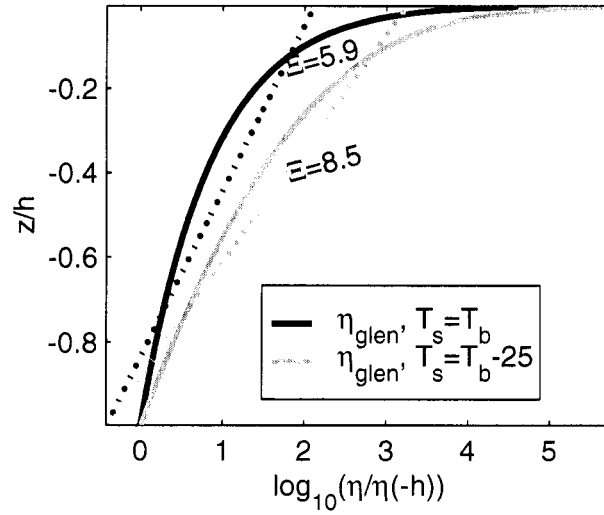
Figure 3.8: Viscosity variations due to nonlinear viscosity and temperature for ice in simple shear. The log of the viscosity divided by the viscosity at the bed is shown as a function of z/h for the Glen's law models (solid curve) and for the best-fitting exponential model (dotted curve). One set of curves is shown for an isothermal model, another for a model with T_s - T_b = -25 K.

Figure 3.8 shows the log viscosity as a function of depth and the best-fitting exponential viscosity for isothermal ice and for ice with $T_s - T_b = -25$ K.

Viscosity variations for simple shearing flow with horizontal divergence

In ice sheets and glaciers in steady state, ice accumulation at the surface is balanced by thinning of the ice column due to horizontal stretching:

$$\dot{b} = \int_{-h}^{0} (\varepsilon_{xx}(z) + \varepsilon_{yy}(z))dz \tag{3.17}$$

In two dimensional flow, $\varepsilon_{yy}=0$, and $\varepsilon_{zz} = -\varepsilon_{xx}$. Following Reeh (1987) we assume $\dot{\epsilon}_{zz}(z)$ varies with depth as

$$\dot{\epsilon}_{zz}(z) = \frac{\dot{b}}{h}\frac{u(z)}{u(0)}\frac{1}{<u(z)/u(0)>}, \tag{3.18}$$

where $u(z)$ is the horizontal velocity and $<>$ indicates a vertical average. To allow a closed solution we assume that the shape factor, $u(z)/(u(0) < u(z)/u(0) >)$, is adequately

represented by that for isothermal ice in simple shear:

$$\frac{u(z)}{1/h \int_{-h}^{0} u(z')dz'} = \frac{5}{4}\left(1 - \left(\frac{z}{h}\right)^4\right)$$

(3.19)

The strain-rate at the bed is zero, and the strain rate at the surface is $1.2\dot{b}/h$.

The stretching of the ice results in a stress-deviator component, s_{zz}, that contributes to the effective stress and softens the ice near the surface. According to Glen's law with $n = 3$, s_{zz} must satisfy:

$$\dot{\epsilon}_{zz} = As_{zz}(1/2(s_{xx}^2 + s_{yy}^2 + s_{zz}^2) + \tau_{xz}^2).$$

(3.20)

For two-dimensional flow, $s_{yy} = 0$ and $s_{xx} = -s_{zz}$, and

$$\dot{\epsilon}_{zz} = As_{zz}(s_{zz}^2 + \tau_{xz}^2).$$

(3.21)

This is a cubic equation in s_{zz}, which has one real root:

$$s_{zz} = \frac{6^{-1/3}K_1^2 - 2^{1/3}(\tau_{xz}^2)}{3^{1/3}K_1}$$

(3.22)

where

$$K_1 = \left(-9\frac{\dot{\epsilon}_{zz}}{A} + \sqrt{81\frac{\dot{\epsilon}_{zz}^2}{A^2} + 12\tau_{xz}^6}\right)^{1/3}.$$

(3.23)

For isothermal glaciers, s_{zz} depends on depth, the extensional strain rate, and the driving stress. We can express the relative importance of the shear strain rate and the extensional strain rate in determining the ice viscosity by the ratio of the extensional strain rate at the surface to the shear strain rate at the bed:

$$\Psi = \frac{\left(\frac{5}{4}\frac{\dot{b}}{h}\right)^{1/3}}{\frac{1}{2}A\tau_d^n}$$

(3.24)

Ψ is large for large accumulation rates, small surface slopes, and thin ice. For a coastal glacier with $h = 500m$, $\alpha = 1°$, and $\dot{b} = 1$ m a^{-1}, $\Psi=0.1$. Ψ values are smaller for thicker inland ice with lower accumulation: a 2000 m thick glacier, with a surface slope of 0.1° and an accumulation rate of 0.05 m a^{-1}, has $\Psi = 0.025$.

Figure 3.9 shows the variations in s_{zz}, τ_{xy} and τ_{eff} for different values of Ψ. Ξ values are large when Ψ is small, because small Ψ reflects large viscosity differences between the
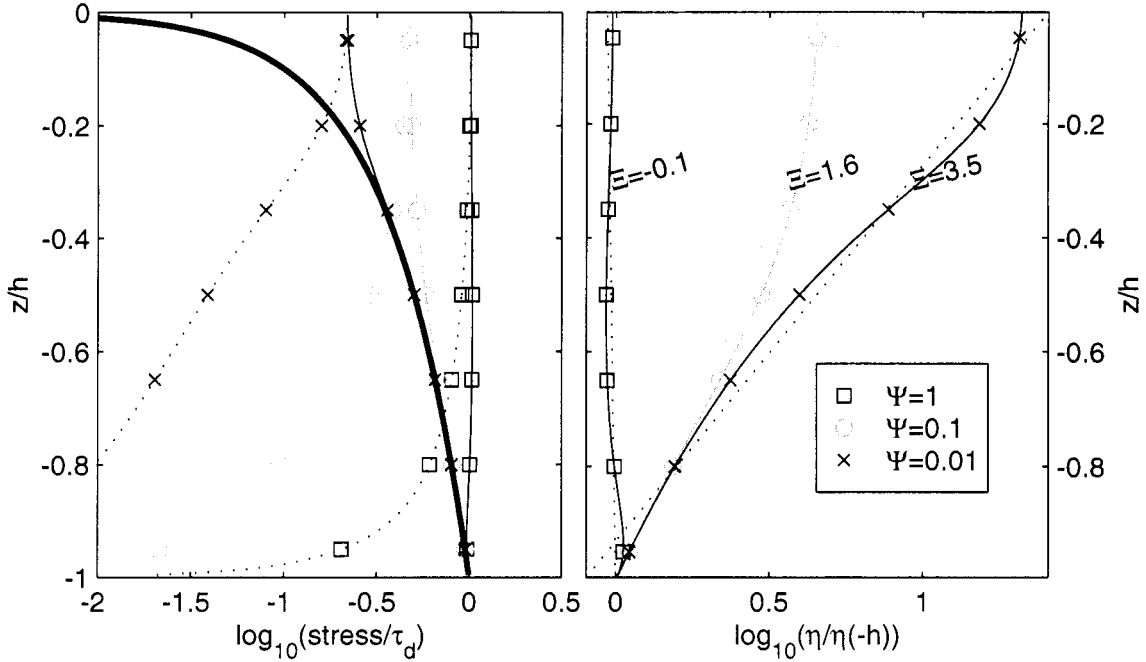
Figure 3.9: Stress component and viscosity variations for $T_s = T_b$, for three values of Ξ. At left, the x-scale gives the log stress components normalized by τ_d. τ_{xz} is shown by the bold solid curve, s_{zz} is shown for three values of Ψ by dotted curves, and τ_{eff} is shown for each value of Ψ by a thin solid curve. At right, the effective viscosity variations are plotted, normalized to the viscosity at the bed. The dotted curves show the best-fitting exponential models.

surface and the bed. For $\Psi = 0.01$, the recovered Ξ is 3.5, significantly smaller than that for $s_{zz}{=}0$. For $\Psi = 0.1$, the viscosity variations near the surface are strongly suppressed, and $\Xi = 1.6$. For $\Psi = 1$, the viscosity of the ice is nearly constant with depth, and $\Xi = -0.1$.

For polar glaciers, s_{zz} reduces the effects of thermal stratification on ice viscosity. The increase in s_{zz} near the surface increases τ_{eff}, reducing the effective viscosity, which partially cancels the large viscosity due to the low temperatures. Figure 3.10 shows the stress components and the viscosity for three values of Ψ for $T_b - T_s = 25$ K. For each value of Ψ, the calculated values of Ξ are larger than those in figure 3.9 by about 0.7, rather than 2.6, as would be expected if longitudinal strain rates were not taken into account.

Figure 3.11 shows the dependance of Ξ on Ψ and on the temperature difference between
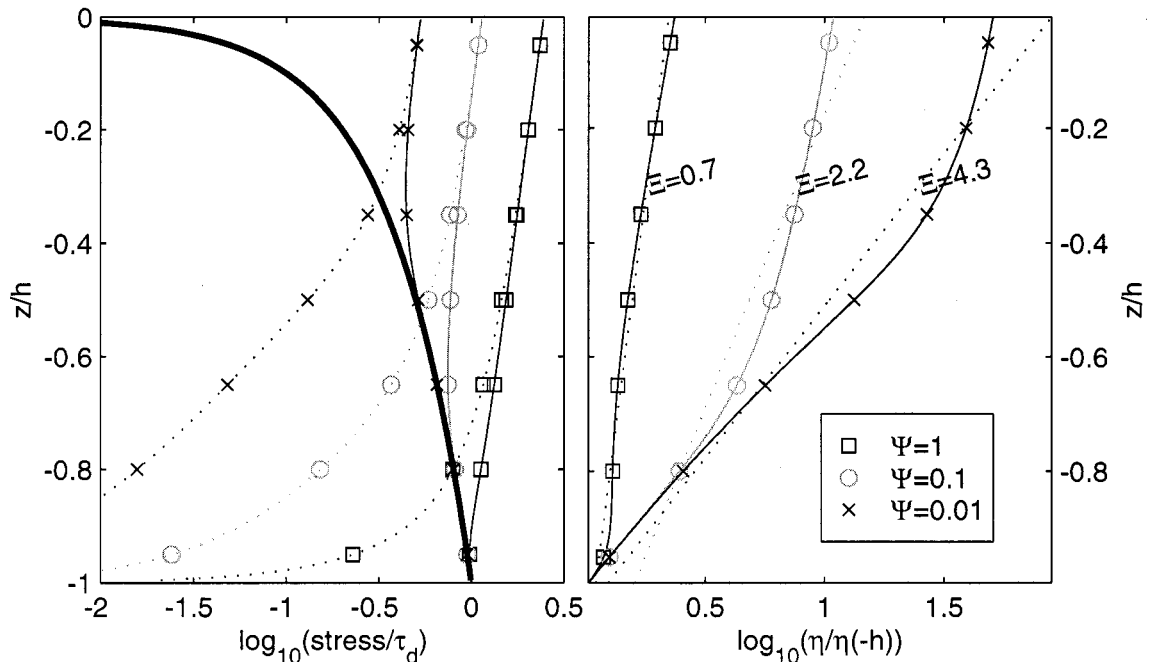
Figure 3.10: Stress component and viscosity variations for $T_b - T_b = 25$ k, for three values of Ξ. At left, the x-scale gives the log stress components normalized by τ_d. τ_{xz} is shown by the bold solid curve, s_{zz} is shown for three values of Ψ by dotted curves, and τ_{eff} is shown for each value of Ψ by a thin solid curve. At right, the effective viscosity variations are plotted, normalized to the viscosity at the bed. The dotted curves show the best-fitting exponential models.

the bed and surface. Ξ values range from 0 for $T_s = T_b$ and $\Psi = 1$, to 7.5, for $T_b - T_s = 60$ K and $\Psi = 10^{-3}$.

3.6.2 Estimated stratification parameters across Antarctica

Using equation 3.24, and the relation between Ψ, $T_b - T_s$ and Ξ shown in figure 3.11 we predict values of Ξ for Antarctica. We estimate the the ice thickness from the BEDMAP project (Lythe and others (2001)), the ice-surface slope from a digital elevation map of Antarctica, smoothed to wavelengths of 40 km (Smith (2005) chapter 2), and the accumulation rate from a compilation by Vaughan and others (1999). We estimate the surface temperature based on a lapse-rate of 10 K km^{-1} and a sea-level temperature of 253 K and assume that
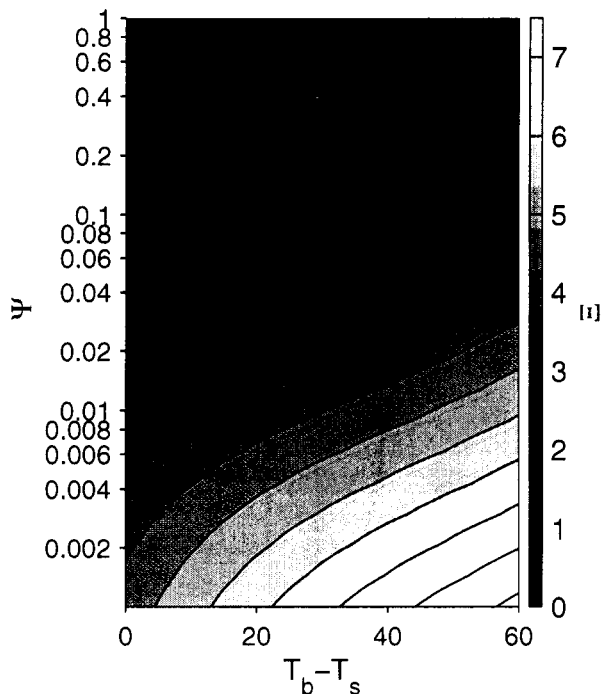
Figure 3.11: Ξ values as a function of Ψ and $T_b - T_s$.

$T_B = 273$ K. Figure 3.12 shows the calculated Ξ values. Ξ values are small at ice divides, where the surface slope is small, and in West Antarctica, where the accumulation rate is relatively large. Ξ is largest in the Amery Ice Shelf catchment, where the surface slope and ice thickness are relatively large, but the accumulation rate is small. The continental median Ξ is 5.1, with 68% of values falling between 3.5 and 6.0 and 95% of Ξ values are less than 6.5. These estimated Ξ values probably overestimate ice stratification, because in some places T_b <273 K, which stiffens the ice near the bed, and because horizontal gradients in ice velocity can contribute additional stress components to equation 3.11, which further softens the near-surface ice.

3.7 Discussion

Including the effects of stratified ice viscosity helps to resolve the difference between the modeled spectra and the measured spectra between $\lambda = 4 - 6h$ seen for $\Xi = 0$ (Smith
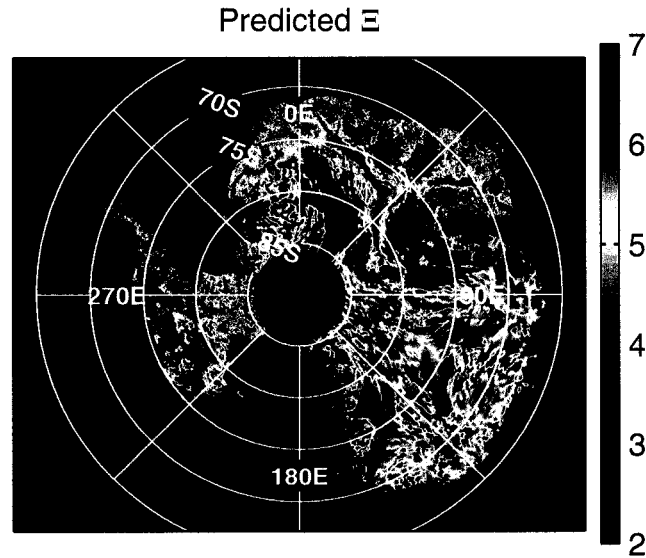
Figure 3.12: Predicted Ξ for Antarctica.

(2005) chapter 2, figures 2.2b and 2.9): Increased transfer around $\lambda = 6 - 8h$ means that the change in the slope of log-log plots of model spectra comes about at approximately $\lambda = 6h$ for moderate stratification, rather than at $\lambda = 3h$ for the unstratified case.

In section 3.6.1 we showed that the longitudinal strain-rate in ice partially counteracts the effect of vertical temperature variations on the ice viscosity. Taking longitudinal stretching, surface-parallel shear, and temperature variations into account, we predict values of Ξ for Antarctica between 4 and 7.

In section 3.5.4 we showed that while analysis of the measured surface spectra does not readily distinguish between models with different stratification parameters for $\Xi \leq 6$, it shows that models with $\Xi = 8$ are rarely compatible with measured surface statistics. Because the pattern of allowable Ξ-values is quite irregular across the continent, correlations between the acceptable Ξ values (figure 3.7 and the predicted Ξ values are not easily seen. However, the allowable Ξ values are generally less than 4 in West Antarctica, where the predicted Ξ values are also small, and the allowable values are large in the Amery Ice Shelf catchment, where predicted Ξ values are large.

The model misfits are generally insensitive to the choice of γ. This suggests that the

oversimplification inherent in the red-noise bed-statistics model is not detrimental to our ability to analyze surface statistics.

The model is also not very sensitive to ice stratification for $\Xi \leq 6$. 90% of spectra are not significantly different from the predicted spectra for $\Xi \leq 4$, and 45% of spectra are not significantly different from predicted spectra for $\Xi \leq 6$. Only for $\Xi = 8$ does the model reliably resolve a difference between measured and predicted spectra. This is in part true because there are not large differences among the transfer functions for $\Xi < 8$, but it also indicates that surface spectra compatible with $\Xi = 8$ are rare, as we predict from our analysis of viscosity profiles.

3.8 Conclusions

We have shown than an RBT model of ice-surface topography with $\Xi < 4$ describes ice-sheet surface spectra well for most of Antarctica. The $\Xi = 6$ and $\Xi = 8$ models do not often match surface statistics. This result is consistent with a model of ice-viscosity profiles that takes into account the stresses due to vertical compression of the ice column, but not with a model that only takes into account shear at the bed. Both models severely simplify the force-balance of the ice sheet, but our results demonstrate that the shear-only model is an oversimplification for analyzing the dynamic transfer of topography.

Because the $\Xi = 0$ model generally fits the surface spectra, realistic models of ice-sheet topography may be generated using a red-noise bed and the transfer functions given by Gudmundsson (2003). The large range of models that fit the data well is in part a symptom of the large scatter in red-noise spectral components. It is likely that if bed topography were known in detail, the uncertainty in our calculations could be reduced dramatically, and the range of acceptable Ξ values for each grid cell would be much smaller.

Chapter 4

ANISOTROPIC TEXTURE OF ICE SHEET SURFACES

4.1 Summary

In this paper, we analyze the magnitude and spatial organization of small-scale surface features, the surface texture, of the Greenland and Antarctic ice sheets. We measure properties of surface textures by analyzing digital elevation models. The texture is revealed in shaded relief maps, because surface slopes emphasize short-wavelength topography. We show that the surface slopes of ice sheets are both qualitatively and quantitatively different if the slope is calculated parallel to, rather than perpendicular to, the large-scale surface slope. The parallel slope variations are larger in magnitude than the perpendicular slope variations, and features in parallel slope maps are elongated perpendicular to the long-wavelength slope, while features in the perpendicular slope maps are elongated at a diagonal to the long-wavelength slope. These properties may be explained by a simple model of glacier dynamics in which a linearly-viscous slab of ice flows over a random, isotropic, red-noise bed. In this model, the surface anisotropy derives from the anisotropic transfer of bed topography to the surface.

4.2 Introduction

Although by normal standards polar ice sheet surfaces are very smooth and flat, they have roughness at all scales. The character of kilometer-scale undulations varies from place to place. Ice-divides are characteristically smooth, while inland areas with moderate surface slopes have a distinct scalloped texture. This scalloped texture gives way to more complicated textures in ice streams, where flow stripes and ice-margin features coexist with undulations across and parallel to flow.

The study of ice-sheet elevation variations has centered on the prediction of transfer

functions relating surface topography to bed topography on profiles. Nye (1959b) outlined the physics of the problem, and Budd (1970) was the first author to predict spectral transfer functions. Hutter and others (1981) improved on Budd's treatment of the stress perturbation to better predict transfer at long wavelengths. Reeh (1987) gave the first treatment of spectral transfer functions for a three-dimensional bed, while Jóhannesson (1992), Gudmundsson and others (1998) and Gudmundsson (2003) extended the theory to include the effects of sliding at the bed.

McIntyre (1986) compared the distributions of surface slopes on intersecting profiles, and found that at short spatial scales, the ice sheet surface is largely isotropic. Thorsteinsson and others (2003) found a good match between bed topography measured on a few profiles and bed topography recovered by inversion of two-dimensional transfer coefficients, but did not explicitly analyze the anisotropy of the ice-sheet surface.

In one of the first discussions of anisotropic surface textures measured by satellite altimetry, Remy and others (1999) found networks in the large-scale (50-500 km) features of ice-sheet topography that are anisotropic relative to the ice-flow direction, with 100 km-scale features running parallel to the ice-flow direction. They explain these large-scale features in terms of the development of drainage networks moving ice from the interior to the coast, showing that the surface curvature at outlet glaciers can be transmitted upstream, branching into an arborescent pattern along the way. They showed that the remainder of the surface topography, at scales too small to be explained by the curvature of the outlet glaciers, shows ridges with wavelengths of about 20 km, organized so that they run at about 45° to the ice-flow direction. The cause and orientation of these diagonal features remains unexplained.

In this paper we show that the Greenland and Antarctic ice sheets have significantly anisotropic surface topography by calculating along-flow and across-flow surface slope variations. We show that these local undulations are between 10% and 50% of the large-scale surface slope, and that undulations measured parallel to the ice-flow direction are 10-20% larger than those measured perpendicular to the ice-flow direction. We also find that surface slopes calculated along and across the ice flow direction have a distinctive appearance: Slopes measured along flow are organized into ripples that cut perpendicularly across the

flow direction, while slopes measured across the flow are organized into ripples at a diagonal to the flow direction. We show that these anisotropic features can result from the transfer of an isotropic bed mediated by ice flow dynamics.

4.3 Data

Our analysis is based on Digital Elevation Models (DEMs) of Greenland and Antarctica, developed by Scambos and Haran (2001), and Bamber and Bindschadler (1997), respectively. Both DEMs are based on ERS-1 radar altimetry, which can accurately measure the large-scale features of ice sheets, but tends to underestimate the amplitude of surface features smaller than the $\approx$10-km width of the radar beam. Both DEMs were constructed using slope-correction factors that partially ameliorate this problem. Bamber and Dans (2005) compared the DEM by Bamber and Bindschadler (1997) to ICESat elevation measurements, and found that the DEM captures undulations with wavelengths greater than 15-20 km, if at moderately reduced amplitudes.

Scambos and Haran (2001) improved the resolution of their Greenland DEM further using a shape-from-shading scheme. They used photoclinometry based on slope-related brightness variations in AVHRR visual images of kilometer resolution with a data-assimilation scheme that let them combine multiple images at different solar illumination angles. They combined this map of the fine-scale undulations with a radar altimetry map that captured the coarse-scale shape of the ice sheet. The final model has a horizonal resolution of about 1 km, with a vertical accuracy on the order of 0.5-4 m over most of the continent. The DEM is most accurate in undulating landscapes, where brightness variations due to topography are much larger than brightness variations due to instrumental noise or to surface reflectivity variations. The most significant errors are near ice-divides, where the ice surface is extremely flat.

4.4 Surface slopes and slope texture

Ice sheet surface slopes give a measure of the size and character of surface undulations in a way that is straightforward to describe and to calculate. Calculating the slope of a surface

enhances short-wavelength features that are not necessarily visible in contour maps, without the need to explicitly describe a "long wavelength" scale and a "short wavelength" scale, although it will prove convenient to make such a distinction later on.

Comparing slope variations in different directions can show whether a surface is isotropic or not. For an isotropic surface, the characteristics of the surface should be independent of direction. We may measure anisotropy by calculating directional statistics, such as the variability in surface slopes, or by looking for apparent directional features in maps of elevations or slopes. In either case, we seek to describe the *texture* of the ice sheet surface, a term we use to refer to the spatial organization of local surface topography variations. We demonstrate in this section that both the magnitude of and the appearance of short scale slope variations are anisotropic, with characteristics that depend on the direction in which we measure the slope relative to the ice flow direction.

Because the ice flow direction generally follows the down-slope direction averaged at 20-40 ice thicknesses (Bamber and others (2000)), we assume that the orientation of the surface slope calculated from a smoothed DEM is the same as the flow direction. We smooth the DEM at a scale of 40 km, which is comparable to or larger than 20 times the ice thickness for most parts of Greenland and Antarctica. This introduces a somewhat arbitrary distinction between short-scale slope variations and long-scale slope variations. However, the scale we choose does not have a large influence on our results, because for small regions of the ice sheet, most variations in slope are at a horizontal scale much smaller than the smoothing length.

4.4.1 Calculating surface slopes

We estimate the surface-slope vector, ∇z, from gridded ice elevations using a centered difference scheme:

$$\nabla z(x,y) = \frac{z(x+\delta,y) - z(x-\delta,y)}{2\delta}\hat{\mathbf{x}} + \frac{z(x,y+\delta) - z(x,y-\delta)}{2\delta}\hat{\mathbf{y}} \qquad (4.1)$$

Here $\hat{\mathbf{x}}$ and $\hat{\mathbf{y}}$ are the unit grid vectors, and δ is the grid spacing. For the Greenland DEM, $\delta = 0.62$ km, while for the Antarctic DEM, $\delta = 5$ km. Because both Scambos and Haran (2001) and Bamber and Bindschadler (1997) filtered the DEM values to make the

DEM surfaces smooth at the single-pixel level, equation 4.1 accurately estimates the slope of the DEM surface. However, since the DEM surfaces represent a smoothed version of the true Antarctic and Greenland surfaces, some details of the surface will not be recovered, particularly for Antarctica.

We treat the surface slope as made up of a long-wavelength component $\mathbf{S}_L$, defined by the overall shape of the ice-sheet, and a short-wavelength component, $\mathbf{S}_s$, defined by local surface undulations. The sum of these two is equal to ∇z:

$$\nabla z = \mathbf{S}_L + \mathbf{S}_s \tag{4.2}$$

We estimate $\mathbf{S}_L$ by calculating a smoothed version of the ice-sheet topography by convolving z with a Gaussian kernel that has standard deviation of 40 km, then taking the gradient of the smoothed surface.

Defining $\mathbf{T}$ as the vector perpendicular to $\mathbf{S}_L$ with the same magnitude as $\mathbf{S}_L$, we can define the components of the slope variations parallel to and perpendicular to the flow-direction, normalized to the long-wavelength slope,

$$[S_\parallel, S_\perp] = \left[\frac{\mathbf{S}_L \cdot \nabla z}{\mathbf{S}_L \cdot \mathbf{S}_L} - 1, \frac{\mathbf{T} \cdot \nabla z}{\mathbf{S}_L \cdot \mathbf{S}_L} \right]. \tag{4.3}$$

Combining this with equation 4.2, we find:

$$[S_\parallel, S_\perp] = \left[\frac{\mathbf{S}_L \cdot \mathbf{S}_L + \mathbf{S}_L \cdot \mathbf{S}_s}{\mathbf{S}_L \cdot \mathbf{S}_L} - 1, \frac{\mathbf{T} \cdot \mathbf{S}_L + \mathbf{T} \cdot \mathbf{S}_s}{\mathbf{S}_L \cdot \mathbf{S}_L} \right], \tag{4.4}$$

which simplifies to

$$[S_\parallel, S_\perp] = \left[\frac{\mathbf{S}_L \cdot \mathbf{S}_s}{\mathbf{S}_L \cdot \mathbf{S}_L}, \frac{\mathbf{T} \cdot \mathbf{S}_s}{\mathbf{S}_L \cdot \mathbf{S}_L} \right]. \tag{4.5}$$

By construction, $\mathbf{S}_s$ should have a mean of zero in each direction, so $S_\parallel$ and $S_\perp$ will each have a mean of zero. The size of variations in each component of $[S_\parallel, S_\perp]$ depends on the magnitude of $\mathbf{S}_s$ relative to $\mathbf{S}_L$ and its degree of anisotropy.

We may form a non-dimensional estimate of the surface roughness over local areas by calculating $R_\parallel$ and $R_\perp$, the RMS deviations in $S_\parallel$ and $S_\perp$ around 0, calculated over areas 50 km on a side. To measure the degree of anisotropy, we define the anisotropy ratio:

$$\Omega = \frac{R_\parallel - R_\perp}{R_\parallel + R_\perp}. \tag{4.6}$$

Ω compares the roughness in the flow-parallel direction to the roughness in the flow-perpendicular direction. For isotropic surfaces, $\Omega=0$; Ω tends towards 1 for $R_\parallel \gg R_\perp$, and tends towards -1 for $R_\parallel \ll R_\perp$.

4.4.2 Slope texture in Greenland

Figure 4.1 shows $R_\parallel$ and $R_\perp$ across Greenland. The spatial distributions of $R_\parallel$ and $R_\perp$ are similar: Both are modestly larger in the southern part of Greenland than in the north, and have unusually large values around the Northeast Greenland Ice Stream (NEGLIS). Figure 4.2 shows the frequency distributions of $R_\parallel$ and $R_\perp$, and the anisotropy ratio, Ω. In most parts of Greenland, $R_\parallel$ and $R_\perp$ are between 0.1 and 0.6, indicating that short-scale slopes are between 10% and 60% of the overall surface slope. The median anisotropy ratio, Ω, is 0.07, showing that the slope variations parallel to the flow direction are moderately larger than those across the flow direction.

Although the differences between $R_\parallel$ and $R_\perp$ are small, $S_\parallel$ and $S_\perp$ have a distinctly different organization in small local regions. Figure 4.3 shows the perpendicular and parallel slope components in the NEGLIS catchment. Both maps are dominated by small-scale features with minimum wavelengths of around 10 km. The map of $S_\perp$, shows features elongated at about 45° to the ice-flow direction, and a prominent trench that follows the margins of NEGLIS. By contrast, the map of $S_\parallel$ shows strong features oriented across the flow direction, with no sign of a trench at the margin.

4.4.3 Slope texture in Antarctica

Figure 4.4 shows the spatial distributions of $R_\parallel$ and $R_\perp$ for Antarctica. Both R values are largest at the flow divides, and are somewhat larger in West Antarctica than in East Antarctica. In most parts of the ice sheet, $R_\parallel$ is somewhat larger than $R_\perp$, particularly near the West Antarctic flow divide, and in Victoria Land near the Transantarctic mountains. Figure 4.5 shows the distributions of $R_\parallel$ and $R_\perp$, and the ratio between the two. R values are somewhat smaller than those in Greenland, typically between 0.05 and 0.55. The median anisotropy ratio, Ω, is 0.11, indicating that there is somewhat more anisotropy in
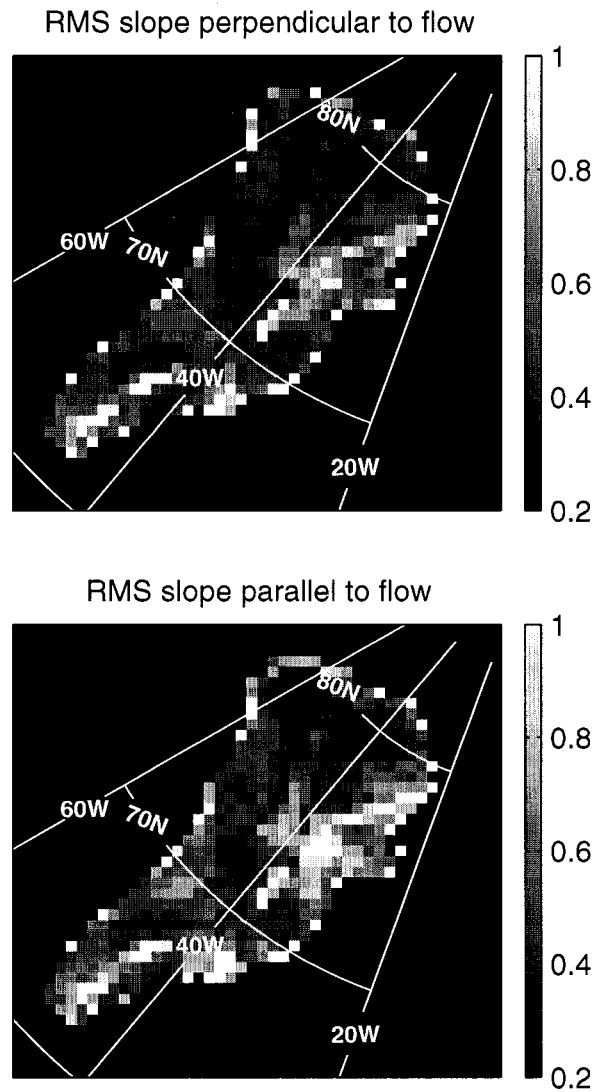
Figure 4.1: Perpendicular and parallel slope roughness for Greenland. Top: map of $R_\perp$. Bottom: Spatial variations in $R_\parallel$.

the Antarctic DEM than in the Greenland DEM.

The patterns in $S_\parallel$ and $S_\perp$ are consistent with those in Greenland: $S_\parallel$ is organized in features oriented perpendicular to flow, while $S_\perp$ is organized in patterns diagonal to the flow direction. A good example of these patterns is found in the topography of ridge B, in Wilkes Land (figure 4.6) where ice flows radially outwards from the northern end of
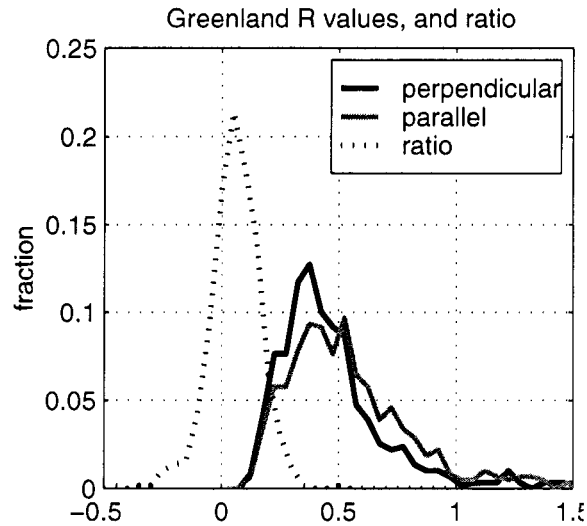
Figure 4.2: Distributions of $R_\perp$ (red), $R_\parallel$ (blue), and the ratio Ω for Greenland.

ridge B, and the features in the parallel and perpendicular slope maps vary continuously in orientation, yet maintain their respective perpendicular and diagonal orientation to ice flow.

4.5   The role of ice-flow dynamics in surface texture

The ice sheet texture in both Antarctica and Greenland is both qualitatively and quantitatively anisotropic. The relationship between texture perpendicular to and parallel to ice flow is fairly consistent from one ice sheet to another. That the anisotropy depends on the ice-flow direction suggests that it is a property of ice-flow, not a property somehow inherited from the bed. Although we have no reason to think that bed topography should be isotropic, it would be surprising to find that the anisotropy of the bed had a consistent orientation to the flow-direction, except perhaps at short scales where glacial erosion is an important factor.

We investigate the influence of ice flow on surface texture using a Red Bed Transfer (RBT) model. In this model, ice surface topography results from ice flow over a rough bed. The bed is isotropic red noise, whose Fourier spectrum as a function of wavenumber $\mathbf{k}$ is
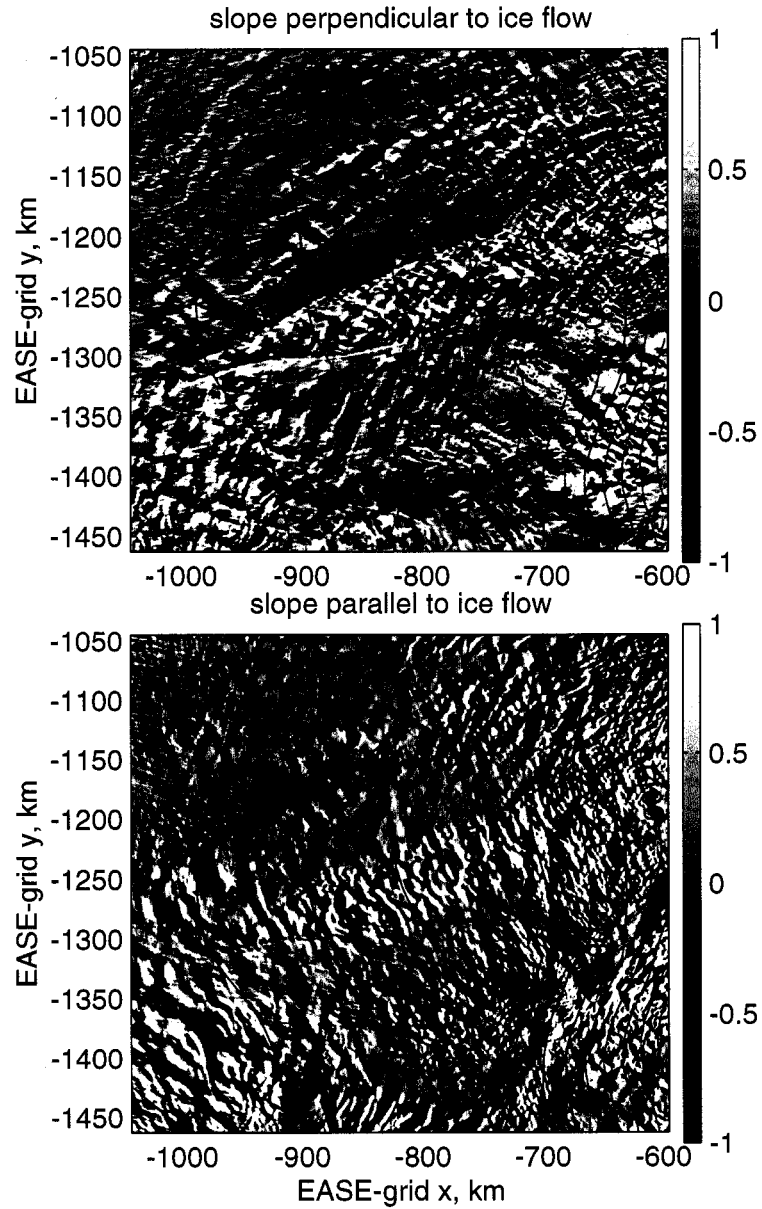
Figure 4.3: Normalized surface slopes taken perpendicular and parallel to the ice-slope direction in Northeast Greenland. The feature with strong surface undulations running from upper right to lower left in the image is the Northeast Greenland Ice Sheet. The very fine undulations in the upper left corner are a result of noise in the DEM in an area with a small large-scale slope.

RMS slope perpendicular to flow

RMS slope parallel to flow
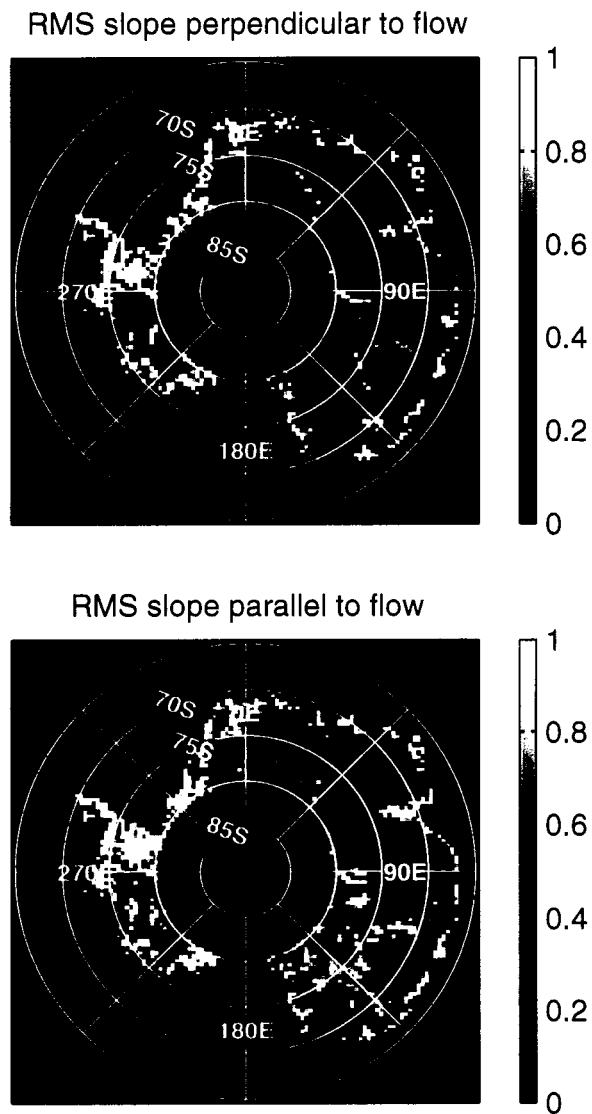
Figure 4.4: Perpendicular and parallel slope roughness for Antarctica. Top: Spatial variations in $R_\perp$. Bottom: Spatial variations in $R_\parallel$.

described by a power-law:

$$Z_b(\mathbf{k}) \propto |\mathbf{k}|^\gamma. \tag{4.7}$$

Here γ is between -1.5 and -1, so that long-wavelength components dominate the bed spectrum. This type of spectrum is typical of land surfaces (Turcotte (1992)).
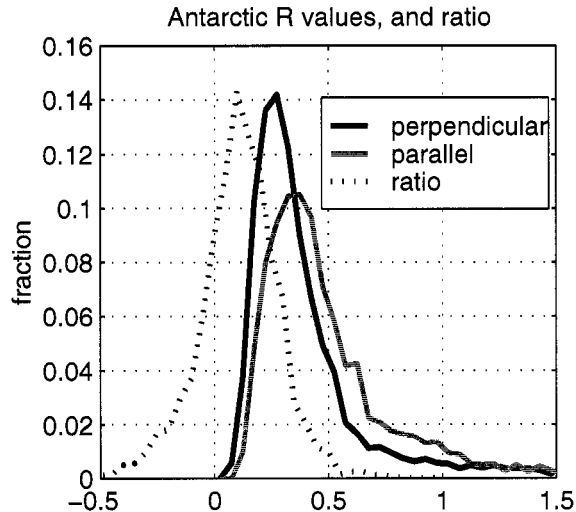
Figure 4.5: Distributions of $R_\perp$ (red), $R_\parallel$ (blue), and the ratio Ω in Antarctica north of $81°$.

The ice flow is modeled using a formulation developed by Gudmundsson (2003), where the ice sheet is approximated by a parallel-sided slab of Newtonian viscous material flowing over the bed. Perturbations in the flow due to bed topography produce small perturbations in the surface topography. The relationship between the bed topography and the surface topography is given by transfer coefficients scaling the two-dimensional Fourier transform of the surface to that of the bed:

$$Z_s(\mathbf{k}) = T_{zz}(\mathbf{k}, \alpha, C) Z_b(\mathbf{k}). \tag{4.8}$$

T_{zz} is expressed as a function of the nondimensional wavenumber, $\mathbf{k}$, which is equal to the wavenumber times the ice thickness, h. The form and magnitude of $T_{zz}(\mathbf{k})$ depends on the long-wavelength surface slope, α, and the sliding ratio C (the ratio between the rate of sliding at the bed and the rate of deformation between the surface and the bed). Although Gudmundsson's derivation of T_{zz} is based on a perturbation analysis that assumes that bed topography is small, and leaves out the effects of non-linear ice viscosity, Raymond and Gudmundsson (2005) found that surfaces calculated for more realistic ice viscosity match the transfer theory well, for bed perturbations up to 25% of the ice thickness.

The Fourier spectra and transfer functions may be expressed as a function of the two-
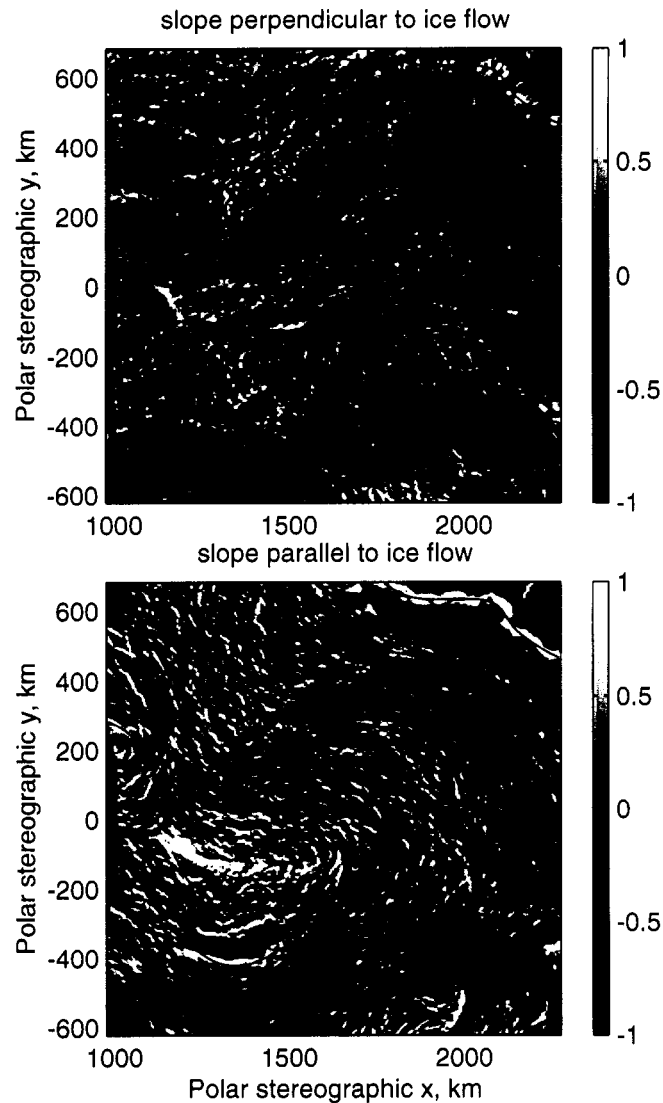
Figure 4.6: Surface texture on Ridge B, Wilkes Land, Antarctica. Top: Slope calculated perpendicular to the ice-flow direction. Bottom: Slope calculated parallel to the slope direction.

dimensional wavenumber, or, equivalently, as a function of the normal azimuth, θ, of the components and the minimum wavelength, λ (measured from crest to crest of the Fourier component along the normal azimuth). The normal azimuth is the direction perpendicular to the ridge crests, relative to the ice-flow direction; a component with a normal azimuth

of 0° appears as ridges elongated perpendicular to ice flow. The two sets of coordinates are related by the transformation:

$$[\theta, \lambda] = \left[tan^{-1}\left(\frac{\mathbf{k}\cdot\hat{y}}{\mathbf{k}\cdot\hat{x}}\right), \frac{2\pi h}{\|\mathbf{k}\|}\right],\tag{4.9}$$

where $\hat{x}$ is the along-flow unit vector and $\hat{y}$ is the across-flow unit vector.

Because the bed in our RBT theory is isotropic, anisotropy in the surface can only come from anisotropy in the transfer functions. The transfer functions (Gudmundsson (2003)) for slow-sliding and fast-sliding ice are shown in figure 4.7. The slow-sliding transfer function is highly anisotropic, with bed undulations elongated perpendicular to the ice-flow direction transferred preferentially to the surface. By contrast, the fast-sliding transfer is nearly isotropic, although bed components striking exactly perpendicular to flow are not transferred to the surface.

We show the pattern of anisotropy in T_{zz} for different values of λ by plotting $T_{zz}(\theta, \lambda)$ / $T_{zz}(0, \lambda)$ against θ (figure 4.8). Regardless of the sliding ratio, in the long-wavelength limit the transfer amplitude follows

$$|T_{zz}(\theta, \lambda)| \approx |T_{zz}(0, \lambda)||cos(\theta)|.\tag{4.10}$$

This means that at long wavelength, the surface is made up of ridges elongated perpendicular to ice flow. In the short-wavelength limit, the transfer becomes nearly isotropic, with nearly constant transfer for $|cos(\theta)| > 0$, falling sharply to zero as $|cos(\theta)| \to 0$. If the sliding rate is small, the transfer is strongly anisotropic for wavelengths as small as $\lambda = h/4$, but as sliding increases, the transition between short- and long-wavelength behavior moves to longer wavelengths, until for $C = 10^4$ the transfer is nearly isotropic for wavelengths as large as 10 h. This means that slow-sliding surfaces are highly anisotropic, and fast-sliding surfaces are nearly isotropic.

4.5.1 Features of model surfaces

For an isotropic bed, anisotropy in the surface arises from anisotropy in the transfer functions. This means that for slow sliding and long wavelengths,

$$|S(\theta, \lambda)| \approx |S(0, \lambda)||cos(\theta)|.\tag{4.11}$$
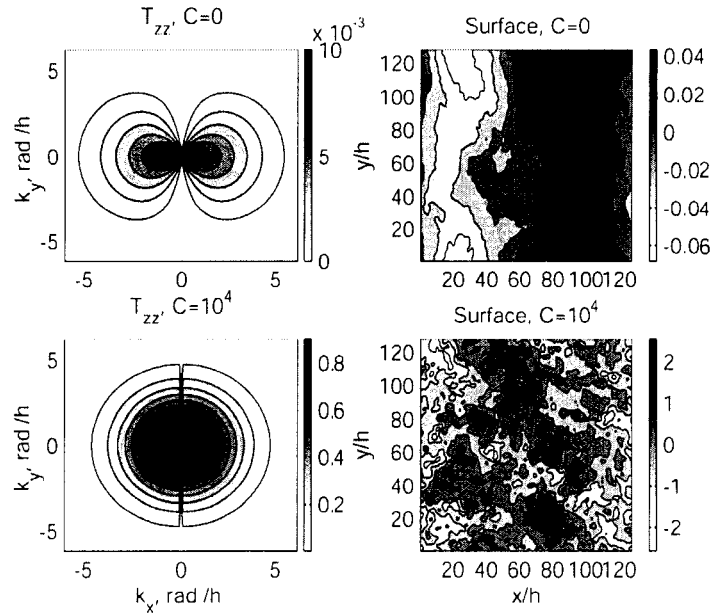
Figure 4.7: Transfer functions (left column) and predicted surfaces (right column) for no sliding (top row) and for fast sliding (bottom row). Both surfaces are based on the same red-noise bed topography, with unit amplitude at $\lambda = 2\pi h$ and $\gamma = -1.25$. The ice-flow direction is from left to right.

while for fast sliding and short wavelengths, $S(\theta, \lambda) \approx S(0, \lambda)$. The $\cos \theta$ dependance means that ridges running across the flow are enhanced relative to ridges running parallel to flow. Figure 4.7 shows surfaces predicted for no sliding and for fast sliding for the same random bed; the non-sliding surface has a dominant ridge running across flow while the fast-sliding surface has no clear feature orientation.

This analysis appears at first to run counter to the claim by Gudmundsson and others (1998) that flow-stripes result from the transfer of bed roughness to the surface in fast-sliding ice. Their claim is based on the impulse-response of the transfer functions: A short-wavelength hill on the bed results in a bump at the surface, with a long shallow trench extending downstream from it. However, RBT surfaces do not show flow-stripes at any sliding rate because the bed is covered everywhere with small hills, and the trench developed by any one hill on the bed is overprinted by the bumps developed by other hills downstream. The preservation of flow stripes requires a very smooth bed, so that the
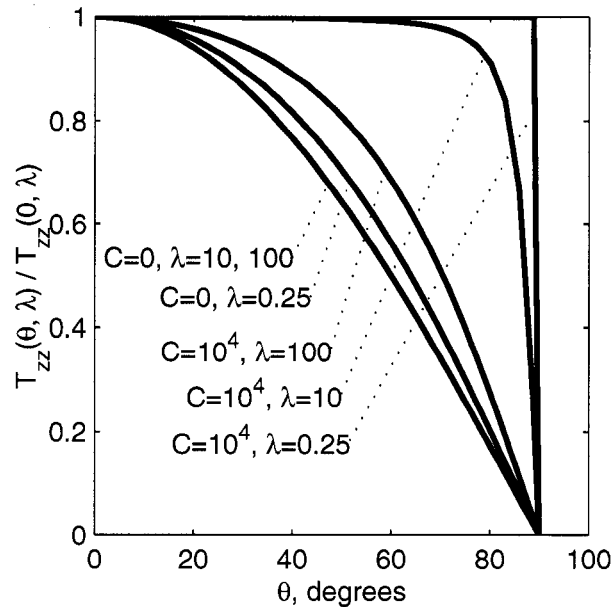
Figure 4.8: The anisotropy of transfer functions for different wavelengths and sliding ratios. $T_{zz}(\theta,\lambda)/T_{zz}(0,lambda)$ is plotted against θ for C=0 and C=10^4, for $\lambda = 0.25h$, $\lambda = 10h$, and $\lambda = 100h$.

trenches are not overprinted by downstream roughness. The implication is that flow stripes may be generated by the bed in a rough area on an ice stream and extend into smoother areas, or they may come about where the ice stream rides on smooth sediments where a few rises protrude through the sediments.

4.5.2 The anisotropy of model surface slopes

We can predict the patterns of anisotropy in the surface slopes of RBT surfaces directly from their predicted Fourier spectra. If a surface has Fourier transform $S(\mathbf{k})$, the transform of its slope along direction $\hat{k}_o$ is

$$S'(\mathbf{k}) = -iS(\mathbf{k})\mathbf{k} \cdot \hat{k}_o. \tag{4.12}$$

The slope spectrum is enhanced relative to the elevation spectrum at short wavelengths for components with elongated perpendicularly to unit vector $\hat{k}_o$. This lets us predict the sorts of variations seen in $S_\perp$ and $S_\parallel$ above. Where equation 4.10 holds, spectra for slopes taken

perpendicular to the flow-direction will be of the form

$$|S'(\lambda, \theta)| = |S(\lambda, 0)|\frac{2\pi h}{\lambda}|sin(\theta)cos(\theta)| \tag{4.13}$$

because $\mathbf{k} \cdot \hat{k_o} = sin(\theta)2\pi h/\lambda$. This spectrum has maxima for $\theta = 45°$, $135°$, $225°$, and $315°$, so the slope appears to have strong features striking at $\pm 45°$ to the flow direction.

By contrast, spectra for slopes taken parallel to the flow-direction will have the form

$$|S'(\lambda, \theta)| = |S(\lambda, 0)|\frac{2\pi h}{\lambda}cos^2(\theta) \tag{4.14}$$

which has maxima at zero and 180∘ to the slope direction, giving strong features only for components with normal azimuths parallel to the slope direction. Short-wavelength features follow this pattern only at slow sliding rates; for faster sliding, the short-wavelength features become isotropic, and the strongest features seen in the slope will be those running across the slope direction, regardless of the orientation of the slope direction relative to the flow direction.

Figure 4.9 shows simulated shaded-relief maps for two ice-sheet surfaces derived from the same red-noise bed, illuminated perpendicular to and parallel to the flow direction. The non-sliding surface has dominant features running across flow when illuminated from a direction parallel to ice flow, and dominant features running at a diagonal to ice flow when illuminated from a direction perpendicular to flow. Features in the fast-sliding surface have smaller wavelengths than those in the non-sliding surface because transfer is stronger at short wavelength. The orientation of these features is less obvious than of those in the non-sliding surface, but under both illumination angles, the dominant feature orientation is perpendicular to the illumination direction.

The expected magnitudes of $R_{\parallel}$ and $R_{\perp}$ depend on the bed amplitude and the rate of sliding, but not on the long-wavelength surface slope magnitude, α. This is because T_{zz} is linearly proportional to α, so because equation 4.3 has a measure of amplitude in the numerator and a measure of α in the denominator, S and thus R should be independent of the long-wavelength surface slope. The dependance of R on the rate of sliding is shown in figure 4.10. For $C = 10^4$, R is about 100 times larger than for $C = 0$.
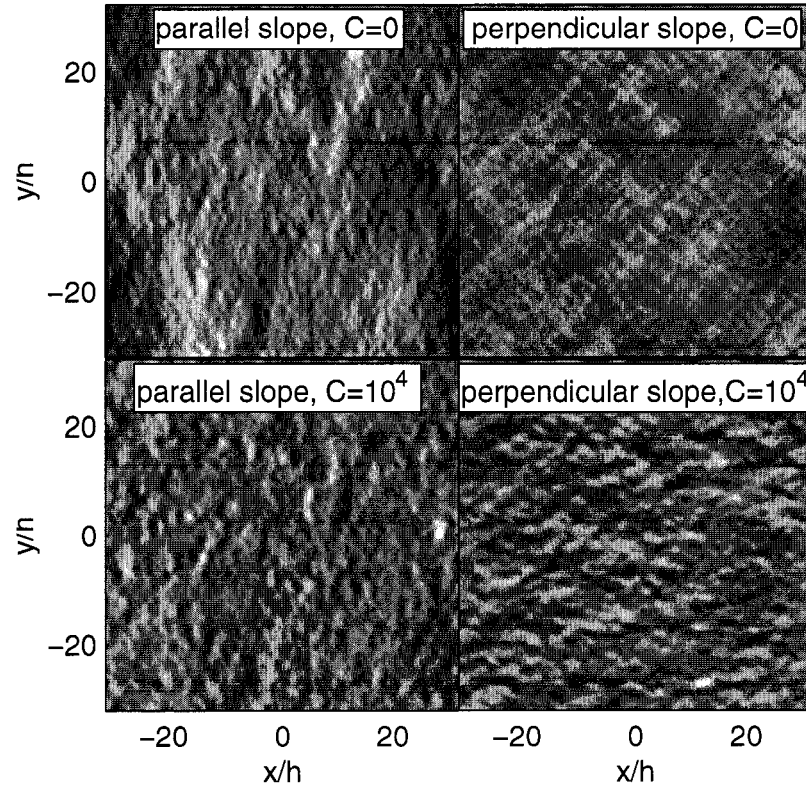
Figure 4.9: Shaded relief ice-sheet surfaces, illuminated from different directions. Ice flow is from left to right. The surface shown in plots at top has no sliding (C=0), the surface shown in plots at bottom has fast sliding (C=10^4). The plots in the left column are illuminated from the left, parallel to ice flow, the plots in the right column are illuminated from the bottom of the page, perpendicular to the ice-flow direction.

The expected value of the anisotropy ratio Ω, depends on the sliding rate. For slow-sliding surfaces such as that in figure 4.9, the expected median value of Ω is 0.22, while for fast sliding surfaces ($C \approx 10^4$), the expected median Ω is 0.06.

4.6 Discussion

The RBT model suggests that the variations we measure in R reflect a combination of bed roughness and sliding variations. If we assume that over most of Greenland and Antarctica, the variations in sliding are too small to be the dominant control on surface roughness, then the relatively small variations in R we observe suggest that bed roughness varies by less
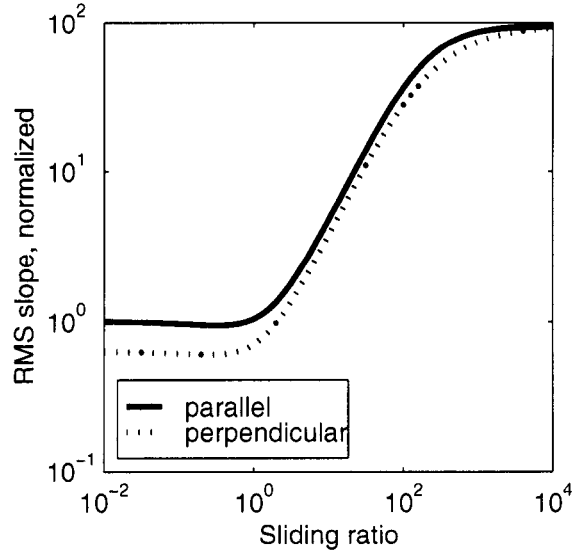
Figure 4.10: $R_\perp$ and $R_\parallel$ as a function of the sliding ratio. Both are normalized to the non-sliding value of $R_\parallel$ at C=0.

than an order of magnitude over most of Antarctica and Greenland.

In the NEGLIS region we can combine information about R with surface-texture patterns to make a qualitative rate of sliding at the bed. NEGLIS shows strong surface texture that is visibly anisotropic. The strength of the surface texture suggests that there is either fast sliding or large roughness at the bed. A compilation of bed elevation data by Bamber and others (2003) shows that the bed roughness beneath NEGLIS is similar to that just to the south of the ice stream, where the surface texture is much weaker. This implies that the strength of the texture results from sliding at the bed. However, the surface anisotropy suggests that very fast sliding ($C > 1000$) cannot be the dominant mechanism of ice-flow, because the surface for fast-sliding ice should be close to isotropic. We can thus conclude that the sliding rate under NEGLIS is between $C \approx 1$ and $C \approx 100$. This assessment agrees with modelling by Joughin and others (2001), who found that the basal drag under the upper part of NEGLIS is between 50% and 80% of the driving stress, implying that there is either sliding at the bed or a layer of weak ice close to the bed. The strong trenches at the margin of the ice stream have no clear explanation in the RBT model; we suggest that

they are a result of mechanisms within the ice sheet margin that are not a part of transfer theory.

The slow-sliding value of Ω predicted by RBT is larger (more anisotropic) than the values we measured in Antarctica, and considerably larger than those we measured in Greenland. The difference between the RBT anisotropy and that measured in Antarctica and Greenland may in part be a result of noise in the data: Adding as little as 0.5% isotropic random noise to the simulated $C = 0$ surface results in Ω values of 0.1, comparable to the calculated anisotropy in Antarctica, while adding 1% random noise results in values of 0.08, comparable to the calculated anisotropy in Greenland. These noise levels do not strongly alter appearance of the surfaces, so the relationship describing the surface texture remains.

4.7   Conclusions

Our calculations show that local surface topography on ice sheets is of significant magnitude compared to the large-scale topography of the ice sheet, with local slopes on the order of 10-50% of the large scale surface slope. We show that the texture of ice sheet surfaces follows distinct patterns: The RMS variations in the surface slope are larger in the along-slope direction than in the across-slope direction, and that slope variations in the along-flow direction and the across-flow direction are organized into across-flow and diagonal features, respectively.

These results are explained well by the RBT model, which shows that anisotropic properties of ice flow produce anisotropic surfaces that have similar properties to those we measure. This model lets us make educated guesses about the rate of sliding at the bed in regions where we have information about bed topography.

Although our analysis does not predict the short-wavelength features described by Remy and others (2001) as running at 45° to the ice-flow direction, we suspect that these features are analogous to the diagonal features that the RBT model predicts for cross-slope illumination of slow-sliding surfaces. The conclusion of McIntyre (1986), that fine-scale ice sheet slopes are not different in the across-slope and along-slope direction, are not borne out by this study, and may be attributed to McIntyre's small sample of topographic profiles.

Our results suggest that care should be taken in interpreting shaded relief maps of ice sheet surfaces, because features with distinct orientations may appear solely due to the direction of lighting relative to the ice-flow direction. Our technique for calculating the surface slope parallel to the ice flow direction allows the construction of shaded relief maps whose texture properties should be the same everywhere, regardless of the ice-flow direction. Maps constructed in this way should be more useful for the investigation of bedrock topography than maps with a shading direction of arbitrary orientation to the flow direction.

Chapter 5

RECENT ELEVATION CHANGES ON THE ICE STREAMS AND RIDGES OF THE ROSS EMBAYMENT FROM ICESAT CROSSOVERS

This paper has been submitted to Geophysical Research Letters under the same title, with co-authors Charles R. Bentley and Charles F. Raymond.

5.1 Summary

We analyze differences in ICESat elevation estimates at orbital crossover locations to determine short-term rates of elevation change for small regions within the Ross Embayment of the West Antarctic Ice sheet. A linear regression of crossover elevation difference against time difference gives an estimate of the mean elevation-change rate during the ICESat mission to date. We observe prevalent elevation change in the south, with uplift in the upstream end of Kamb Ice Stream at 0.24-0.30 m a^{-1}, and thinning in the parts of Whillans Ice Stream, Mercer Ice Stream, and the adjacent Conway and Engelhardt ice ridges at 0.05-0.18 m a^{-1}. These rates of elevation change are too large to be explained by the 0.02 -0.03 m a^{-1} formal regression error, by seasonal height variations, or by accumulation- or densification-rate variability, suggesting that they reflect real variations stemming from ice dynamics of the region.

5.2 Introduction

NASA's Ice, Cloud and land Elevation Satellite (ICESat) mission carries Earth's first polar-orbiting satellite laser altimeter Geoscience Laser Altimeter System (GLAS). The 86S orbit extent provides first-time altimetric coverage of the southern parts of the Ross Ice Shelf. By mid 2005, ICESat had collected ice-surface-elevation data over a period of just more than

24 months, allowing resolution of cm-per-year elevation changes (Schutz and others (2005)).

Recent studies of the ice dynamics of the Ross Embayment (RE), near the southern limit of ICESat coverage between 75°S and 86°S, show large rates of change in ice velocities and local mass balance over decadal and shorter time scales. A general review of WAIS elevation changes has been given by Alley and Bindschadler (2001). GPS-based point measurements coupled with airborne laser altimetry surveys show rapid thickening in the upper trunk of KIS (Kamb Ice Stream, further abbreviations defined in table 2), rapid thinning in the upper trunk of WIS, and near balance in the catchment region of WIS (Spikes and others (2003)). This is consistent with velocity changes recently observed in the ice streams: The stagnation of KIS produced a net thickening in the region where flow from the still-active tributaries flows into the stagnant trunk region (Price and others (2001)). Likewise, the downstream region of WIS has slowed faster than the upstream region, which could lead to thickening of the middle of the ice stream (Joughin and others (2002)), although WIS as a whole is largely in balance (Joughin and Tulaczyk (2002)). The spatial pattern of long-term relative elevation change across the RE was estimated from the shapes of internal layers in the inter-stream ridges, detected by ice penetrating radar. These show a gradient in thinning from south to north, with WIS thinning faster than BIS (Nereson and Raymond (2001)). In this paper we use ICESat data to determine elevation changes in the RE. Although these elevation differences reflect time-varying snow deposition and densification as well as ice dynamics, we show that they now are adequate to demonstrate that the largest predicted changes are ongoing, and to suggest that rapid change is occurring in regions not covered by previous satellite altimeters.

5.3 Methods

We recover rates of elevation change from analysis of elevation estimates at orbital crossover locations. We select a subset of the approximately 110,000 crossovers in the RE that we believe to have the smallest contamination by errors, and divide these into geographical regions to obtain the spatial distribution of elevation-rate estimates. We then solve for the mean rate of elevation change during the observation period by linear regression by including

Table 5.1: GLA01 and GLA12 versions and dates for laser operations periods.

Ops period	GLA01	GLA12	dates
1	13	18	2/20/03-3/20/03
2a	19	21	9/25/03-11/18/03
2b	16	16	2/17/04-3/21/04
2c	17	17	5/18/04-6/21/04
3a	18	18	10/3/04-11/8/04
3b	19	19	2/18/05-3/24/05

an estimate of the data-covariance matrix. Finally, we test the sensitivity of our recovered elevation-change rates to seasonal cycles in the surface elevation due to accumulation and time-varying densification.

Throughout this paper we will measure data residuals using $\hat{\sigma}$, a robust estimator of the standard deviation. $\hat{\sigma}$ is equal to half the width of the range that contains the central 68% of a distribution of residuals.

5.3.1 ICESat data and processing

We combine data from the GLA01 Global Altimetry Data and GLA12 Ice Altimetry Data. The data versions used are the most current available in May 2005; dates and version numbers are listed in table 1. We correct the return energy on GLA01 from all data from Release 21 and earlier using the formula given by Fricker and others (2005). We correct our data for detector saturation by shortening the range for all returns with a gain setting equal to 13 by 0.022 m/fJ for every fJ of return energy over 13.1 (Sun and others (2003)).

To minimize errors due to forward scattering by clouds and highly saturated returns, we screen the data based on a set of parameters describing the return pulse, provided in GLA12. Returns unaffected by saturation or forward scattering resemble narrow Gaussian pulses, similar to the transmitted pulse. We expect saturation and forward scattering to change the shape of these pulses, increasing the apparent surface roughness (estimated from the width

of the return-pulse), the misfit between the return pulse a Gaussian, and expect clouds to decrease the apparent surface reflectivity. We also expect forward scattering to increase the apparent shot-to-shot surface roughness because of inhomogenaeties in cloud layers. After some experimentation, we find that if we reject all returns for which the apparent surface reflectivity is less than 40 % or the apparent surface roughness is more than 2 m or the RMS difference between the digitized waveform and the best-fitting single Gaussian is more than 0.06 mV, we can reduce the RMS shot-to-shot surface roughness for the flat parts of WAIS from 0.30 m to 0.025 m. These criteria reject about 45% of all shots. To remove the few remaining large outliers resulting from small-scale surface roughness, undetected forward scattering, and minor aberrations in the pulse-fitting routine, we use an iterative 3-σ edit in calculating our regressions.

We calculate cross-over differences by linear interpolation into the elevations on each track to find the elevations at the crossing point. We estimate that the errors introduced by this interpolation are less than 0.05 m, based on the RMS error in estimating the elevations of every second shot in our region from the remaining shots. This error is a small component of the other errors discussed in section 5.3.3.

5.3.2 Elevation change regions

To obtain centimeter-level regression errors, at least a few hundred crossover measurements are required. Instead of dividing the ice sheet into a regular grid for this averaging, we prefer to make divisions based on our knowledge of the local glaciology (Bentley (1987)). We divide the RE into 28 regions (Figure 1), defined by 5 ice stream trunks, 10 well-defined tributaries, and 4 inter-stream ridges. We make smaller subdivisions in a few important areas: e.g. we treat the upstream end of the trunk of KIS (Kamb Junction) separately from the stagnant downstream end of KIS, and divide RIR into a slow-flowing section (RIR$_W$, abutting Siple Dome), and an upstream section (RIR$_E$) including some faster tributary flow. In the far south, the crossover density is very high, allowing the subdivision of MIS and CIR. We have also calculated elevation change rates for small areas surveyed by airborne laser altimetry; results from these areas are described by Csatho and others (2005).

5.3.3 Regression process

We assume that the elevation difference at each crossover results from a linear rate of elevation change, $\dot{z}$, that is constant for each local region of the ice sheet. This can be written as a matrix equation:

$$\mathbf{d} = \dot{z}\mathbf{t} + \varepsilon \tag{5.1}$$

Here $\mathbf{d}$ is a vector of N elevation differences, $z_{ai} - z_{di}$, $\mathbf{t}$ is a vector of N time differences, and ε is a vector of errors.

The least-squares $\dot{z}$ estimate based on equation 5.1 is:

$$\dot{z} = (\mathbf{t}^T C^{-1} \mathbf{t})^{-1} \mathbf{t}^T C^{-1} \mathbf{d} \tag{5.2}$$

Here C is the $N \times N$ data covariance matrix for errors in elevation measurements. $(\mathbf{t}^T C^{-1} \mathbf{t})^{-1} \mathbf{t}^T$ is the generalized inverse of $\mathbf{t}$, abbreviated $\mathbf{t}^{-g}$. The formal error estimate for $\dot{z}$ is then (Menke (1989))

$$\sigma_{\dot{z}}^2 = \mathbf{t}^{-gT} C^{-1} \mathbf{t}^{-g}. \tag{5.3}$$

The data covariance matrix is constructed as:

$$C_{i,j} = \begin{cases} \sigma_{pass}^2 + \sigma_{shot}^2 & i = j \\ (1/2)\sigma_{pass}^2 & \text{i and j from same pass} \\ 0 & \text{otherwise} \end{cases} \tag{5.4}$$

Here σ_{pass} is the error in z that is consistent for each pass over a region, while σ_{shot} is the error in z that is uncorrelated from shot to shot. The covariance matrix is necessary for accurate estimates of the error in $\dot{z}$, because increasing correlation between errors decreases the effective number of measurements of elevation change for a given region, producing larger errors.

We estimate the on-diagonal covariance at 0.31 m from the $\hat{\sigma}$ values of crossovers with time differences less than 8 days. Because this period is short, these should contain pass and shot errors but should be essentially unaffected by any elevation change signal. We obtain the off-diagonal covariance, σ_{pass}, by constructing a set of crossovers with essentially no elevation-difference signal correlated between tracks. This amounts to a regression of

elevation difference against a model with one independent parameter for each pass across our region, which can be solved by standard methods (Menke (1989)). Under this regression, the $\hat{\sigma}$ misfit of eight-day crossovers is 0.26 m; the difference between this and the on-diagonal covariance must be made up by σ_{pass}, so σ_{pass} is $\sqrt{0.31^2 - 0.26^2}$ m, or about 0.16 m.

Previous measurements of ice elevation change have found seasonal cycles in the elevation of the ice sheet, which are thought to result from seasonal accumulation and from temperature-dependant densification processes Zwally and Jun (2002). Because we have between 3 and 4 periods of measurements per year, we can estimate the magnitude, A, and phase, Φ, of the dominant elevation-signal. We assume that the Φ is spatially uniform, and that A is proportional to the accumulation rate, $\dot{b}$, as estimated by Vaughan and others (1999). Using all of the cross-overs in our region not eliminated by data-filtering, we fit a model of the form

$$z_a - z_d = (\dot{z})(t_a - t_d) + A\dot{b}(sin(2\pi t_a + \Phi) - sin(2\pi t_d + \Phi)) \tag{5.5}$$

to the cross-over differences in a least-squares sense, for t is in years. The contribution of the seasonal cycle to the cross-over differences is given by equation 5.5 excluding the secular elevation-rate term. These values may be subtracted from the cross-over values to correct elevation differences for the seasonal cycle.

We also analyze whether constant ranging biases for each period of laser operations could significantly affect the elevation estimates, by estimating the bias for each period by constrained least squares regression. We constrain these biases to have an RMS magnitude of 0.1 m (comparable to the difference between the version 16 and version 18 data releases (Luthcke and others (2005)), and find that the best fitting bias model does not significantly alter the recovered rates of elevation change.

5.4 Results

The data filtering and the 3-σ edit leave 19,858 crossovers distributed irregularly over our 28 regions. $\hat{\sigma}$ residuals for individual regions are between 0.25 and 0.55 m, and the cumulated residuals for all regions have a $\hat{\sigma}$ of 0.40 m.

Including the seasonal correction reduces the cumulated $\hat{\sigma}$ residual modestly, to 0.38 m. The best-fitting seasonal cycle has a minimum on November 15, a maximum on May 15, and an amplitude of 1.9 times the accumulation rate, although shifts in the phase of this cycle by up to 45 days in either direction have little effect on the residuals. The amplitude is mostly determined by measurements during period 2c, because all of the other periods fall near the zero-crossings of the cycle. The mean elevation rate from equation 5.5 is -0.09 m a^{-1}, which mostly reflects elevation changes on MIS and CIR, near the southern limit of coverage where cross-overs are disproportionately concentrated.

The calculated rates of elevation change, with and without the correction for the seasonal cycle, are given in Table 1 and the elevation rates without the seasonal correction are shown in Figure 5.5. We only consider significant those rates that are at least twice the formal regression error (typically 0.02 m a^{-1}), and larger than the 0.07 ma^{-1} random variation in surface height expected from randomly-varying accumulation and firn density Wingham (2000). Although correcting the data for the seasonal cycle results in a general decrease in the magnitude of elevation rates, only in the VdVIS tributary is the difference significant. In the discussion that follows we will refer to the uncorrected rates.

The largest rates are found in the tributary and junction regions of KIS, where thickening rates are between 0.25 and 0.28 m a^{-1}. In contrast, the tributary region of WIS and the upstream parts of MIS appear to be thinning: The tributaries of WIS and VdVIS are thinning at at 0.15 m a^{-1} and 0.17 m a^{-1}, respectively, the three divisions of CIR are thinning between 0.13 and 0.18 m a^{-1}, and the eastern part of MIS is thinning by 0.05 m a^{-1}. The downstream portions of MIS are approximately in balance, and the trunk and western portion of WIS appear to be thickening. In the northern part of the embayment, there is strong thinning in the trunk of BIS (0.18 ± 0.03 m a^{-1}), with smaller but still significant rates (0.07 - 0.15 m a^{-1}) on MIS, SIR, HIR, and Siple Dome.

5.5   Discussion

Analysis of ICESat crossover data have provided a new insight into the changes occurring in the RE. The demonstration of known glaciological characteristics of the RE, namely the

weak thinning at Siple Dome (Pettit (2004)) and the growth of the upper KIS system (Price and others (2001)), lends credibility to our results. Likewise, comparisons between airborne laser altimetry measurements from 1998 and from 2000, and between these measurements and ICESat, show elevation changes in KIS, VdVIS, and WIS very similar to those we estimate (Csatho and others (2005)). However, contrary to our expectation that elevation change should be confined to the ice streams, there appears to be more prevalent surface subsidence: for example, EIR and CIR both show thinning that is stronger than that seen in the adjacent ice streams.

The recovered seasonal cycle is roughly in phase with moisture transport into the RE estimated by Cullather and others (1998). This is surprising if the seasonal elevation cycle is due to the accumulation of snow for a constant densification rate, which would imply that the elevation should lag the accumulation, or if the densification is strongest in the summer, which would produce a decrease in elevation over the summer (Zwally and Jun (2002)). The recovered seasonal cycle may result from temporally-varying snow density, or may represent an error due to a measurement bias in the laser 2c period. The analysis of further epochs of ICESat data should clarify this.

We do not consider that the prevalent surface lowering is a conclusive indicator of long-term ice-dynamic conditions. It may instead be a result of a deficit in regional accumulation during the study period. Excluding the rapidly-thickening tributaries of KIS and rapidly-thinning CIR, the area-weighted mean elevation change for all regions is -0.08 ± 0.03 m a^{-1}, which is close to the 0.07 m a^{-1} elevation rate variability due to accumulation variations (Wingham (2000)).

Small random accumulation variations cannot explain the rapid thinning of CIR, EIR and HIR. We conclude that this thinning must be a response to recent elevation changes in the ice streams neighboring the ridges. Modeling by Nereson and others (1998) shows that fast changes in the ice streams are quickly propagated into the ridges, affecting the ridge divide after a delay of about 200 a. The time required for the change in the ridge to reach half of its equilibrium value is longer, about 500 a, so elevation change in the ridges reflects the mean behavior of the ice streams over approximately this period, with increasing sensitivity to recent changes. This thinning in the ridges may reflect retreat of the grounding

line: The grounding line appears to have reached its present position at the mouth of MIS relatively recently (Conway and others (1999)), and at WIS it has retreated at an average rate of 450 m a^{-1} in the late 20th century (Bindschadler and Vornberger (1998)). The fact that EIR and CIR are thinning faster than MIS and WIS suggests that rate of thinning in the ice streams was more rapid in the recent past than at present, although the time history of thinning is not possible to resolve from these measurements.

Acknowledgments for chapter 5

Table 5.2: Rates of elevation change and abbreviations for regions of the ice sheet. Column 3 gives the uncorrected elevation-change rate, shown in bold if significantly different from zero. Column 4 gives the elevation-change rate corrected for the season-cycle estimate. Column 5 gives the elevation rates corrected for laser ops period ranging biases. Regions may be designated IS: ice stream and IR: ice ridge.

| Region	abbreviation	elevation rate	season	ranging
Mercer IS W	MIS_W	-0.02 ± 0.02	-0.01	0.01
Mercer IS M	MIS_M	-0.04 ± 0.02	-0.06	-0.02
Mercer IS E	MIS_E	-0.05 ± 0.02	-0.08	-0.06
Conway IR SW	CIR_{SW}	$\mathbf{-0.18 \pm 0.02}$	-0.17	-0.15
Conway IR SE	CIR_{SE}	$\mathbf{-0.13 \pm 0.02}$	-0.14	-0.13
Conway IR N	CIR_N	$\mathbf{-0.18 \pm 0.02}$	-0.18	-0.17
Whillans IS trunk	WIS_{trunk}	0.06 ± 0.02	0.05	0.08
Whillans IS W	WIS_W	0.05 ± 0.02	0.04	0.08
Van der Veen IS	VdV	$\mathbf{-0.16 \pm 0.02}$	$\mathbf{-0.21}$	-0.15
Whillans IS N	WIS_N	$\mathbf{-0.15 \pm 0.02}$	-0.17	-0.15
Engelhardt IR S	EIR_S	$\mathbf{-0.12 \pm 0.02}$	-0.13	-0.11
Engelhardt IR N	EIR_N	$\mathbf{-0.10 \pm 0.02}$	-0.11	-0-08
Engelhardt IR E	EIR_E	0.04 ± 0.03	0.03	0.08
Kamb IS trunk	KIS_{trunk}	-0.06 ± 0.02	-0.08	-0.03
Kamb IS junction	KIS_{junc}	$\mathbf{0.27 \pm 0.03}$	0.28	0.28
Kamb IS S	KIS_S	$\mathbf{0.26 \pm 0.03}$	0.20	0.29
Kamb IS N	KIS_N	$\mathbf{0.29 \pm 0.03}$	0.23	0.32
Siple Dome	$Siple_{Dome}$	$\mathbf{-0.09 \pm 0.02}$	-0.13	-0.07
Raymond IR W	RIR_W	0.01 ± 0.03	-0.01	-0.01
Raymond IR E	RIR_E	$\mathbf{0.17 \pm 0.03}$	0.14	0.21
Bindschadler IS tr.	BIS_{trunk}	$\mathbf{-0.18 \pm 0.03}$	-0.22	-0.15
Bindschadler IS S	BIS_S	-0.07 ± 0.08	-0.10	-0.06
Bindschadler IS N	BIS_N	$\mathbf{-0.09 \pm 0.03}$	-0.11	-0.04
Shabtaie IR	SIR	$\mathbf{-0.14 \pm 0.04}$	-0.21	-0.12
Macayeal IS trunk	MIS_{trunk}	$\mathbf{-0.12 \pm 0.03}$	-0.14	-0.09
Macayeal IS S	MIS_S	-0.05 ± 0.03	-0.09	-0.05
Macayeal IS	MIS_N	-0.02 ± 0.05	0.05	0.03
Harrison IR	HIR	-0.02 ± 0.04	-0.08	-0.08
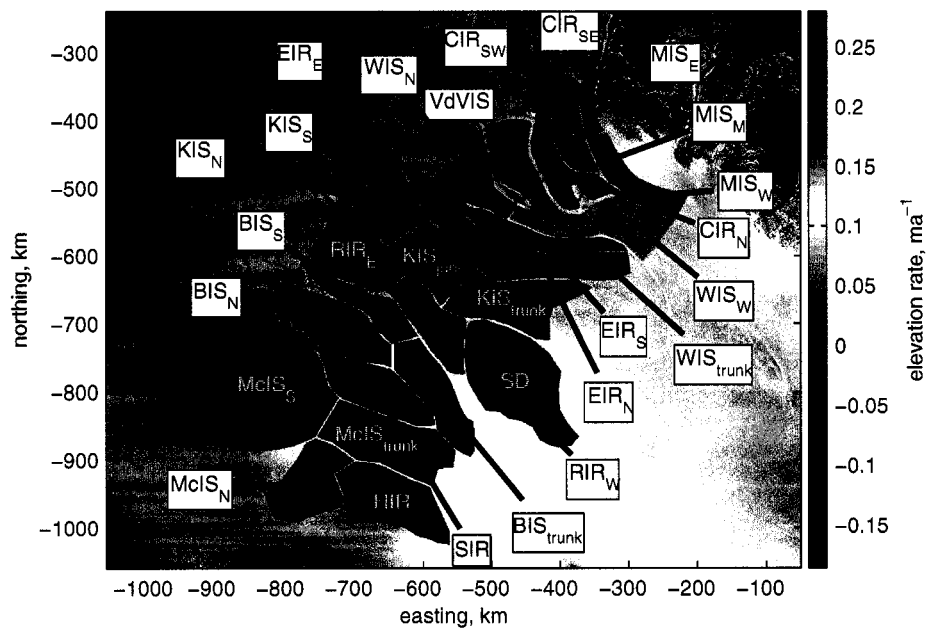
Figure 5.1: Derived rates of elevation change for the 28 regions of the Ross Embayment used in this study, listed in Table 5.2. Background image is the RAMP mosaic (Jezek and Team (2002)).

Chapter 6

SYNTHESIS

6.1 Summary and discussion

A significant part of this dissertation was a description of ice-surface topography. The description may be divided roughly into a characterization of the generic properties of the ice sheet surface, and a description of how the surface roughness varies across the ice sheet. These aspects are united in a process-based model of small-scale ice-surface topography that mimics the observed properties of the ice sheet.

The shapes of Fourier spectra of ice-sheet surfaces may be described as follows:

- At wavelengths less than the ice thickness, the surface expression of basal topography is very weak. Those surface features present may be generated by aeolian and depositional processes.

- At wavelengths between one and about 6 ice thicknesses, the spectral amplitude increases strongly with wavelength. Effective spectral exponents are on the order of 15-25 dBa/decade.

- At wavelengths greater than about 6 ice thicknesses, the spectral amplitude increases slowly with wavelength, with effective spectral slopes of 5-10 dBa/decade.

Further, the map-view variations in surface slope suggest that

- For ice that is not streaming rapidly, the 2-D spectral amplitude is proportional to the cosine of the angle between the normal to the ridge-crests of two dimensional Fourier components and the ice-flow direction.

The ice thickness is the dominant control on the shape of measured ice-sheet spectra, as it determines the transition between short- and long-wavelength behavior.

This description of ice-sheet topography may be sufficient for many purposes: For instance, a model of ice-atmosphere interactions to predict accumulation variations could use a two-part power-law model, to estimate the surface spectrum, with one spectral exponent to describe the topography for $\lambda < 6h$ and another to describe the topography for $\lambda > 6h$. This would reduce the number of free parameters needed to describe the ice sheet surface to two: The ice thickness and the surface roughness. A two-dimensional model of surface topography might include a parametrization of the azimuthal variation in the surface topography, but as I showed in chapter 2, profiles extracted from a surface with $A(\theta) \propto cos(\theta)$ have a consistent spectral shape for all azimuths, so in a 1-D model, the azimuthal variations could be included in the surface roughness.

These properties of ice-surface topography are drawn together by a model in which ice-flow over bed topography leads to surface topography. In the simpler form of the model, the ice is treated as a Newtonian fluid of constant (unstratified) viscosity, while in a more complex form the model approximates viscosity variations due to temperature and stress variations by an exponential model of viscosity stratification. These models predict both the observed spectral shape and the spatial roughness variations: Table 6.1 lists eight observations about the properties of ice sheet surfaces, and shows whether they have been demonstrated qualitatively or numerically to match the stratified or the unstratified transfer theories.

The broad success of this model in predicting the major features of ice sheet topography leads to the major conclusion of chapters 2, 3, and 4: That ice dynamics largely determine the properties of ice sheet topography at scales of several kilometers. This is not a surprising conclusion, and in some previous studies it is even a premise. However, my work demonstrates the level of detail that must be incorporated into an ice-dynamic model to capture the variations in surface topography: constant-viscosity transfer theory (Gudmundsson (2003)) is adequate to capture the most significant features of the ice-sheet topography, even though it does not fully account for the effects of variations in ice viscosity with depth. Incorporating viscosity variations can improve the similarities between

Table 6.1: Observed properties of ice sheet surfaces, and the degree to which their relationship to transfer theory has been observed or quantified. For each observed property of the ice sheet surface, I indicate whether the phenomenon has been (Q)ualitatively observed to have properties similar to those predicted by transfer theory or shown (N)umerically to have the properties predicted by transfer theory. The chapters in which each aspect of the theory is discussed are listed in column 3.

Observed	Unstratified	Stratified	Chapter
Spectral curves have a consistent shape	Q	N	2, 3
Spectral curves change slope at about $\lambda = 6h$		Q	3
Spectra depend on ice thickness	N	N	2, 3
Surface roughness depends on surface slope	Q	Q	2, 3, 4
Surface roughness depends on basal sliding	Q		3, 4
Spectral shapes are inconsistent with highly stratified viscosity profiles		N	3
Surface texture is anisotropic around the ice-flow direction	Q		4

model spectra and measured spectra, but only if the effects of longitudinal stretching on the ice viscosity are taken into account in selecting the stratification parameter in the transfer model.

The last chapter of the dissertation looked at temporal changes in the ice-surface topography in the Ross Embayment. These measurements show that apparent surface changes are prevalent, and spatially variable on scales at least as small as 50-100 km. Some of the apparent elevation changes, in particular those in the tributaries of Kamb Ice Stream, are consistent with well-known properties of the ice dynamics. Others show changes where no previous studies have estimated elevation change, such as in the eastern part of Raymond Ice Ridge and in the eastern part of Conway Ice Ridge. A few changes, such as the apparent thinning in the trunk of Kamb ice stream, are in direct contradiction to the expectations of previous authors. Because our estimates of elevation change are based on a short time-series of measurements, with a very new measurement system, these estimates should be repeated as more ICESat data become available and the potential biases and errors in the ICESat system are better known.

6.2   *Directions for further research*

My description of ice-sheet surfaces is neither complete nor comprehensive. It is incomplete in that, among other things, I have ignored any property of the surface related to the phase of surface spectra. I have assumed in modeling the surface that the bed spectrum is purely incoherent; however, Jóhannesson (1992) showed that coherent features at the bed, such as sharp, isolated mountains or rifts, can produce qualitatively different features at the surface than small amplitude random bed features, including local spectral peaks at a few times the ice thickness. Analysis of phase spectra is more complicated than the analysis of amplitude spectra, and might most usefully be performed over small areas, rather than in the context of a continental survey such as mine.

My description is not comprehensive, in that I have not used all of the data available, even in the ICESat data-set I explored in chapters 2 and 3. In the process of mapping spectral components over Antarctica, I discarded large numbers of spectral estimates in

the interest of having only one estimate per pixel. Near the southern limit of coverage, at 86° S, I used only a small fraction of the available data. In this area, direct estimates of the two-dimensional Fourier transform of the surface should be possible from ICESat data alone, which would allow a more precise description of the anisotropy of the ice sheet surface there.

The analysis in this dissertation includes very few data describing the ice-sheet bed. Except for chapter 5 I maintain a very broad view of the ice sheets, describing the statistics of ice surfaces in general rather than investigating any specific part of the ice sheet in detail. Although in most parts of the Greenland and Antarctic ice sheets few data exist that could describe bed topography on a kilometer scale, there are a few areas in each continent where radio echo sounding has mapped the bed extensively. Notably, bed topography is known on the Ross Embayment ice streams on flight-lines between 5 and 10 km apart, and a similar survey is underway around the Pine Island region of West Antarctica. Both of these areas have the potential to discharge large volumes of ice into the oceans, a process which requires the expansion of fast-flowing ice streams into the relatively stagnant surrounding ice. My analysis suggests that a change in the ice stream boundaries would be accompanied by an increase in surface roughness that would be visible from space; current measurements of surface roughness will allow monitoring of these areas for changes in flow characteristics in the future, and knowledge of the bed roughness, combined with the analysis in chapter 2, should help calibrate estimates of the sliding rate should the streaming areas expand.

My techniques also suggest ways of handling uncertainties in studies using bed-topography data. For example, the surface topography on a line that has been surveyed with radar depends both on the bed topography directly below the survey line, which is imaged by the radar, and on the topography of the surrounding bed. The potential contributions from this unknown topography may be estimated under the assumption that the rest of the bed has red-noise properties, with an amplitude comparable to that measured beneath the survey line.

The elevation-change analysis in chapter 5 may be repeated as long as ICESat continues to give high-quality ice-elevation data. Each additional cycle of data will improve estimates of the rate of elevation change, and will help to correct for instrumental ranging biases.

A small area on Conway Ridge, where the elevation-rate is known independently from measurements of ice divergence and snowfall, may serve as a calibration site to independently estimate the biases during 2003-2004.

BIBLIOGRAPHY

Alley, R. B. and R. Bindschadler. 2001. The West Antarctic Ice Sheet and sea level. *In* R. B. Alley and R. Bindschadler, *eds, Ant. Res. Ser. 77*. American Geophysical Union, Washington D.C, 1–12.

Austin, R. T., A. W. England and G. H. Wakefield. 1994. Special problems in the estimation of power-law spectra as applied to topographical modeling. *IEEE Trans. Geosci. Remote Sensing*, **32**, 928–939.

Bamber, J., R. Hardy and I. Joughin. 2000. An analysis of balance velocities over the Greenland Ice Sheet and comparison with synthetic aperture radar interferometry. *J. Glaciol.*, **46**(152), 67–74.

Bamber, J. L. and R. A. Bindschadler. 1997. An improved elevation dataset for climate and ice-sheet modelling: validation with satellite imagery. *Ann. of Glaciol.*, **25**, 438–444.

Bamber, J. L. and J. L. G. Dans. 2005. The accuracy of digital elevation models of the Antarctic continent. *Ann. of Glaciol.*, **In Press**.

Bamber, J. L., D. J. Baldwin and S. P. Gogineni. 2003. A new bedrock and surface elevation dataset for modelling the Greenland Ice Sheet. *Ann. of Glaciol.*, **37**, 351–356.

Bell, E. E., D. D. Blankenship, C. A. Finn, D. L. Morse, T. A. Scambos, J. M. Brozena and S. M. Hodge. 1998. Influence of subglacial geology on the onset of a West Antarctic ice stream from aerogeophysical observations. *Nature*, **394**, 58–62.

Bentley, C. R. 1987. Antarctic Ice Streams: A Review. *J. Geophys. Res.*, **92**(B9), 8843–8868.

Bindschadler, R. and P. Vornberger. 1998. Changes in the West Antarctic Ice Sheet since 1963 from declassified satellite photography. *Science*, **279**(5351), 689–692.

Bindschadler, R., K. Wobeter, H. Choi and P. Vornberger. 2004. Self help: Ice streams retain more water by moving faster. Abstracts from the 11th Annual WAIS Workshop. http://igloo.gsfc.nasa.gov/wais/pastmeetings/Sched04.htm.

Budd, W. F. 1968. The longitudinal velocity profile of large ice masses. *IAHS*, **79**, 58–75.

Budd, W. F. 1969. The dynamics of ice masses. Australian National Antarctic Research Expedition, Scientific Report 108, Melbourne, Australia.

Budd, W. F. 1970. Ice flow over bedrock perturbations. *J. Glaciol.*, **9**(55), 29–48.

Budd, W. F. and D. B. Carter. 1971. An analysis of the relation between the surface and bedrock profiles of ice caps. *J. Glaciol.*, **10**(59), 197–209.

Conway, H., B. L. Hall, G. H. Denton, A. Gades and E. Waddington. 1999. Past and future grounding-line retreat of the West Antarctic Ice Sheet. *Science*, **286**, 280 – 283.

Csatho, B., Y. Ahn, T. Yoon, C. van der Veen, V. B. Spikes, G. Hamilton, D. Morse and S. Vogel. 2005. Icesat measurements confirm complex patterns of thickness changes on Siple Coast ice streams, Antarctica. *Geophys. Res. Lett.*, **In Press**.

Cullather, R. J., D. H. Browich and M. L. Van Woert. 1998. Spatial and temporal variability of Anrarctic precipitation from atmospheric methors. *J. Climate*, **11**, 334–368.

Ekholm, S., K. Keller, J. L. Bamber and S. P. Gogineni. 1998. Unusual surface morphology from digital elevation models of the greenland ice sheet. *Geophys. Res. Lett.*, **25**(19), 3623–3626.

Fahnestock, M. A., T. A. Scambos, C. A. Schuman, R. J. Arthern, D. P. Winebrenner and R. Kwok. 2000. Snow megadune fields on the East Antarctic Plateau: extreme atmosphere-ice interaction. *Geophys. Res. Lett.*, **27**(22), 3719 (1999GL011248).

Fricker, H. A., A. Borsa, C. Carabajal, K. Quinn, B. Bills and B. Minster. 2005. Assessment of ICESat performance at the Salar de Uyuni, Bolivia. *Geophys. Res. Lett.*, **In Press**.

Gagnon, J. S., S. Lovejoy and D. Schertzer. 2003. Multifractal surface and terrestrial topography. *Europhysics letters*, **62**(6), 801–807.

Gray, L., I. Joughin, S. Tulaczyk, V. B. Spikes, R. Bindschadler and K. Jezek. 2005. Evidence for subglacial water transport in the West Antarctic Ice Sheet through three-dimensional satellite radar interferometry. *Geophys. Res. Lett.*, **32**(3), L03501.

Gudmundsson, G. H. 2003. Transmission of basal variability to a glacier surface. *J. Geophys. Res.*, **108**(B5), 2253. doi:10.1029/2002JB002107.

Gudmundsson, G. H., C. F. Raymond and R. Bindschadler. 1998. The origin and longevity of flow-stripes on Antarctic ice streams. *Ann. of Glaciol.*, **27**, 145–152.

Hodge, S. M. and S. K. Doppelhammer. 1996. Satellite imagery of the onset of streaming flow of ice streams C and D, West Antarctica. *J. Geophys. Res.*

Hutter, K., F. Legerer and U. Spring. 1981. First-order stresses and deformations in glaciers and ice sheets. *J. Glaciol.*, **27**(96), 227–270.

Jezek, K. and R. P. Team. 2002. RAMP AMM-1 SAR image mosaic of Antarctica. Digital Media.

Jóhannesson, T. 1992. *Landscape of temperate ice caps.* (Ph.D. thesis, Univ. of Washington.)

Joughin, I. and S. Tulaczyk. 2002. Positive mass balance of the Ross Ice Streams, West Antarctica. *Science*, **295**, 476–480.

Joughin, I., M. Fahnestock, D. MacAyeal, J. Bamber and P. Gogineni. 2001. Observation and analysis of ice flow in the largest Greenland ice stream. *JGR*, **106**(D24), p. 34,021 (2001JD900087).

Joughin, I., S. Tulaczyk, R. Bindschadler and S. F. Price. 2002. Changes in West Antarctic ice stream velocities: Observation and analysis. *J. Geophys. Res.*

Joughin, I., S. Tulaczyk, D. R. Macayeal and H. Engelhardt. 2004. Melting and freezing beneath the Ross ice streams, Antarctica. *J. Glaciol.*, **50**(168), 96–108.

Kamb, B. and K. A. Echelmeyer. 1986. Stress-gradient coupling in glacier flow: I. Longitudinal averaging of the influence of ice thickness and surface slope. *J. Glaciol.*, **32**(111), 267–284.

Liu, C., C. R. Bentley and N. E. Lord. 1999. Velocity difference between the surface and base of Ice Stream B2, West Antarctica, from radar fading-pattern experiment. *Ann. of Glaciol.*, **29**, 243–249.

Luthcke, S. B., D. D. Rowlands, T. A. Williams and M. Sirota. 2005. Geolocation errors and the impact on ice sheet elevation change detection. *Geophys. Res. Lett.*, **In Press**.

Lythe, M., D. G. Vaughan and the Bedmap Consortium. 2001. Bedmap: a new ice thickness and subglacial topographic model of Antarctica. *JGR*, **106(B6)**, 11335–11351.

Malamud, B. D. and D. L. Turcotte. 2001. Wavelet analyses of Mars polar toporaphy. *J. Geophys. Res.*, **106**(E8), 17497–17504.

McIntyre, N. 1986. Antarctic ice sheet topography and surface bedrock relationships. *Ann. of Glaciol.*, **8**, 124–128.

Menke, W. 1989. *Geophysical Data Analysis, Discrete Inverse Theory*, volume 45 of *International Geophyics Series*. Academic Press.

Nereson, N. A. and C. F. Raymond. 2001. The elevation history of the ice streams and spatial accumulation patterns along the Siple Coast of West Antarctica inferred from ground-based radar data from three inter-ice stream ridges. *J. Glaciol.*, **47**(157), 303–313.

Nereson, N. A., R. C. A. Hindmarsh and C. F. Raymond. 1998. Sensitivity of the divide position at Siple Dome, West Antarctica, to boundary forcing. *Ann. of Glaciol.*, **27**, 207–214.

Nye, J. F. 1952. The mechanics of glacier flow. *J. Glaciol.*, **2**(12), 82–93.

Nye, J. F. 1959a. A method of determining the strain-rate tensor at the surface of a glacier. *J. Glaciol.*, **3**(25), 409–418.

Nye, J. F. 1959b. The motion of glaciers and ice sheets. *J. Glaciol.*, **3**(26), 493–407.

Parizek, B. R., R. B. Alley, S. Anandakrishnan and H. Conway. 2002. Sub-catchment melt and long-term stability of ice stream D, West Antarctica. *Geophys. Res. Lett.*, **29**(8), Art. No. 1214.

Paterson, W. S. B. 1994. *The Physics of Glaciers*. Pergamon Press, Oxford, 3rd edition.

Pettit, E. C. 2004. *Unique Dynamic Behaviors of Ice Divides*. Ph.d thesis, University of Washington, Seattle, WA.)

Price, S. F., R. A. Bindschadler, C. L. Hulbe and I. Joughin. 2001. Post-stagnation behavior in the upstream regions of ice stream c, West Antarctica. *J. Glaciol.*, **47**.

Raymond, M. and G. H. Gudmundsson. 2005. On the relationship between surface and basal properties on glaciers, ice sheets, and ice streams. *In Preparation*.

Reeh, N. 1982. A plasticity theory approach to the steady-state shape of a three-dimensional ice sheet. *J. Glaciol.*, **28**(100), 431–455.

Reeh, N. 1987. Steady-state three-dimensional ice flow over an undulating base: first-order theory with linear ice rheology. *J. Glaciol.*, **33**(114), 177–185.

Remy, F. and J. F. Minster. 1997. Antarctica ice sheet curvature and its relation with ice flow and boundary conditions. *Geophys. Res. Lett.*, **24**(9), 1039–1042.

Remy, F., P. Shaeffer and B. Legresy. 1999. Ice flow physical processes derived from the ERS-1 high-resolution map of the Antarctica and Greenland ice sheets. *Geophys. J. Int.*, **139**, 645–656.

Remy, F., B. Legresy and L. Testut. 2001. Ice sheet and satellite altimetry. *Surveys in Geophysics*, **22**(1), 1–29.

Ridley, J., W. Cudlip and S. W. Laxon. 1993. Identification of subglacial lakes using ERS-1 radar altimeter. *J. Glaciol.*, **39**(133), 625–634.

Scambos, T. and T. Haran. 2001. An image-enhanced DEM of the Greenland Ice Sheet. *Ann. of Glaciol.*, **34**, 291–298.

Scambos, T. A., N. A. Nereson and M. A. Fahnestock. 1998. Detailed topography of Roosevelt Island and Siple Dome, West Antarctica. *Ann. of Glaciol.*, **27**, 61–67.

Schoof, C. 2002. Basal perturbations under ice streams: Form drag and surface expression. *J. Glaciol.*, **48**(162), 407–416.

Schutz, R., H. J. Zwally, C. Shuman, D. Hancock and J. DiMarzio. 2005. Icesat mission overview, 2005. *Geophys. Res. Lett.*, **In Press**.

Siegert, M. J., J. Taylor, A. J. Payne and B. Hubbard. 2004. Macro-scale bed roughness of the siple coast ice streams in West Antarctica. *Earth Surface Processes and Landforms*, **29**, 1591–1596.

Siegert, M. J., J. Taylor and A. J. Payne. 2005. Spectral roughness of subglacial topography and implications for former ice sheet dynamics in East Antarctica. *Global and Planetary Change*, **45**, 249–263.

Smith, B. E. 2005. *Analysis of Small scale ice sheet topography of Antarctica and Greenland.* (Ph.D. thesis, University of Washington.)

Smith, B. E., N. E. Lord and C. R. Bentley. 2002. Crevasse ages on the northern margin of Ice Stream C, West Antarctica. *AG*, **34**, 209–216.

Smith, W. H. F. and P. Wessel. 1990. Gridding with continuous curvature splines in tension. *Geophysics*, **55**, 293–305.

Spikes, V., G. Hamilton, S. Arcone, S. Kaspari and P. Mayewski. 2004. Variability in accumulation rates from GPR profiling on the West Antarctic Plateau. *Ann. of Glaciol.*, **39**.

Spikes, V. B., B. M. Csatho, G. S. Hamilton and I. M. Whillans. 2003. Thickness changes on Whillans Ice Stream and Ice Stream C, West Antarctica, derived from laser altimeter measurements. *J. Glaciol.*, **49**(165), 223–230.

Sun, X., J. B. Abshire and D. Yi. 2003. Characteristics and performance of the altimeter receiver. *In EOS trans., AGU Fall mtg supplement, Abstract C32A-0432*, volume 84, F383, San Francisco, CA.

Thorsteinsson, T., C. F. Raymond, G. H. Gudmundsson, R. B. Bindschadler, P. Vornberger and I. Joughin. 2003. Bed topography and lubrication inferred from surface measurements on fast flowing ice streams. *J. Glaciol.*, **49**(167), 481–490.

Turcotte, D. L. 1992. *Fractals and Chaos in Geology and Geophysics*. Cambridge University Press.

Vaughan, D. J., J. L. Bamber and M. Giovinetto. 1999. Reassessment of net surface mass balance in Antarctica. *J. Climate*, **12**(4), 933–946.

Whillans, I. M. 1983. Ice movement. *In* G. d. Robin, *ed, The climatic record in polar ice sheets*, 70–77. Cambridge University Press, Cambridge etc.

Wild, M., P. Calanca, S. C. Scherrer and A. Ohmura. 2003. Effects of polar ice sheets on global sea level in high-resolution greenhouse scenarios. *J. Geophys. Res.*, **108**(D5).

Wingham, D. J. 2000. Short fluctuations in the density and thickness of a dry firn column. *J. Glaciol.*, **146**, 399–411.

Zwally, H. J. and L. Jun. 2002. Seasonal and interannual variations of firn densification and ice-sheet surface elevation at the greenland summit. *J. Glaciol.*, **48**(161), 199–207.

Zwally, H. J., B. Schutz, W. Abdalati, J. Abshire, C. R. B. C, A. Brenner and ten more. 2002. Icesat's laser measurements of polar ice, atmosphere, ocean, and land. *J. Geodynamics*, **34**(3-4), 405–445.

Appendix A

THE FOURIER SLICE THEOREM APPLIED TO TOPOGRAPHIC SPECTRA

The Fourier Slice Theorem appears frequently in discussions of tomography and seismic image processing (e.g. Menke (1989)). Although I have found it useful in manipulating 2-D red-noise Fourier spectra, I have not found a published example showing its use in this way. Accordingly, I sketch a proof of the Fourier Slice Theorem as applied to the extraction of 1-D profile spectra from 2-D Fourier spectra below.

Suppose a two-dimensional surface $s(\mathbf{u})$ has a Fourier spectrum $S(\mathbf{k})$. The two are related by:

$$s(\mathbf{u}) = \int S(\mathbf{k})e^{2\pi i(\mathbf{k}\cdot\mathbf{u})}d\mathbf{u} \tag{A.1}$$

A profile parallel to $\hat{\mathbf{x}}$ samples the surface on the line $\mathbf{u} = l\hat{\mathbf{x}}$. The topography on this surface is $\phi(l) = s(l\hat{\mathbf{x}})$, and its Fourier transform, written terms of equation A.1 is:

$$\phi(\omega, \hat{\mathbf{x}}) = \int e^{-2\pi i l\omega}\left(\int S(\mathbf{k})e^{2\pi i\mathbf{k}\cdot(l\hat{\mathbf{x}})}d\mathbf{k}\right)dl \tag{A.2}$$

or,

$$\phi(\omega, \hat{\mathbf{x}}) = \int\int S(\mathbf{k})e^{2\pi i\mathbf{k}\cdot(l\hat{\mathbf{x}})-2\pi i l\omega}d\mathbf{k}dl \tag{A.3}$$

The integral over l reduces to a δ-function, so

$$\phi(\omega, \hat{\mathbf{x}}) = \int S(\mathbf{k})\delta(\omega - \mathbf{k}\cdot\hat{\mathbf{x}})d\mathbf{k}. \tag{A.4}$$

This shows that the spectrum at frequency ω of a profile extracted from a surface parallel to $\hat{\mathbf{x}}$ is equal to the sum of the 2D Fourier transform on a line in the k-plane perpendicular to $\hat{\mathbf{x}}$ running through the point $\mathbf{k}\omega$. If components of the 2D Fourier spectrum are incoherent (meaning that they are independent realizations of a Gaussian random process, as we expect for surfaces predicted from red-noise beds), then the components add incoherently, and

equation A.4 becomes:

$$\phi(\omega, \hat{\mathbf{x}})^2 = \int S(\mathbf{k})^2 \delta(\omega - \mathbf{k} \cdot \hat{\mathbf{x}}) d\mathbf{k}. \tag{A.5}$$

where $\phi(\omega, \hat{\mathbf{x}})$ is now the expected value of the surface amplitude. This equation may be rewritten in terms of a line-integral on the $\mathbf{k}$-plane running perpendicular to $\hat{\mathbf{x}}$ through the point $\omega\hat{\mathbf{x}}$:

$$\phi(\omega, \hat{\mathbf{x}})^2 = \int_{-\infty}^{\infty} S(\omega\hat{\mathbf{x}} + t\hat{\mathbf{t}})^2 dt, \tag{A.6}$$

where $\hat{t}$ is a unit vector in the $\mathbf{k}$ plane that is perpendicular to $\hat{\mathbf{x}}$.

Appendix B

RECOVERING BIASES IN LASER EPOCHS BY CONSTRAINED LINEAR REGRESSION

At this time, not all ICESat data are processed to the highest possible quality, and data from some operations periods have residual pointing and range biases remaining, especially Laser 2b, 2c and 3a (Luthcke and others (2005)). We consider a simple model for how ICESat instrument biases may affect our results. We suppose that for each operations period , ICESat had a different ranging bias and a different ascending-descending bias, and that any improvement to our knowledge of these biases will reduce crossover residuals.

We look for models for which the RMS ranging bias is on the order of 0.1 m, comparable to the improvements made between release 18 and release 21 of ICESat data. We estimate the ranging biases by augmenting the **t** matrix in equation 5.1 with two columns and two rows per laser operations period. The added columns give $\partial d_i / \partial L_j$ and $\partial d_i / \partial A_j$, the dependence of the elevation differences, d_i, on the ranging biases, L_j, and the ascending-descending biases, A_j. The added rows give constraint equations, forcing the estimated biases to be close to zero. By adjusting the weights on the constraint equations we can tune the recovered biases to have an approximate RMS of 0.1 m.

The optimum solution with a 0.10 m RMS bias has a $\hat{\sigma}$ of 0.31 m. It suggests that Laser 2c has a range bias of +0.12 m (the estimate of the surface elevation is 0.12 m too high), while Laser 3a has a range bias of -0.19 m. These results are roughly consistent with those of Fricker and others (2005), although we find a larger bias for laser 3a than they do. Lasers 1, 2a, 2b, and 3b have biases less than 0.07 m, and there is no significant linear trend in the laser biases as a function of time. The difference between ascending and descending biases is less than 0.05 m for all operations periods. This model results in a small universal algebraic increase in the rate of elevation change, but no significant changes in $\dot{z}$ estimates from the uncorrected calculation. This implies that the pattern of elevation change seen

here should be robust to further improvements to our understanding of the ICESat ranging bias.

CURRICULUM VITAE

Benjamin E. Smith

University of Washington

Department of Earth and Space Sciences

Condon Hall 310 Box 351310

Seattle WA, 98122 ben @ ess.washington.edu

Education

- **University of Washington, Seattle**

  Ph.D, Earth and Space Sciences, 2005 (anticipated)

- **University of Wisconsin, Madison**

  M.S., Geophysics, 1999

- **University of Chicago**

  B.S., Physics, 1997

Award

- 2002 – 05 NASA Earth Systems Sciences Fellow

Publications and selected presentations

- Smith, B.E, N. E. Lord, and C. R. Bentley. Crevasse ages on the northern margin of Ice stream C, West Antarctica. 2002. *Annals of Glaciology* **34**: 209-216

- Winebrenner, D.P., B. E. Smith, G, A. Catania, H. B. Conway, and C. F. Raymond Radio-frequency attenuation beneath Siple Dome, West Antarctica, from wide-angle and profiling radar observations. 2003. *Annals of Glaciology* **37**: 226-232

- Smith, B. E. Kilometer-scale texture of the West Antarctic Ice Sheet. 2004. Poster. AGU 2004 fall meeting, San Francisco, CA.

- Smith, B. E. High-resolution Antarctic topography from the ICESat mission near 86S. Invited talk, AGU 2004 fall meeting, San Francisco, CA.

- Smith, B. E., C. R. Bentley, and C. F. Raymond. Recent elevation changes on the ice streams and ridges of the Ross Embayment from ICESaT crossovers. 2005. *Geophysical Research Letters, submitted*